Fabrication of Thin Films of Semiconductor Alloys Containing Cu- and Fe-Sulfides by the Electrochemical Deposition Method

by

Yang Kai

Thesis for Ph. D. degree of engineering

Department of Engineering Physics, Electronics and Mechanics,
Graduate School of Engineering,
Nagoya Institute of Technology,
Nagoya, Japan.

March 2014

Abstract

In this doctoral thesis, the electrochemical deposition (ECD) of p-type Cu_xZn_yS, $Cu_2ZnSnS_{4-x}O_x$ (CZTSO), FeS_xO_y thin films were studied. These films are environment-friendly and toxic free material, which are promising candidates as either transparent conduction film or solar cell.

This thesis has five chapters. In the first chapter, we introduce a brief background on thin film and the different thin films deposition technique, and explain the advantages of the ECD technique. The ECD techniques are classified according to the nature of applied bias, and the cyclic voltammogram is explained. Finally we introduce basic properties of Cu_2S, Cu_2ZnSnS_4, and FeS_2, which are basic constituents of the films deposited in this work.

In the second chapter, Cu_xZn_yS thin films were deposited on the indium-tin-oxide (ITO)-coated glass from solutions containing $Na_2S_2O_3$, $CuSO_4$ and $ZnSO_4$ by the ECD and photochemical deposition (PCD) methods. Films with different Zn/Cu ratios were deposited. The Cu_xZn_yS thin films had a wide band gap of 3.0-3.6 eV. The Cu_xZn_yS films showed p-type conduction and photosensitivity in the photoelectrochemical (PEC) measurement. Moreover, we fabricated ZnO/ Cu_xZn_yS/ITO heterojunction, and rectification properties were confirmed. We annealed Cu_xZn_yS in a nitrogen atmosphere for an hour at different temperatures up to 400°C. The optical transmission increased with increasing annealing temperature, whereas the bandgap did not vary significantly.

In the third chapter, CZTSO thin films were deposited on the ITO substrate by the DC and two-step pulsed ECD methods from aqueous solutions containing $CuSO_4$, $ZnSO_4$, $SnSO_4$, and $Na_2S_2O_3$. The films deposited by pulsed ECD contained smaller amount of oxygen than those deposited by DC ECD. The films had band gap energies in a range from 1.5 eV and 2.1 eV. By a PEC measurement, it was confirmed that CZTSO films showed p-type conduction and photosensitivity. CZTSO/ZnO heterojunctions exhibited rectification properties. CZTSO

thin films deposited by pulsed ECD were sulfurized at 300ºC. After the sulfurization, the oxygen amount decreased clearly. The optical transmission became higher, but the bandgap did not change clearly. Relatively strong X-ray diffraction (XRD) peaks of CZTS were observed, and weak photovoltaic effects were confirmed for heterojunction with ZnO.

In the fourth chapter, FeS_xO_y thin films were fabricated by the ECD method. The composition was Fe:S:O ≈ 1:1:1 when the $FeSO_4$ concentration was 40 mM, $Na_2S_2O_3$ concentration 100 mM, and the deposition temperature 15 ~ 40ºC. In the PCE measurement, the deposited FeS_xO_y film showed p-type conduction and photoconductivity. The band gap was estimated to be 1.2 eV. The Raman spectra showed that Fe atoms in FeS_xO_y are bonded to both O and S atoms so that new vibrational bands are formed. Moreover, a ZnO/ FeS_xO_y heterostructure was fabricated, and rectification properties were confirmed. After annealing at 100 ~ 400ºC in a nitrogen atmosphere for an hour, the Fe content did not vary significantly, while the O/S ratio increased with annealing temperature. The optical transmission and the bandgap increased with increasing annealing temperature. After the 400ºC annealing, the XRD peaks of Fe_3O_4 were observed and the conduction type was changed to n-type.

In the fifth chapter, we give conclusion of this work and suggestions for the future works.

Acknowledgements

First and foremost I thank my supervisor, Prof. Masaya Ichimura, who gave me the opportunity to join this lab. I thank him for giving me unswerving confidence that I knew what I was doing at every stage of this research, which made this research possible through his guidance, support and encouragement over the past 5 years. I am grateful to Dr. Masashi Kato for his comments, pieces of advice and discussion.

My cordial gratitude to Prof. Tetsuo Soga and Associate Prof. Madan Niraula for the time spent in reading and commenting my manuscript. Their ideas and suggestions really helped.

I am particularly indebted to my teacher Dr. Hidehiro Ikeda and Prof. Toru Oda, Nishinippon Institute of Technology. They introduced me to the solar cell research and encouraged me to overcome setbacks.

I would also like to thank all the past and present members of the Ichimura group for scientific discussions, technical support, and general collaboration in the lab. I especially thank Mr. Ashraf and Ms. Supria Chowdhury, Mr. Muhibbullah, Mr. Nakashima, Ms. Odon, Ms. Song, Ms. Bao, Mr. Junie, Mr. Zhang Hai, Mr. Mandula, Mr. Yamazaki, Mr. Maeda, and Mr. Tanaka. Many thanks also to Mr. Moriguchi for his technical assistance.

I am grateful to Japan Student Services Organization (JASSO), Meitetsu International Scholarship Foundation, Nagaya Institute of Technology I- scholarship, and Rotary Yoneyama Memorial Foundation for the scholarships, which helped me to accomplish this work. Specially, thanks to Mr. Shigeki Kokubo and Mr. Atsuo Itoh of Rotary Club of Toyota-Naka

for their support. The interactions with the rotary club members cultivate my spirit of societal participation.

Finally, the love and support of my parents, my wife Chang Yue, and my son Yangchang Yigu turned any fear of failure into desires to succeed . Thank you very much.

Contents

Chapter 2: Fabrication of transparent p-type Cu_xZn_yS thin films by the electrochemical and photochemical deposition method

Chapter 3: Fabrication of Cu-Zn-Sn-S-O thin films by the electrochemcal deposition method and application to heterojunction cells.

Chapter 4: Electrochemical deposition of Fe-S-O thin films

Chapter 5: Conclusions

Chapter 1
Introduction

1.1. Thin film

A thin film is a layer of material ranging from fractions of a nanometer (monolayer) to several micrometers in thickness. Electronic semiconductor devices and optical coatings are the main applications benefiting from thin-film construction.

Thin film research and experimental work for successful application of its properties in engineering and different branches of science and technology are greatly expanding in different parts of the world. During the last five decades, a great deal of research work has been carried out on thin films of metals, semiconductors and insulators. Sufficient time has also been utilized to search for other new coating materials relevant to electro-optical properties. These include the spectrally selective coating, transparent conducting coating, heating elements, antistatic coating on instrument panels, and electrical contact in liquid crystals, electro-chromic and electro-luminescent displays, smart window coating, photo-chromic, thermo-chromic coating and solar absorbing layer etc. according to design and structure of the devices. These coating may be either a single or multilayer on a suitable neutral substrate or may be a layer forming composite structure with the substrate. Among the above varieties of layers, oxide and sulfide thin films have been figured prominently for solar cell application.

1.1.1. Transparent conducting film

Transparent conducting films (TCFs) are optically transparent and electrically conductive in thin layers. TCFs for photovoltaic applications have been fabricated from both inorganic and organic materials. Inorganic films typically are made up of a layer of transparent conducting oxide (TCO), generally in the form of indium tin oxide (ITO), fluorine

doped tin oxide (FTO), and doped zinc oxide. Organic films are being developed using carbon nanotube networks and graphene, which can be fabricated to be highly transparent to infrared light, along with networks of polymers such as poly (3,4-ethylenedioxythiophene) and its derivatives.

Transparent materials possess bandgaps with energies corresponding to wavelengths which are shorter than the visible range of 380 nm to 750 nm. Photons with energies below the bandgap are not collected by these materials and thus visible light passes through. However, applications such as photovoltaics may require an even broader bandgap to avoid unwanted absorption of the solar spectra.

1.1.1.1. n-type transparent conducting films

TCO have been widely used in optoelectronics industries as well as in research fields. The first report of transparent conducting thin films of cadmium oxide (CdO) was published in 1907 by Badekar [1] who prepared the films by thermal oxidation of sputtered films of cadmium. Since then extensive works have been done in the field of TCO technology to prepare new types of TCOs with wide ranging applications [2]. These well-known and widely used TCOs include SnO_2:Sb/F, ZnO:In/Al/F/B/Ga, In_2O_3:Sn/F/Sb/Pb, Cd_2SnO_4 etc. as well as some new TCOs such as Zn_2SnO_4, $ZnSnO_3$, $GaInO_3$:Ge/Sn, $AgInO_2$:Sn, $MgIn_2O_4$, $CdSb_2O_6$:Y, $Zn_2In_2O_5$, $ZnGa_2O_4$, $In_4Sn_3O_{12}$, $CdIn_2O_4$:Sn etc.. As far as applications are concerned, TCOs are being used extensively in the window layers of solar cells, as front electrodes in flat panel displays (FPD), low-emissivity (‘‘low-e’’) windows, electromagnetic shielding of cathode-ray tubes in video display terminals, as electrochromic (EC) materials in rear-view mirrors of automobiles, EC-windows for privacy (so-called ‘‘smart windows’’), oven windows, touch-sensitive control panels, defrosting windows in refrigerators and airplanes, invisible security circuits, gas sensors, biosensors, organic light emitting diodes, polymer light emitting diodes, antistatic coatings, cold heat mirrors, etc. [3]. Also some new applications of TCOs have been proposed recently such as holographic recording media, high refractive index wave

guide overlays for sensors and telecommunication applications, write once read-many-times memory chips, electronic ink etc. [4]. And lastly, the low-temperature deposition of TCOs onto poly(ethylene terephthalate) (PET), polyimides and other polymer substrates in roll-coating processes for touch-screen and infrared reflector applications are the recent challenges for the TCO industries [5].

1.1.1.2. p-type transparent conducting films

Although TCOs have a vast range of applications as mentioned above, very little work has been done on active device fabrication using TCOs [6, 7]. This is because most of the aforementioned TCOs are n-type semiconductors. But the corresponding p-type transparent conducting oxides (p-TCO), which are essential for junction devices, were surprisingly missing in thin film form for a long time until in 1997, when Kawazoe et al. from Tokyo Institute of Technology, Japan, reported p-type conductivity in a highly transparent thin film of copper aluminumoxide ($CuAlO_{2+x}$) [8]. This has opened up a new field in optoelectronics device technology, the so-called ‘‘Transparent Electronics’’ or ‘‘Invisible Electronics’’ [9], where a combination of the two types of TCOs in the form of a pn junction could lead to a ‘‘functional’’ window, which transmits visible portion of solar radiation yet generates electricity by the absorption of the UV part [8]. It must be mentioned here that the first report of a semitransparent p-type conducting thin film of nickel oxide (NiO) was published in 1993 by Sato et al. [10] from Kanazawa Institute of Technology, Japan. They observed about 40% transmittance of the NiO films in the visible region and when they tried to fabricate an all-TCO pin diode of the form p-NiO/i-NiO/i-ZnO/n-ZnO, the visible transmittance further reduced to almost 20%. Although this low transmittance was not favorable for superior device applications, the report was an important milestone in the field of “Transparent Electronics” and in the development of TCO technology.

1.1.2. Thin film solar cells

A thin-film solar cell, also called a thin-film photovoltaic cell, is a solar cell that is made by depositing one or more thin layers (thin film) of photovoltaic material on a substrate. The thickness range of such a layer varies from a few nanometers to tens of micrometers. Many different photovoltaic materials are deposited with various deposition methods on a variety of substrates. Thin-film solar cells commercially available are categorized according to the photovoltaic material used:

- Amorphous silicon (a-Si) and other thin-film silicon (TF-Si)
- Cadmium telluride (CdTe)
- Copper indium sulfide (CIS)
- Dye-sensitized solar cell (DSC) and other organic solar cells

The thin film materials for solar cells are semiconductors that overcome one limitation of crystalline silicon in that they have direct band gaps. This means that their light absorption coefficients are high, and much thinner films of material can be used to collect the same amount of light, making them less materials-intensive. With the exception of amorphous silicon, the thin film inorganic materials are compound p-type semiconductors, such as $Cu_2(In,Ga)(S,Se)_4$ (CIGS), $CuInS_2$ (CIS) and Cu_2ZnSnS_4 (CZTS). The power conversion efficiency record for laboratory scale CIGS devices has recently exceeded 20% for the first time [11]. Another key advantage of these materials compared to Si is their tolerance to defects and grain boundaries, which allows for less stringent quality requirements. The success of CIGS, CIS and CZTS is only diminished by the fact that they contain expensive and rare materials. The cost and availability of In is a particular issue that will become pressing in the context of the anticipated deployment of photovoltaics on terawatt scales [12, 13].

A typical thin-film device structure is shown in Figure 1.1, illustrated for the case of a CIS or CIGS device. The p-type materials discussed above form the ‘absorber’ layer in the device, the layer where incident light is absorbed resulting in the excitation of electrons. The photovoltaic effect occurs at the interface between the absorber layer and a transparent n-type

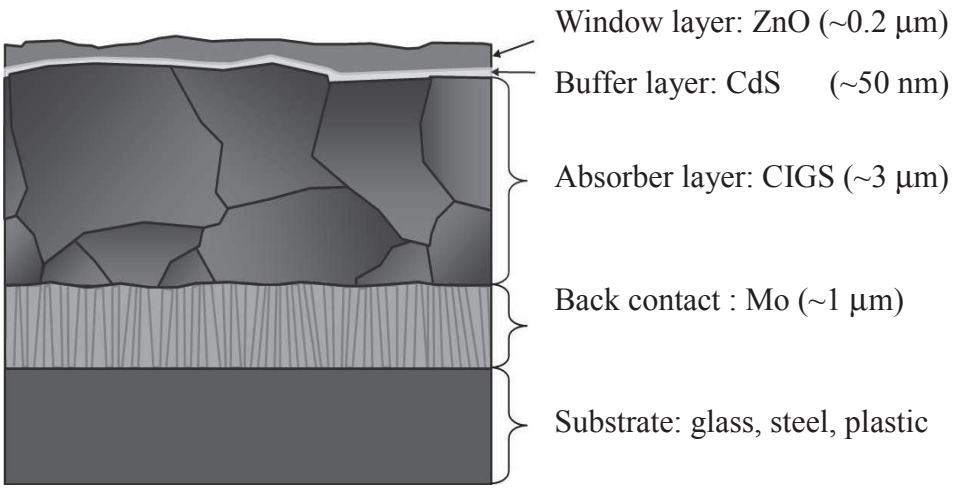

Fig. 1.1. Schematic cross-sectional diagram of a thin film photovoltaic cell, showing the layers that comprise it.

semiconductor. The n-type half of the device is actually composed of two layers, a 'buffer' layer of CdS which is very thin (~50 nm) and a thicker 'window' layer of ZnO. Electrical contact is made with the top of the device by addition of a transparent conducting oxide and metallic contact grid. The absorber layer is usually fabricated on a Mo-coated substrate, which provides mechanical strength and electrical contact to the back of the film.

1.2. Thin film deposition techniques:

Thin films could be prepared either with properties the same as that of their bulk counter parts or with properties different from bulk materials (size effects). The thickness of the thin films may be of the order of microns. Selection of process and process parameters influence the structure and composition which in turn alters the physical properties of the films. Single process cannot be used for all the materials. In general, the thin film deposition methods can be classified into two main categories; namely physical and chemical deposition techniques.

1.2.1. Physical deposition techniques:

In case of physical deposition methods, atoms are directly transported in a gas phase from the source material to be deposited onto the substrate forming a thin layer of solid.

1.2.1.1. Vacuum thermal evaporation:

In evaporation the substrate is placed inside a vacuum chamber, in which a block (source) of the material to be deposited is also located. The source material is then heated to the point where it starts to boil and evaporate. The material vapor finally condenses in form of thin film on the cold substrate surface and on the vacuum chamber walls. There are two popular evaporation technologies. In e-beam evaporation, an electron beam is aimed at the source material causing local heating and evaporation. In resistive evaporation, a tungsten pot, containing the source material, is heated electrically with a high current to make the material evaporate.

In general, vacuum evaporation offers the following advantages: High-purity films can be deposited from high-purity source material. Source of material to be vaporized may be a solid in any form and purity. The line-of-sight trajectory allows the use of masks to define areas of deposition on the substrate. Deposition rate monitoring and control are relatively easy. It is the least expensive of the PVD processes.

1.2.1.2. Sputtering technique:

Sputtering is a technology in which the material is released from the source at much lower temperature than evaporation. The substrate is placed in a vacuum chamber (discharge tube) with the source material, named a target, and an inert gas (such as argon) is introduced at low pressure. In this discharge tube a high energy voltage is given between the two electrodes creating the ionization of the argon ions. The positive argon ions move toward the cathode with a very high momentum and hit the target. The atoms, at the target surface, get momentum from the argon ion and come out in a vapor form and condense on all surfaces

including the substrate.

1.2.1.3. Molecular beam epitaxy (MBE):

Molecular beam epitaxy is the ultimate and most expensive technique. In this technique ideal condition is achieved by reducing the deposition rate to the lowest value, and creating the best vacuum of 10^{-6} or 10^{-7} Pa. It is ideally suited for depositing single crystal thin films atomic-layer by layer. MBE offers the following advantages: Surfaces and interfaces can be grown with excellent flatness (one atomic layer). Exact thickness control is possible. The ultra high vacuum chamber (UHV) of MBE enables the accomplishment of various in-situ characterizations.

1.2.1.4 Pulsed laser deposition (PLD)

Pulsed laser deposition (PLD) is a technique where a high power pulsed laser beam is focused inside a vacuum chamber to strike a target of the material that is to be deposited. This material is vaporized from the target (in a plasma plume) which deposits it as a thin film on a substrate (such as a silicon wafer facing the target). This process can occur in ultra high vacuum or in the presence of a background gas, such as oxygen which is commonly used when depositing oxides to fully oxygenate the deposited films.

1.2.2. Chemical deposition techniques:

Generally in chemical deposition methods, thin films are formed by chemical reaction on the surface of substrate

1.2.2.1. Chemical vapor deposition (CVD):

CVD is a widely used method for depositing thin films of a large variety of materials. In

a typical CVD process, reactant gases (often diluted in a carrier gas) enter the reaction chamber. The gas mixture is heated as it approaches the deposition surface. Depending on the process and operating conditions, the reactant gases may undergo homogeneous chemical reactions in the vapor phase before striking the surface.

Advantages of chemical vapor deposition are as follows: high purity films, economical, uniform thickness of films, high density films, excellent conformity and step coverage, good control of film composition. Disadvantages of chemical vapor deposition are: expense of reactants, use of hazardous chemicals, restricted to reactants in gas state.

1.2.2.2 Photochemical deposition (PCD)

The photochemical deposition (PCD) has been developed to deposit a variety of metals, metal oxides, sulfides and selenides thin films from an aqueous solution using UV light. It can be carried out at ambient temperature, from simple precursor compounds. PCD method consists of the direct irradiation of precursor bath with UV light. As indicated in Figure 1.2,

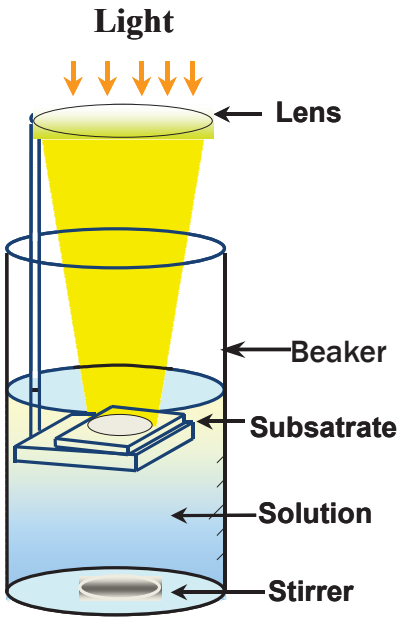

Fig. 1.2. Schematic diagram of the PCD method

the advantages of PCD are its simplicity, cheapness, low cost of the starting materials, better controllability and capability of large area deposition. The problem associated with PCD is low deposition rate. It was also observed that the substrate position affects the deposited film thickness and it is difficult to control this position precisely. Overall, for low temperature, damage-free deposition, PCD processes is increasingly important.

1.2.3 Electrochemical deposition (ECD)

The basic mechanism involved in this technique is the reaction of ions at the surface of substrate, controlled by an external applied potential /current. Ions that are solvated in a liquid medium arrive at the surface by a diffusive motion or a convective motion, depending on the experimental conditions. At the surface of the substrate, the ion is reduce resulting in an absorbed atom, which migrates to an energetically favorable site. For voltage controlled experiments, the continuity of this mechanism over the entire surface leads to the formation of a density of nuclei and the establishment of a macroscopic electrical current through the electrochemical cell. The current measured through the electrochemical cell can be directly related to the formation of the deposit. The continuous aggregation of atoms on the growing front results in deposits with structural and morphological properties strongly dependent on the electrodeposition parameters. Figure 1.3 shows schematic of a standard three-electrode cell used for deposition.

This technique has many advantages:

It requires simple equipment.

It can be performed at near room temperature and atmospheric pressure.

It is easily scaled to cover large areas.

The main disadvantage of the ECD technique is the relatively low quality of the deposited film.

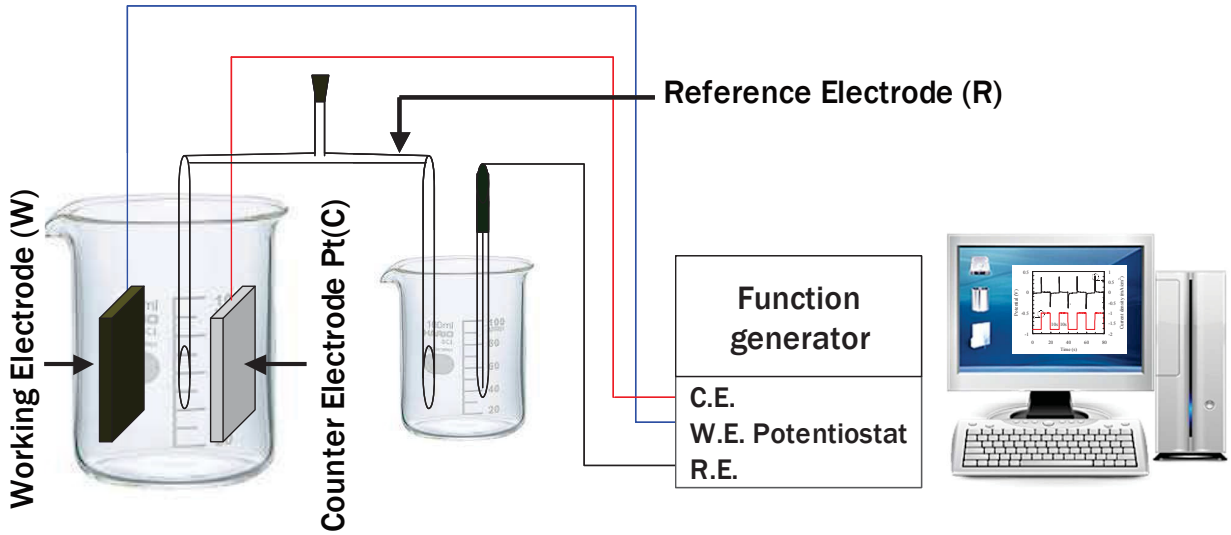

Fig. 1.3. Schematic diagram of the 3-electrode cell apparatus used for electrochemical deposition of thin films.

1.2.2.3.1 ECD techniques according to the nature of applied field

ECD techniques can be classified according to the nature of the applied potential to the substrate: a) galvanostatic, b) potentiostatic, c) pulsed source.

a) Deposition at a constant DC current (galvanostatic)

The constant current between the working and counter electrodes required for electrodeposition at a constant direct current can be obtained from a galvanostat. The initial guide line for choosing the required deposition current density can be obtained from the knowledge of (1) faradic efficiency and (2) the maximum permissible growth rate for a good crystal. The former can be obtained by a series of preliminary deposition experiments. The latter is to be obtained from available crystal growth data. The galvanostatic deposition of compound semiconductors is more complex, and a straightforward answer for the proper choice of deposition current is not possible. Compound semiconductors are usually

electrodeposited by the transport of at least one of the constituents under diffusion control. The simplest situation is when the deposition of all the components is diffusion-controlled. The rates of depositions will then be directly proportional to the corresponding limiting current densities (and hence the corresponding bulk concentrations).

b) Deposition at a constant DC potential (potentiostatic)

In potentiostatic (i.e. constant DC potential) ECD, different charge transfer reactions occur at rates appropriate to the steady state interfacial overpotential and exchange current density. The choice of overpotential is dictated by the composition of the bath, the substrate, and in practice the actual deposition potential depends on a number of factors such as substrate-deposite interaction, the hydrogen overvoltage, the interaction between the components during compound deposition, and the polarization characteristics of the bath. Potentiostatic deposition is carried out under either pure activation, diffusion, or mixed control depending on the choice of the deposition potential.

Constant potential deposition is usually carried out using a potentiostat to control the potential of the working electrode as shown in Figure 1.3. A three electrode cell with a working electrode (W), a reference electrode (R), and a counter electrode (C). For reliable measurement of the working electrode potential, the reference electrode should be kept close to it to minimize the ohmic drop within the electrolyte.

Potentiostatic DC deposition has been used to grow layers of large number of elemental, binary, and ternary semiconductors. For elemental semiconductors, the use of low overpotential generally helps in the formation of a small number of nuclei that grow independently of each other until they are sufficiently large to coalesce or join at the grain boundary. However, very low overpotential may not be suitable as they may lead to a spongy or porous deposit due to low nucleation rates. As the overpotential is increased, the super saturation increases and a large number of nuclei are formed. The deposit thus acquires a fine-grained morphology. Very high overpotential may however, lead to the growth of

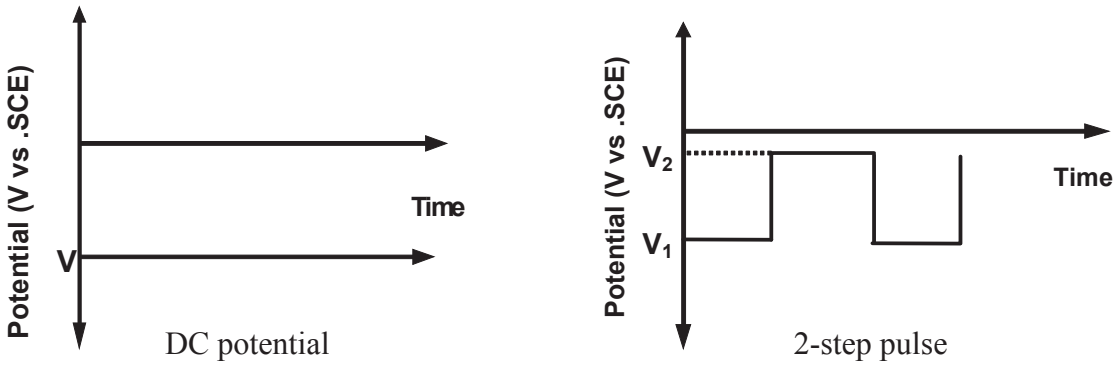

Fig. 1.4. Electrochemical deposition techniques according to the nature of applied field.

whiskers or dendrites. In the case of compound semiconductors, more stringent control of the deposition potentials is required to maintain the deposit stoichiometry. The optimum deposition potential is governed by the interplay of a number of complex factors.

c) ECD by a periodic or pulsed source

The use of non-DC signals for ECD is known to improve the deposit quality. However, it attracts the attention just recently especially for the applications of semiconductor electrodeposition. Non-DC ECD can be carried out by varying either the current or the overpotential.

Some of the merits of non-DC ECD are summarized below:

In DC ECD, one can vary only one parameter; the current or the potential. In non-DC ECD at least three parameters can be varied. For example in periodic (two step) deposition one can change the reduction potential (V_R), and the oxidation potential (V_O), the reduction duration (t_R) of the deposition cycle and the oxidation duration (t_O) of the deposition cycle.

Non-DC ECD is usually accompanied by the process of ECD, surface transformation and electropolishing. For example during the anodic cycle of the pulse, adsorption, desorption, and recrystallization of the deposit occur. The properties of the deposits can thus be greatly

altered by suitably choosing the pulse duty cycle or the anodic and cathodic portion of the waveform. Figure 1.4 shows the deposition potential forms that will be used in this thesis. In chapter 3 a comparison of the DC and the pulsed deposition of $Cu_2ZnSnS_{4-x}O_x$ (CZTSO) will be given.

1.2.2.3.2 Cyclic voltammogram

The most effective tool for analyzing the electrochemical processes is to use a voltammogram. In cyclic voltammetry the current response of an electrochemical system is monitored with the application of a triangular potential sweep. A typical experiment requires a function generator, potentiostat, and recorder or data acquisition system. The function generators modulates the output of the potentiostat so that one can apply a cyclic linear ramp with a desirable slope and modulate the working electrode potential between two voltage limits. In this thesis, cyclic voltammetry is used as an initial step to have an idea about the suitable oxidation and reduction potential of a certain compound [14]. As shown in Figure 1.5, voltammograms present the current plotted against electrode potential.

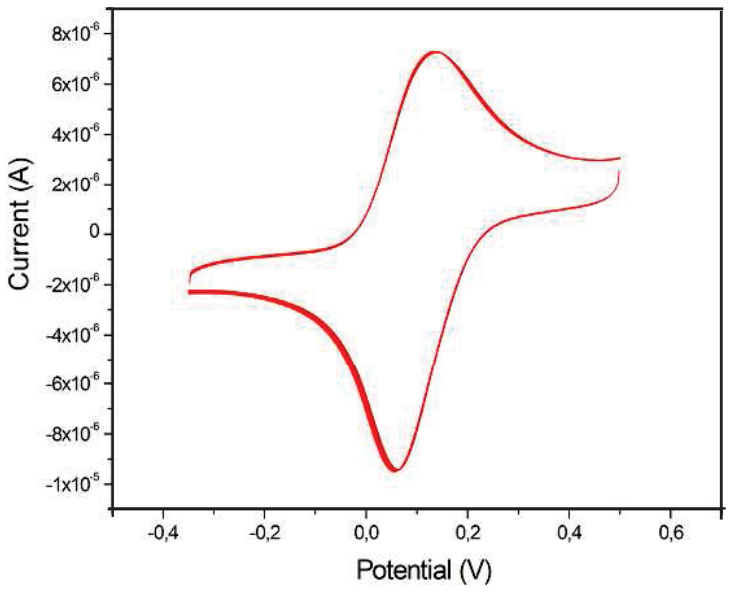

Fig. 1.5. Representative cyclic voltammogram

1.3 Photoelectrochemical (PEC) measurement

To determine the type of conduction and to estimate the photosensitivity, the photoelectrochemical (PEC) measurements were carried out. The PEC measurements were performed using the same three-electrode cell with the light incident from a xenon lamp toward the backside of the sample (working electrode) as shown in Figure 1.6. The three-electrode cell with a solution containing 100 mM $Na_2S_2O_3$ was used. The incident light (about 100 mW/cm^2) was turned off and on mechanically every 5 s by inserting and removing a barrier between the lamp and the sample, respectively (i.e., a 200 mHz periodic pulse of light). This light chopping was performed under the application of a ramp voltage between the working and reference electrode. This measurement was accomplished through two different voltage range; first in the anodic bias range (from 0 to +1 V) and then in the cathodic bias range (from 0 to –1 V). Under illumination, some carriers were excited in the illuminated region of the deposited thin film. The excited minority carriers then diffused to the surface during their lifetime to participate in the electrochemical reaction at the film/electrolyte interface. For example, if the current becomes more negative under the light illumination during the cathodic and anodic biasing, then the minority carriers generated here are electrons, and the deposited film is p-type.

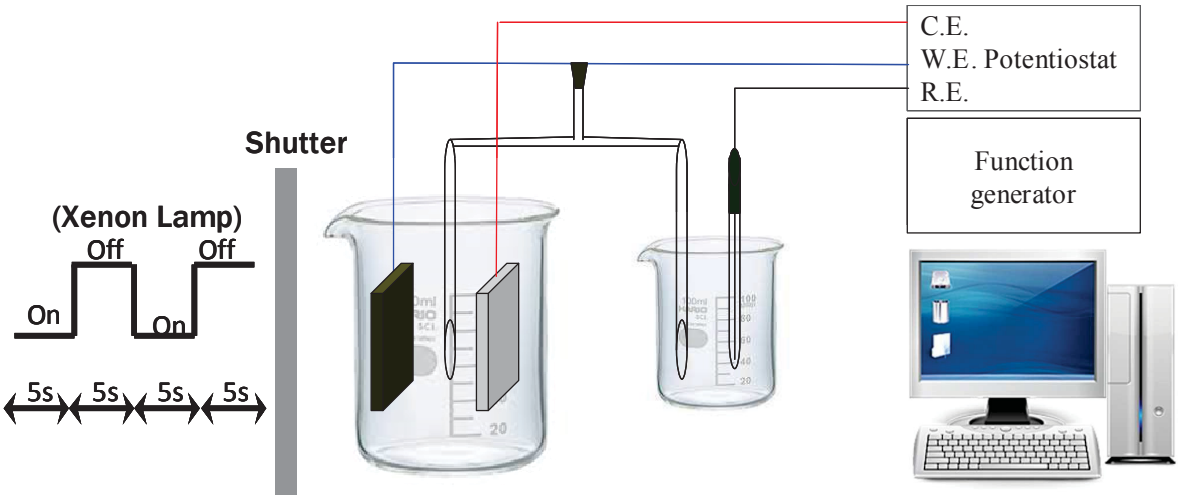

Fig. 1.6. A schematic diagram of the 3-electrode cell apparatus used for photoelectrochemical (PEC) study of the deposited film.

1.4. Basic properties of the materials

1.4.1. Basic properties of Cu_2S

Cu_xS is a p-type semiconductor and has been traditionally applied for solar cells combined with CdS. Application for IR-absorbing [15] and electro conductive coatings [16] are also considered as promising. Cu_xS is one of typical nonstoichiometric compounds and does not have a fixed composition ratio x. This is basically because the oxidation number of Cu can be either +1 or +2 [17]. Many different phases with different composition ratios are known, and the reported indirect band gap values are scattered in a range between 1.0 and 1.5 eV, and the direct band gap values in a range between 1.7 and 2.5 eV [18]. Cu_xS thin films have been fabricated by various methods including chemical techniques, such as chemical bath deposition (CBD) [19], PCD [20], spray pyrolysis [21], ECD [22].

1.4.2. Basic properties of Cu_2ZnSnS_4

Cu_2ZnSnS_4 (CZTS) is notionally derived from $CuInS_2$ (CIS) by substitution of two In atoms for one Zn and one Sn atom. This isoelectronic substitution produces a material with many of the same properties of the parent compound, but it does not contain any rare or expensive elements. The desirable properties include p-type conductivity, a high absorption coefficient and band gap of around 1.5eV (the theoretical optimum value for solar energy conversion [23]). Another advantage of the similarity between CZTS and CIS is that CZTS may be substituted directly into the standard device structure (Figure 1.1). The quaternary Cu-Zn-Sn-S system is also interesting from the viewpoint of fundamental science, as it further increase the complexity of the defect chemistry and electronic structure, while providing additional opportunities for materials optimization by control of stoichiometry compositional gradients. The compound $Cu_2ZnSnSe_4$ (CZTSe) is derived similarly, and has a band gap of around 0.9 eV [24]. The alloying of CZTS and CZTSe to from a pentanary system is another aspect that is already being explored. Oxygen is another group VI element and can replace S in CZTS without disturbing valence. Therefore, $Cu_2ZnSnS_{4-x}O_x$ (CZTSO) can also be suitable

for thin film solar cells.

The potential of CZTS was recognized around 20 years ago by Ito and Nakazawa, who prepared films by atom beam sputtering of a synthetic CZTS powder source and demonstrated a photovoltaic effect at the junction between CZTS and cadmium-tin-oxide [25]. In the following decades, Katagiri et al made steady improvements in device efficiency, which reached 6.7% in 2007 for a co-sputtered CZTS film that was annealed for three hours with H_2S [26]. Very recently there has been huge growth in the number of publications relating to CZTS and CZTSe, with a great variety of techniques employed to synthesis and study them. The current best device efficiency is a very promising 11.1% for a $Cu_2ZnSn(S,Se)_4$-base device, which is even more interesting given that this film was synthesized using a solution-base method to deposit a precursor followed by heating with sulfur [27].

1.4.3. Basic properties of FeS_2

The mineral pyrite, or iron pyrite, also known as fool's gold, is an iron sulfide with the formula FeS_2. This mineral's metallic luster and pale brass-yellow hue give it a superficial resemblance to gold, hence the nickname fool's gold. Iron sulfide exists in several distinct forms, which differ in the ratio of sulfur to iron and denomination: Pyrrhotite ($Fe_{1-x}S$), Troilite (FeS), Mackinawite ($Fe_{1+x}S$), Pyrite and Marcasite (FeS_2), Greigite (Fe_3S_4), respectively.

FeS_2 has attracted much interest in various fields, such as photoelectrochemical and photovoltaic solar cells [28-30], batteries [31], photoemission [32], and photodiodes [33-36], due to its strong light absorption ($\alpha > 10^5$ cm $^{-1}$) [37] and a suitable bandgap (Eg = 0.95 eV), More importantly, earth abundance (iron is the fourth most abundant element in the earth's crust), low-cost and non-toxicity of FeS_2 make it excellent candidates for developing cost-effective optoelectronic devices instead of inorganic semiconductors that possess non-sustainable elements. Many methods have been used for the preparation of thin pyrite films, such as low pressure chemical vapor deposition [38], spray pyrolysis [39], sulfurization

of electrodeposited films [40, 41], sulfurization of sputtered [42] or vacuum evaporated [43, 44] iron films, sol-gel [45, 46], and chemical bath deposition [47]. More recently, use of ink technology is also reported, where precursor films of molecular inks composed of iron complexes and elemental sulfur were spin-coated and annealed [48].

1.5. Preview of this thesis

The purpose of this work is to fabricate thin films of new multinery semiconductors consisting of non-toxic and earth abundant elements by using inexpensive techniques, i.e., the ECD and PCD methods. As described in 1.3, the quaternary compound CZTS has been widely researched with a great variety of techniques employed for synthesis. In this work, CZTS and related multinery alloys were deposited. Moreover, we attempted to deposit Fe compound films as an even more environmentally friendly material than CZTS. We also explored the possibility of application of those films for, LED and thin film solar cell.

This thesis has five chapters. In the first chapter, a brief background was introduced on different thin films deposition techniques. The advantages and disadvantages of ECD were explained, and relevant techniques were described.

In the second chapter, we report the deposition of Cu_xZn_yS thin films on ITO glass substrate using the ECD and PCD methods from an acidic aqueous solution containing $Na_2S_2O_3$, $CuSO_4$ and $ZnSO_4$. The Cu_xZn_yS thin films have a wide band gap of about 3.2 eV and exhibit p-type conduction and photosensitivity. The ZnO/ Cu_xZn_yS heterojunction cells showed rectification properties. Thus, Cu_xZn_yS can be regarded as a new wide-gap p-type material. Cu_xZn_yS thin films deposited by ECD were annealed. The optical transmission increased with increasing annealing temperature.

In the third chapter, we describe the deposition of Cu-Zn-Sn-S-O (CZTSO) thin films using DC and 2-step pulsed ECD. P-type conductivity and photosensitivity of the films were

confirmed, and the pn heterojunction with ZnO showed rectification properties. CZTSO thin films deposited by pulsed ECD were sulfurized. After the sulfurization, the oxygen amount decreased clearly.

In the fourth chapter, we report deposition of iron sulfide oxide (FeS_xO_y) by the ECD method. The deposition solution contained $FeSO_4$ and $Na_2S_2O_3$. In the photoelectrochemical measurement, the deposited FeS_xO_y film showed p-type conduction and photoconductivity. The band gap was estimated to be 1.2 eV from the optical transmission result for a 0.5 μm-thick film. Moreover, a ZnO/ FeS_xO_y heterostructure was fabricated, and rectification properties were confirmed. After annealing, the Fe content did not vary significantly, but O and S contents depend on the annealing temperature. The optical transmission and the bandgap increased with increasing annealing temperature.

In the fifth chapter, we give conclusions of this work and suggestions for the future works.

References

[1] K. Badekar, Ann. Phys. (Leipzig) 22 (1907) 749.

[2] C.M. Lampert, Sol. Energy Mater. 6 (1981) 1.

[3] C.M. Lampert, Sol. Energy Mater. 21 (1990) 191.

[4] C. Grivas, S. Mallis, L. Boutsikaris, D.S. Gill, N.A. Vainos, P.J. Chandler, Laser Phys. 8 (1998) 326.

[5] R.L. Cornia, J.B. Fenn, H. Memarian, R. Ringer, Proceedings of 41st Annual Technical Conference, Boston, SVC, (1998) 452.

[6] C.H. Seager, D.C. McIntyre, W.L. Warren, B.A. Tuttle, Appl. Phys. Lett. 68 (1996) 2660.

[7] M.W.J. Prince, K.O. Gross-Holtz, G. Muller, J.B. Cillessen, J.B. Giesbers, R.P. Weening, R.M. Wolf, Appl. Phys. Lett. 68 (1996) 3650.

[8] H. Kawazoe, M. Yasukawa, H. Hyodo, M. Kurita, H. Yanagi, H. Hosono, Nature 389 (1997) 939.

[9] G. Thomas, Nature 389 (1997) 907.

[10] H. Sato, T. Minami, S. Takata, T. Yamada, Thin Solid Films 236 (1993) 27.

[11] P. Jackson, D. Hariskos, E. Lotter, S. Paetel, R. Wuerz, R. Menner, W. Wischmann and M. Powalla, Prog. Photovolt: Res. Appl. 19 (2011) 894.

[12] M. A. Green, Prog. Photovolt: Res. Appl. 17 (2009) 347.

[13] A. Feltrin, A. Freundlich, Renewable Energy 33 (2008) 180.

[14] R.K. Pndey, S. N. Sahu, S. Chandra, Handbook of Semiconductor Electrodeposition (Marcel. Dekker, Inc, USA 1996) Chapter 5.

[15] P. Nair and M. Nair, J. Phys. D: Appl. Phys. 24 (1991) 83.

[16] T. Yamamoto, E. Kubota, A. Taniguchi, S. Dev, K. Tanaka, and K. Osakada, Chem. Mater. 4 (1992) 570.

[17] I. Grozdanov, C. K. Barlingay, S. K. Dey, M. Ristov, M. Najdoski, Thin Solid Films 250 (1994) 67.

[18] A.C. Rastogi and S. Salkalachen, Thin Solid Films 97 (1982) 191.

[19] I. Grozdanov, C. K. Barlingay, S.K. Dey, M. Ristov, and M. Najdoski, Thin Solid Films 250 (1994) 67.

[20] J. Podder, R. Kobayashi, and M. Ichimura, Thin Solid Films 472 (2005) 71.

[21] C. Naşcu, I. Pop, V. Ionescu, E. Indrea, I. Bratu, Mater. Lett. 32 (1997) 73.

[22] J. Vedel, P. Cowache and D. Lincot, Solar Cells 11 (1984) 241.

[23] K. Sekiguchi, K. Tanaka, K. Moriya, H. Uchiki, Phys. Stat. Sol. 3 (2006) 2618.

[24] G. Zoppi, I. Forbes, R. W. Miles, P. J. Dale, J. J. Scragg and L. M. Peter, Progress in Photovoltaics: Research and Applications 17 (2009) 315.

[25] Ito, K. and T. Nakazawa, Jpn. J. Appl. Phys. 27 (1988) 2094.

[26] H. Katagiri, K.Jimbo, S. Yamada, T. Kamimura, W.S. Maw, T. Fukano, T. Ito and T. Motohiro, Appl. Phys. Express 1 (2008) 041201.

[27] T. K. Todorov, K. B. Reuter, D. B. Mitzi, Adv. Mater. 22 (2010) E156.

[28] W. Jaegermann, H. Tributsch, J. Appl. Electrochem. 13 (1983) 7.

[29] A. Ennaoui, H. Tributsch, Solar Cells 13 (1984) 197.

[30] F. Alharbi, J. D. Bass, A. Salhi, A. Alyamani, H. C. Kim, R. D. Miller, Renewable Energy 36 (2011) 2753.

[31] Y. Shao-Horn, S. Osmialowski, Q. C. Horn, J. Electrochem. Soc. 149 (2002) A1499.

[32] A. Fujimori, K. Mamiya, T. Mizokawa, T. Miyadai, T. Sekiguchi, H. Takahashi, N. Mori, S. Suga, Phys. Rev. B 54(1996) 16329.

[33] D. Y. Wang, Y. T. Jiang, C. C. Lin, S. S. Li, Y. T. Wang, C. C. Chen, C. W. Chen, Adv. Mater. 24 (2012) 3415.

[34] I. J. Ferrer, C. Sanchez, J. Appl. Phys. 70 (1991) 2641.

[35] J. Puthussery, S. Seefeld, N. Berry, M. Gibbs, M. Law, J. Am. Chem. Soc. 133 (2010) 716.

[36] M. Cabán-Acevedo, M. S. Faber, Y. Tan, R. J. Hamers, S. Jin, Nano Lett. 12 (2012) 1977.

[37] P. Altermatt, T. Kiesewetter, K. Ellmer, H. Tributsch, Solar Energy Mater. Solar Cells 71 (2000) 14.

[38] D.M. Schleich, H.S.W. Chang, J. Cryst. Growth 112 (1991) 737.

[39] A. Yamamoto, M. Nakamura, A. Seki, E.L. Li, A. Hashimoto, S. Nakamura, Sol. Energy

Mater. Sol. Cells 75 (2003) 451.

[40] G. Pimenta,W. Kautek, Thin Solid Films 238 (1994) 213.

[41] S. Nakamura, A. Yamamoto, Electrodeposition of pyrite (FeS_2) thin films for photovoltaic cells, Sol. Energy Mater. Sol. Cells 65 (2001) 79.

[42] L. Meng, J.P. Tu, M.S. Liu, Mater. Lett. 38 (1999) 103.

[43] B. Rezig, H. Dahman, M. Kenzari, Renewable Energy 2 (1992) 125.

[44] I.J. Ferrer, C. Sanchez, J. Appl. Phys. 70 (1991) 2641

[45] H. Siyu, L. Xinyu, L. QingYu, and C. Jun, J. of Alloys and Comp. 472 (2009) L9.

[46] L. Huang, F. Wang, Z. Luan, and L. Meng, Materials Letters 64 (2010) 2612.

[47] D. A. Maz´on-Montijo, M. T. S. Nair and P. K. Nair, Journal of Solid State Science and Technology 2 (11) (2013) P465.

[48] S. Seefeld, M. Limpinsel, Y. Liu, N. Farhi, A. S. Weber, Y. Zhang, N. Berry, Y. J. Kwon, C. L. Perkins, J. C. Hemminger, R. Wu, M. Law, J. Am. Chem. Soc. 135 (2013) 4412.

Chapter 2
Fabrication of Transparent p-type Cu_xZn_yS Thin Films by the Electrochemical and Photochemical Deposition Methods

2.1 Introduction

Cu_xS (x=1~2) is a p-type semiconductor and has been traditionally applied for solar cells combined with CdS. Application for IR-absorbing [1] and electro conductive coatings [2] are also considered as promising. Cu_xS is one of typical nonstoichiometric compounds and does not have a fixed composition ratio x. This is basically because the oxidation number of Cu can be either +1 or +2 [3]. Many different phases with different composition ratios are known, and the reported indirect band gap values are scattered in a range between 1.0 and 1.5 eV, and the direct band gap values in a range between 1.7 and 2.5 eV [4]. Cu_xS thin films have been fabricated by various methods including chemical techniques, such as chemical bath deposition (CBD) [1,3,5-8], photochemical deposition (PCD) [9], spray pyrolysis [10], electrochemical deposition (ECD) [11-14]. On the other hand, ZnS is an n-type semiconductor material, and its direct band gap was reported to be 3.6 eV. It has been well-known as an electroluminescence material and more recently been applied for buffer layers of solar cells [15-16]. ZnS thin films can also be prepared by different chemical techniques, such as CBD [15-19] and ECD [20, 21].

In this work, we attempt to deposit Cu_xZn_yS thin films by ECD and PCD. Cu_xZn_yS can be considered as an alloy of Cu_xS and ZnS. Therefore, one may expect that it possibly becomes p-type or n-type, and that its band gap energy may be in a range between those of two constituent compounds. Thus, Cu_xZn_yS can be a promising material for a variety of optical device applications, such as electroluminescent and photoconductor devices and photovoltaic cells. It should be noted that since Cu_xS is a nonstoichiometric compound, Cu_xZn_yS can be considered as a nonstoichiometric alloy. Thus, the metal/S ratio will not be

fixed and the composition is given by two variables, x and y, unlike III-V and II-VI ternary (pseudo-binary) alloys such as $Al_xGa_{1-x}As$ and $Zn_xCd_{1-x}S$, for which the alloy composition is given by a single variable x. So far, there are very few reports on thin film deposition of this material. Yildirim, et al. fabricated $Cu_{0.6}Zn_{0.4}S$ thin films by successive ionic layer absorption and reaction (SILAR) [22]. The band gap of their films was in a range of 1.85-2.14 eV, and the conduction type was not reported. More recently, the spray pyrolysis method for Cu-Zn-S (CZS) films is also reported, The band gap of CZS films was varied in the range of 1.8 - 3.5 eV when the Cu/(Cu+Zn) ratio was increased from 0 to 67 %. By the Hall-effect measurement using a CZS film with Cu/(Cu+Zn) 50 %, the CZS was a p-type semiconductor [23]. We give characterization results for Cu_xZn_yS deposited from aqueous solutions containing lactic acid. Moreover, we discuss annealing effects for Cu_xZn_yS in a nitrogen atmosphere for an hour at different temperature, namely 100, 200, 300 and 400°C. Then, a detailed characterization for the as-deposited as well as the annealed films has been performed.

2.2 Experimental procedure

A three-electrode cell was used for ECD with a saturated calomel electrode (SCE) as the reference electrode (The potential of SCE is at 0.241 V vs. SHE, standard hydrogen electrode.) Indium-tin-oxide (ITO)-coated glass was used as the working electrode (substrate) and a platinum sheet was used as the counter electrode. In the following, all the potential values are vs SCE. Hokuto Denko function generator HB-104 and potentiostat/ galvanostat HA-301 were used in the deposition. Both the ITO substrate and the platinum sheet were washed ultrasonically in alky benzene and dried in nitrogen before the experiment. The deposition area was about 1x1 cm^2. An aqueous bath containing 100mM $Na_2S_2O_3$ and 10 mM $CuSO_4$ was used for the Cu_xS deposition. The volume of the deposition solution is 50 ml. The pH of the solution was adjusted to 2.5 by adding 2 ml of lactic acid. Lactic acid is a weak acid with acidity constant pK_a of 3.86, and it is known that lactic acid can act as a pH buffer during ECD [25,26]. The deposition time is 30 min, and the deposition temperature is varied from room temperature to 60ºC. After selecting the optimum deposition temperature (40ºC), we

examined deposition with different lactic acid amounts (1 - 5 ml). For Cu_xZn_yS deposition, we used an aqueous bath containing 100mM $Na_2S_2O_3$, 25~0.75 mM $CuSO_4$ and 5~29.25 mM $ZnSO_4$. We fixed the sum of the concentrations of $ZnSO_4$ and $CuSO_4$ at 30 mM, and varied the Zn/Cu ratio. The amount of lactic acid was fixed at 2ml, and the temperature at 40 ˚C on the basis of the results of Cu_xS deposition. The deposition potential was set at -0.90 V, and the deposition time was 20 min. It should be noted that all the above deposition potential was determined on the basis of the cyclic voltammetry (CV). The cathodic scan was from 0 to -1.5V and the anodic scan was from -1.5V to +0.5V with a scan rate of 20mV/s. After the experiment, the deposited films were washed in pure water and naturally dried in air.

Cu_xS and Cu_xZn_yS are expected to be formed by the following mechanism, as reported for other sulfides [27,28]. Elemental sulfur is released from $S_2O_3^{2-}$ by the reaction.

$$S_2O_3^{2-} + 2H^+ = S + H_2SO_3. \quad [1]$$

The stabilized pH would lead to stable sulfur supply according to reaction [1]. Cu_xS is expected to be formed at the cathode by the reaction

$$xCu^{2+} + S + 2x\,e^- = Cu_xS. \quad [2]$$

Cu_xZn_yS is expected to be formed at the cathode by the reaction

$$xCu^{2+} + yZn^{2+} + S + 2(x + y)e^- = Cu_xZn_yS. \quad [3]$$

Cu_xZn_yS thin films were also deposited by the PCD method. $CuSO_4$, $ZnSO_4$ and $Na_2S_2O_3$ were dissolved into 50ml pure water, and the pH value was adjusted by H_2SO_4 or NaOH. Thus, $CuSO_4$ and $ZnSO_4$ are the source of Cu and Zn, while $Na_2S_2O_3$ is the source of S, as well as the reducing agent.

ITO-coated glass sheet was used for the substrate. Acetone was used for cleaning and degreasing the substrate. As indicated in the previous chapter-1 (see Figure 1.2), the substrate was immersed in the sample solution to a depth of about 2~3mm from the solution surface, and irradiated by the light of an ultra-high-pressure mercury arc-lamp through a lens. The concentration, pH, light irradiation time were varied to explore the conditions for PCD

deposition. The light intensity is about 1000mW/cm^2. The deposition solution contained 300mM $Na_2S_2O_3$, 5 mM $CuSO_4$ and 25 mM $ZnSO_4$, and pH value was set to 3.0 by adding H_2SO_4. An about 0.2 μm-thick transparent film was obtained with 60 min deposition. After deposition, the sample was washed with pure water and dried naturally.

Compositional analysis was carried out by Auger electron spectroscopy (AES) using a JEOL JAMP 9500 and 7800 Auger microprobe at a probe voltage of 10 kV and a current of 10 nA. Mapping images of Auger signals were obtained from the intensities of electrons with particular kinetic energies. Argon ion etching with an acceleration voltage of 3 kV and a current of 8 mA was used to sputter the film surface. The Cu/S and Zn/S atomic ratios were calculated using standard CuS and ZnS compounds, respectively. The scanning electron microscope (SEM) observation was also performed using JEOL JAMP 9500 at a constant acceleration voltage of 10 kV and a magnification of 6000. The films thickness was measured by an Accretech Surfcom-1400D profile meter. The optical transmission measurement was performed using a JASCO U-570 spectrometer with the substrate as the reference. X-ray diffraction (XRD) was measured using a Rigaku Smartlab diffractometer with a Cu Kα radiation source. Raman spectra were measured using a JASCO NR-1100 spectrometer with the 488 nm line of the Ar ion laser as an excitation source in a quasi-backscattering configuration. Furthermore, to determine the type of conduction and to estimate the photosensitivity, photoelectrochemical (PEC) measurements were carried out using the same potentiostat as used for the deposition. The three-electrode cell with a solution containing 100 mM $Na_2S_2O_3$ was used. The light was incident from a xenon lamp toward the backside of the sample. The incident light (about 100 mW/cm^2) was turned off and on mechanically every 5 s by inserting and removing a barrier between the lamp and the sample. This light chopping was performed under the application of a ramp voltage, first in the cathodic bias range (0 to -1 V) and then in the anodic bias range (0 to +1 V).

ZnO was also deposited by ECD using an aqueous solution containing 0.1 M $Zn(NO_3)_2$ [29]. The deposition temperature was 60ºC. The deposition bias was a two-step pulse with V_1

= -1.3V and V_2 = -0.6 V, and the duration of each pulse was 10s. The deposition time was 2 min, and the film thickness was about 0.5 μm. Indium was evaporated as electrodes on the ZnO/ Cu_xZn_yS / ITO structure.

2.3. Results and discussion

2.3.1 ECD of Cu_xZn_yS

First, we investigated Cu_xS thin film deposition. The optimum deposition condition was determined as follows: $Na_2S_2O_3$: 100 mM, $CuSO_4$: 20 mM, lactic acid: 2 ml, deposition potential: -0.45 V, and temperature: 40 ˚C. Figure 2.1 shows an example of the AES spectra for Cu_xS under the optimum condition. Figure 2.2 shows the surface morphology of the Cu_xS film deposited under the optimum condition. Particles are seen on the surface of a compact, continuous film. The result of Raman spectra is shown in Figure 2.3. Scattering due to the longitudinal-optical (LO) phonon of Cu_xS was observed near 471cm^{-1}. Thus it is confirmed that the Cu_xS compound was synthesized.

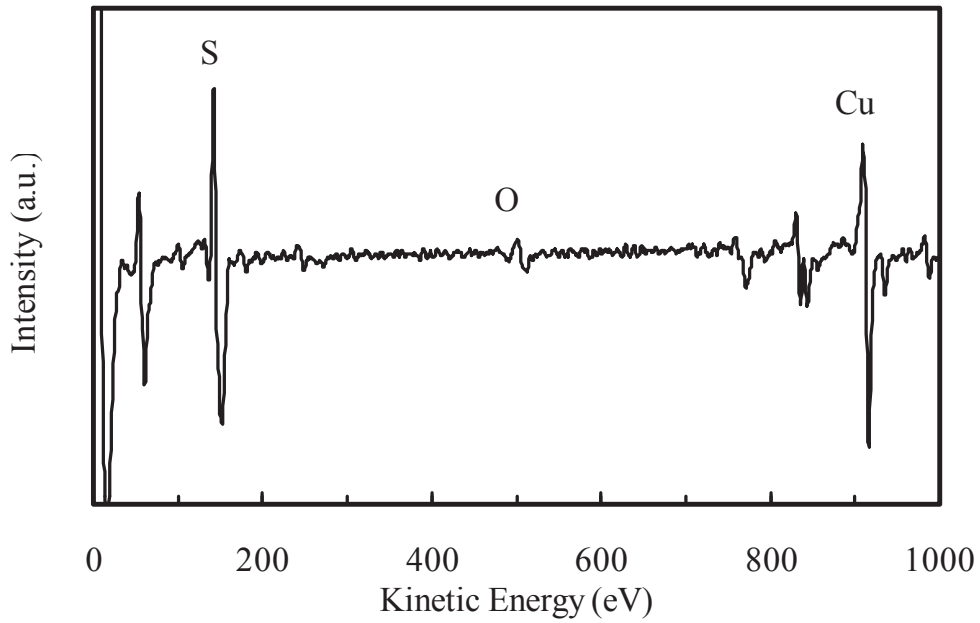

Fig. 2.1. AES spectra for the Cu_xS thin film.

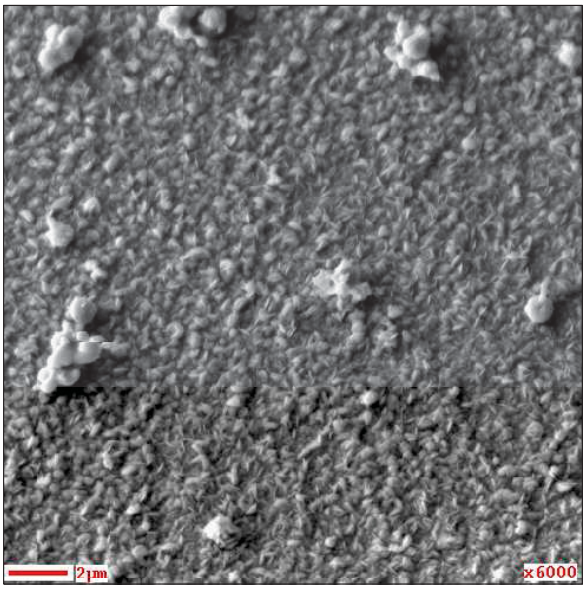

Fig. 2.2. SEM micrographs of the surface of the Cu_xS thin film.

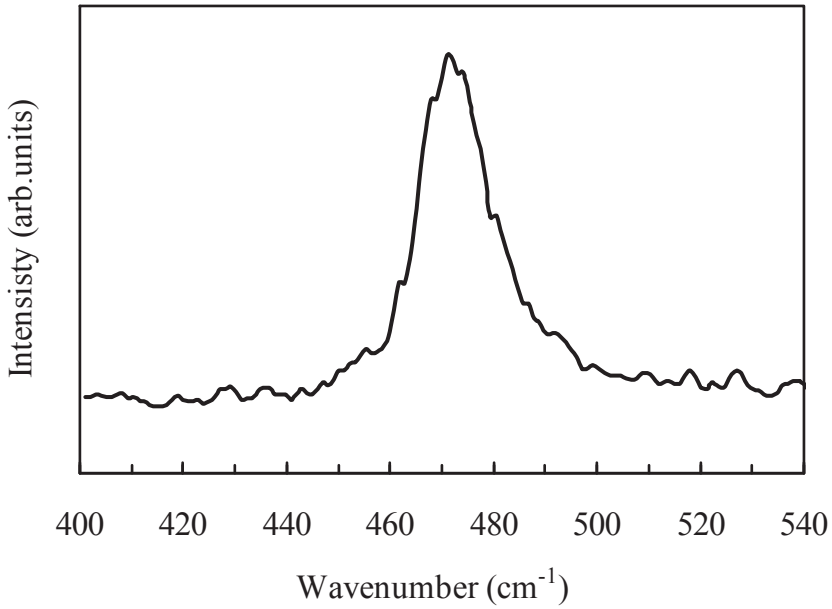

Fig. 2.3. Raman spectrum of the Cu_xS thin film.

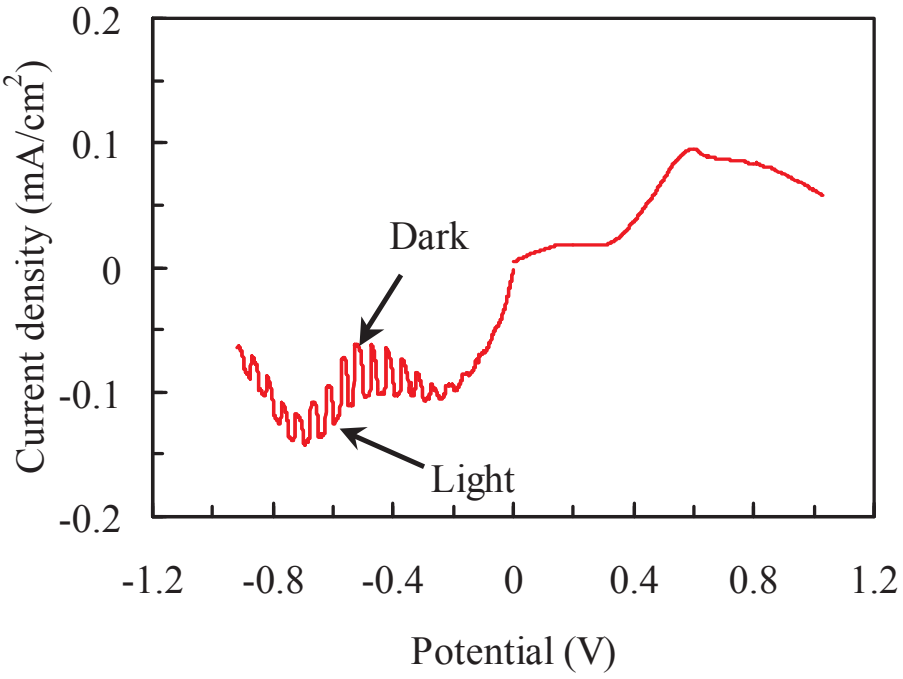

Fig. 2.4. PEC measurement results for the Cu_xS thin film.

Figure 2.4 shows the results of the PEC measurement for the Cu_xS sample deposited under the optimum condition. The step-form variation in the current is due to the turning on/off of the illumination. By the illumination of the films, carriers were excited, and the excited minority carriers diffused to the surface during their lifetime to participate in the electrochemical reaction at the film/electrolyte interface. Since the photocurrent is negative, the minority carriers generated here are electrons. Thus, the deposited film is p-type and show photosensitive behaviors. Lactic acid is an organic acid, ionizing slowly in the aqueous solution, and acts as a buffer reagent to stabilize pH of the solution. The stabilized pH would lead to stable sulfur supply according to eq.(1) and improvement of the sulfide deposition.

Figure 2.5 shows the optical transmission spectrum of the film deposited under the optimum condition. The absorption edge was observed near 500nm. The optical energy band gap was calculated from the classical relation for direct-band optical absorption,

$$\alpha = k(h\nu - E_g)^{1/2} / h\nu, \qquad [4]$$

where k is a constant, E_g is the band gap, and $h\nu$ is the photon energy. The plot in Figure 2.6 shows that the band gap deduced from the spectrum is 2.1 eV (for a 0.4 μm-thick film), which agrees fairly well with those previously reported for Cu_xS films deposited by chemical techniques [3-11]. We attempted to calculate the indirect bandgap, but the plot of $(\alpha h\nu)^{1/2}$ vs. hν does not give a reasonable value of E_g.

On the basis of the results for Cu_xS, the pH of the solution was adjusted using lactic acid for Cu_xZn_yS deposition. We fixed the sum of the concentrations of $ZnSO_4$ and $CuSO_4$ at 30 mM, and varied the Zn/Cu ratio. $Na_2S_2O_3$ concentration was fixed at 100mM, and the temperature at 40 ˚C. First, for Zn/Cu = 0.5, the CV measurement was carried out, and the deposition potential was set at -0.90 V. The solution was stable for Zn/Cu>1, but precipitation was spontaneously formed for Zn/Cu<1. Thus, for films deposited at Zn/Cu<1, we carried out only AES and not other characterizations. The solution condition and film compositions are listed in Table 2.1.

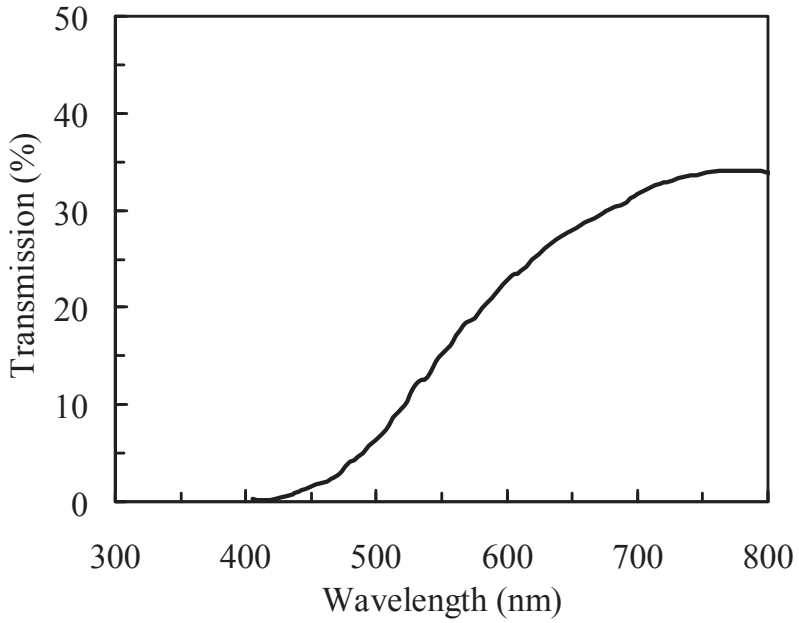

Fig. 2.5. Optical transmission spectrum for the Cu_xS thin film.

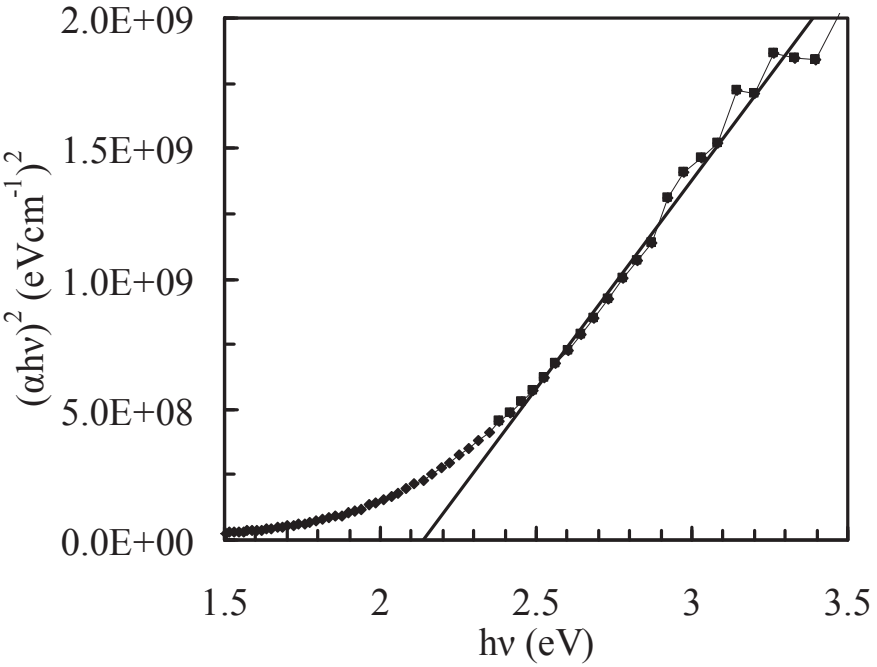

Fig. 2.6. Estimation of the band gap for the Cu_xS thin film.

Figure 2.7 shows the SEM image of the Cu_xZn_yS film (Zn/Cu ratio in the solution =4). The film thickness was about 0.1 μm and did not significantly depend on the concentration ratio. The film exhibited some surface roughness as a result of agglomerates formed on the surface. Figure 2.8 shows the mapping of the Auger signals along with the SEM image of the same area. All the elements seem to be distributed almost uniformly, but dark spots are seen in each of the AES maps. Those dark spots correspond to particles (white spots in the SEM image), and the signal intensity of each element is smaller at the position of the particles than in the flat part. The AES spectra taken at position A (particle) and B (flat part) are shown in Figure 2.9. The ratios of the signal intensities are almost the same, and therefore we may conclude that a uniform random alloy Cu_xZn_yS was formed. In the following, AES data taken at the flat part are used in the composition calculation.

Table 2.1. Solution conditions, film compositions, and band gap energies for the Cu_xZn_yS films.

$ZnSO_4$ (mM)	$CuSO_4$ (mM)	Zn/Cu Ratio	Zn	:	Cu	:	S	Band gap (eV)
5.00	25.00	0.2	0.76	:	0.66	:	1	3.3
10.00	20.00	0.5	0.8	:	0.6	:	1	3.3
15.00	15.00	1	0.71	:	0.48	:	1	3.2
20.00	10.00	2	0.64	:	0.34	:	1	3.0
22.50	7.50	3	0.63	:	0.26	:	1	3.1
24.00	6.00	4	0.67	:	0.29	:	1	3.2
25.00	5.00	5	0.66	:	0.28	:	1	3.3
27.27	2.73	10	0.64	:	0.23	:	1	3.2
28.57	1.43	20	0.59	:	0.22	:	1	3.2
29.27	0.73	40	0.71	:	0.21	:	1	3.3

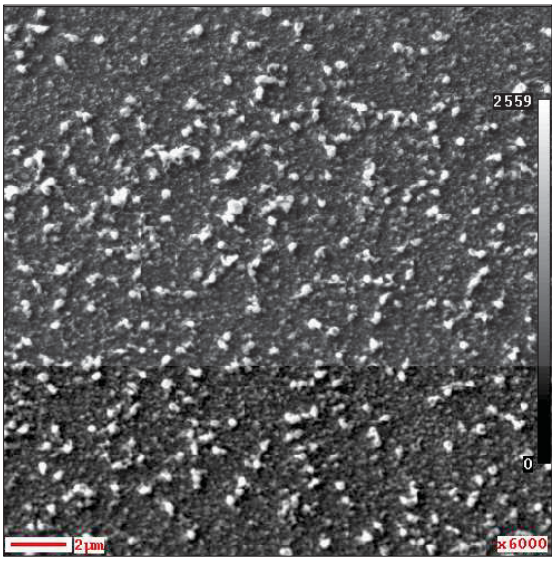

Fig. 2.7. SEM photograph of the surface of the Cu_xZn_yS film (Zn/Cu ratio in the solution = 4).

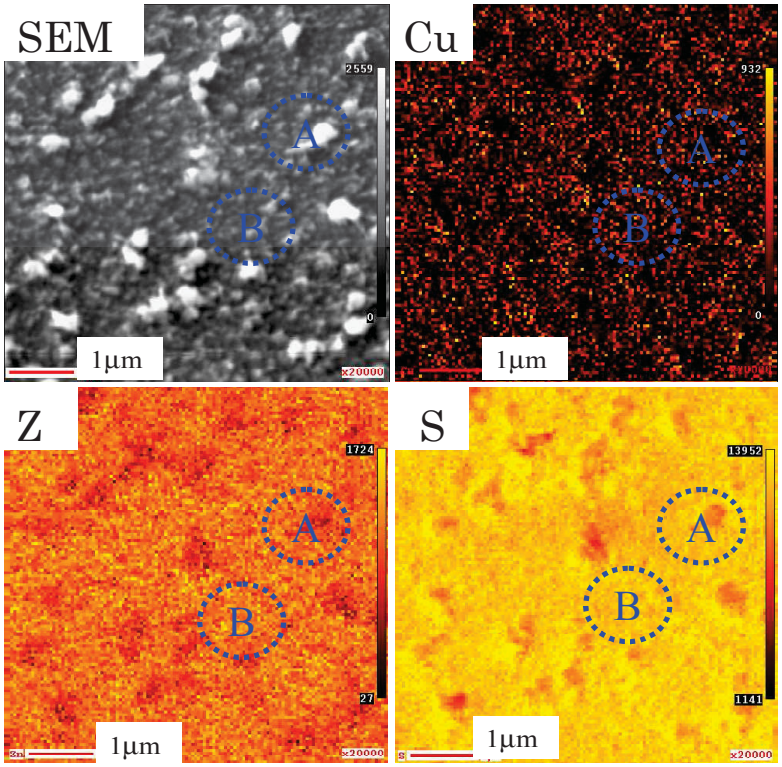

Fig. 2.8. SEM image and Auger signal maps for Cu, Sn, and S of the Cu_xZn_yS film (Zn/Cu = 4).

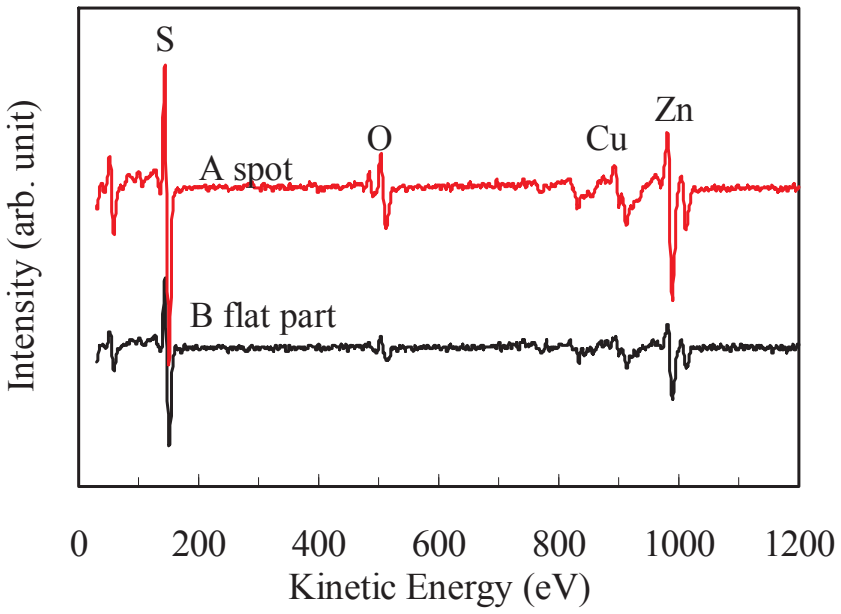

Fig. 2.9. AES spectra at position A (particle) and B (flat part) of the AES maps.

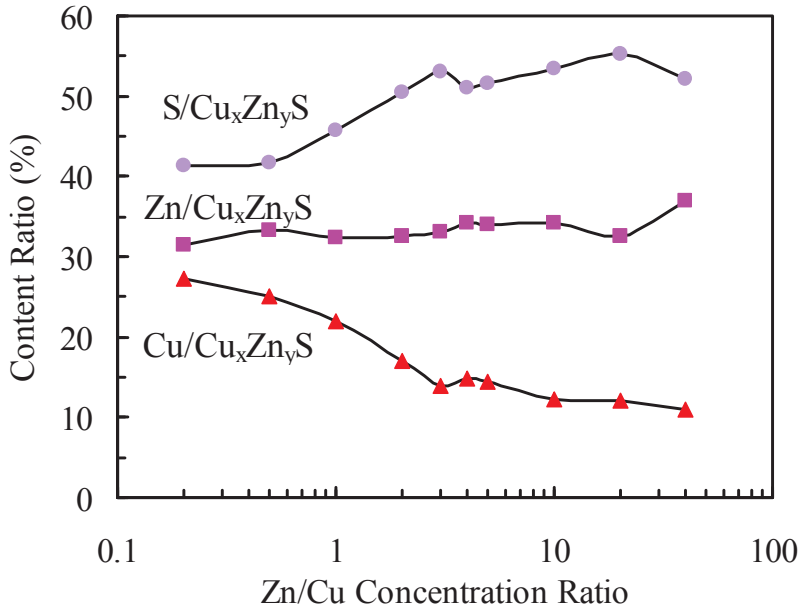

Fig. 2.10. Relation between the Zn/Cu concentration ratio of the solution and the Cu, Zn, S content ratios of the deposited films.

The concentration ratios for the three elements are shown in Figure 2.10 for the films deposited with different solution compositions. The Zn content depends only weakly on the Zn/Cu concentration ratio in the solution. The copper content decreases and the sulfur content increases with increasing Zn/Cu. As noted in Introduction, Cu_xZn_yS can be considered as a nonstoichiometric alloy, and in fact the S/metal ratio varied as shown in Figure 2.10. For relatively Zn-rich conditions, the S/metal ratio seems to approach unity ($S/Cu_xZn_yS \approx 0.5$). This would be because ZnS is a stoichiometric compound with S/ZnS=0.5.

Figure 2.11 shows Raman spectra of the films deposited with various concentration ratios. A peak near 470 cm^{-1} was detected for Zn/Cu = 3 and 4, but no peaks were observed for other concentrations ratios. As noted above, a peak was observed near 470 cm^{-1} for Cu_xS. In fact, this peak can be assigned to the S-S vibration since elemental sulfur also exhibits a peak there. The appearance of the peak near 470 cm^{-1} does not necessarily mean presence of a separate Cu_xS or elemental sulfur phase, because in Raman spectra, even isolated impurities

can exhibit a peak. Thus the Raman results may indicate that the number of S-S bonds is relatively large when Zn/Cu=3 or 4.

Figure 2.12 shows the XRD patterns of the Cu_xZn_yS films (Zn/Cu=2, 4, 40) grown on the ITO substrate and the bare ITO substrate. We mark the peak positions of In_2O_3 taken from the database (JCPDS Files No. 6-0416), and they closely match the peak positions observed for the bare ITO substrate. From comparison of the four spectra, it is seen that all the films exhibited no sharp peak, which confirms that the deposited film is amorphous. Almost the same spectra were observed for the other samples.

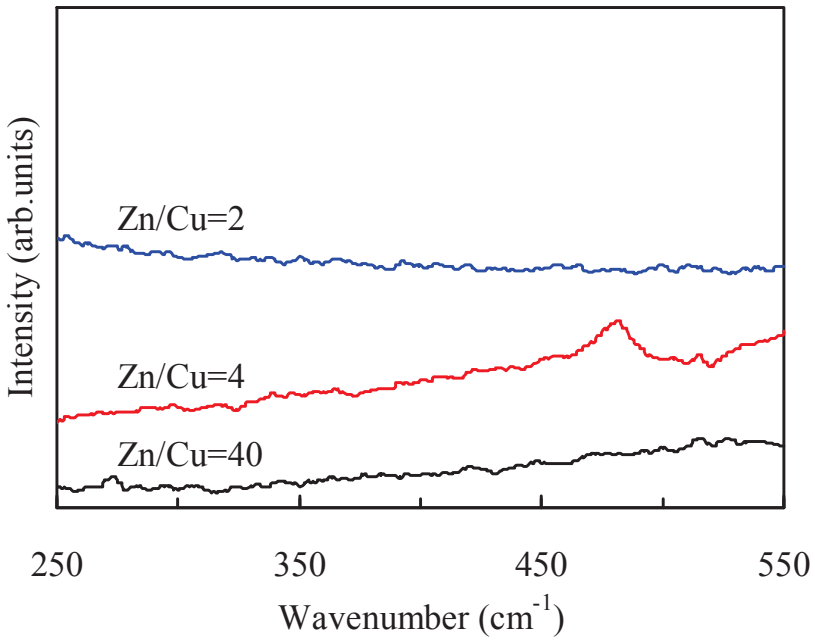

Fig. 2.11. Raman spectra of the Cu_xZn_yS thin films deposited with various concentration ratio (Zn/Cu=2, 4, 40).

Figure 2.13 shows the optical transmission spectra for the Cu_xZn_yS films deposited with three different concentration ratios of the solution (Zn/Cu=2, 4, 40). All the Cu_xZn_yS thin films showed an optical transmission of 60% ~80% in the visible region for a 0.1 μm-thick film. The gradual decrease in the UV region can be attributed to the amorphous nature of the Cu_xZn_yS film. The other Cu_xZn_yS films with different Zn/Cu ratios also show transmission spectra similar to those shown in Figure 2.13. Elemental Cu is metallic, and Cu_xS has an absorption edge in the visible region. Therefore, the high optical transmission of the Cu_xZn_yS films indicates that Cu in the films is not in the metallic Cu or Cu_xS phase but constitutes a ternary alloy with a wide band gap.

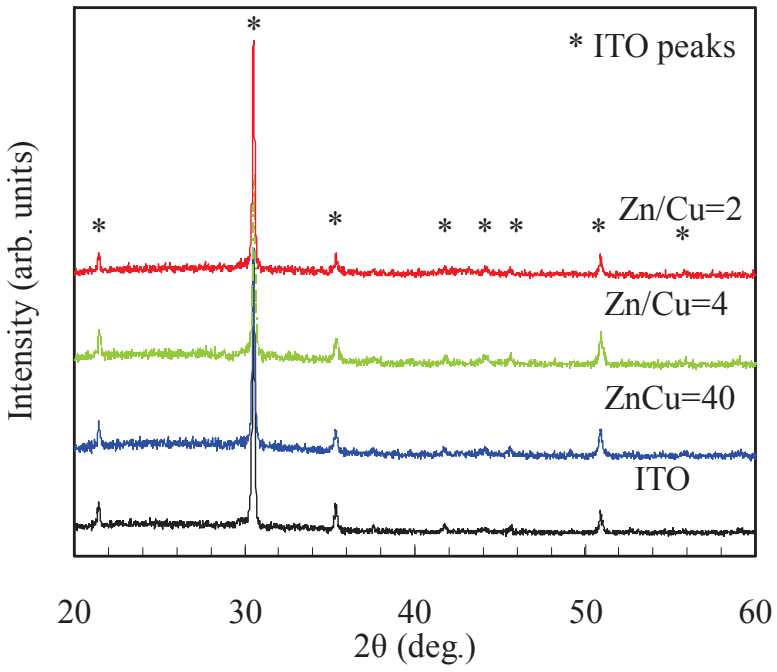

Fig. 2.12. XRD data of the Cu_xZn_yS thin films of various concentration ratios (Zn/Cu=2, 4, 40).

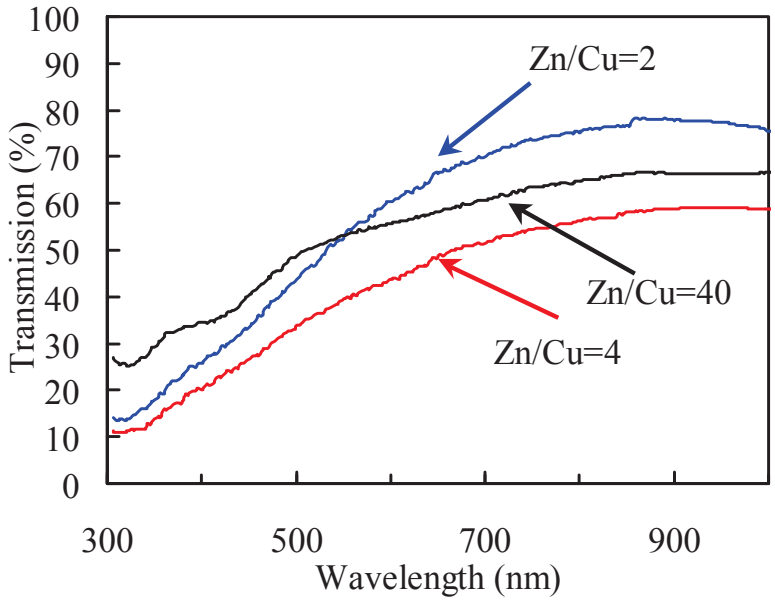

Fig. 2.13. Optical transmission spectra of the Cu_xZn_yS thin films deposited with various concentration ratios (Zn/Cu=2, 4, 40).

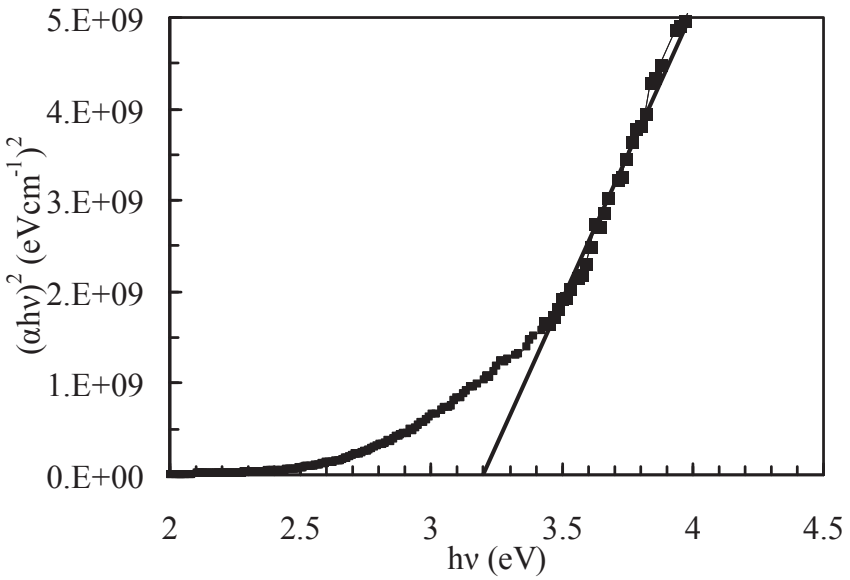

Fig. 2.14. Estimation of the band gap for the deposited Cu_xZn_yS (Zn/Cu=4) thin film.

The direct energy band gap of the deposited film was estimated from the optical transmission measurement. The plot of $(\alpha h\nu)^2$ vs. $h\nu$ shown in Figure 2.14 reveals that the direct energy band gap of the film deposited with Zn/Cu=4 approximately equals 3.2eV [24]. We attempted to calculate the indirect bandgap, but the plot of $(\alpha h\nu)^{1/2}$ vs. hν does not give a reasonable value of E_g. For the other concentrations ratios, the band gap was in a range of 3.0-3.3eV and only weakly dependent on the Zn/Cu concentration ratio. Those band gap energies are considerably larger than that reported for the $Cu_{0.6}Zn_{0.4}S$ film deposited by the SILAR method (2.14 eV) [22].

Figure 2.15 shows the PEC measurement result for the three samples. Since the photocurrent is negative, the minority carriers generated here are electrons. Thus, the deposited films are all p-type and photosensitive. The results for the Cu_xZn_yS films of the other compositions also show that the films are photoconductive and p-type, and the intensity of the photocurrent tends to be larger for larger Zn/Cu ratios. It is known that a compound or an alloy semiconductor containing Cu tends to have p-type conductivity because the valence

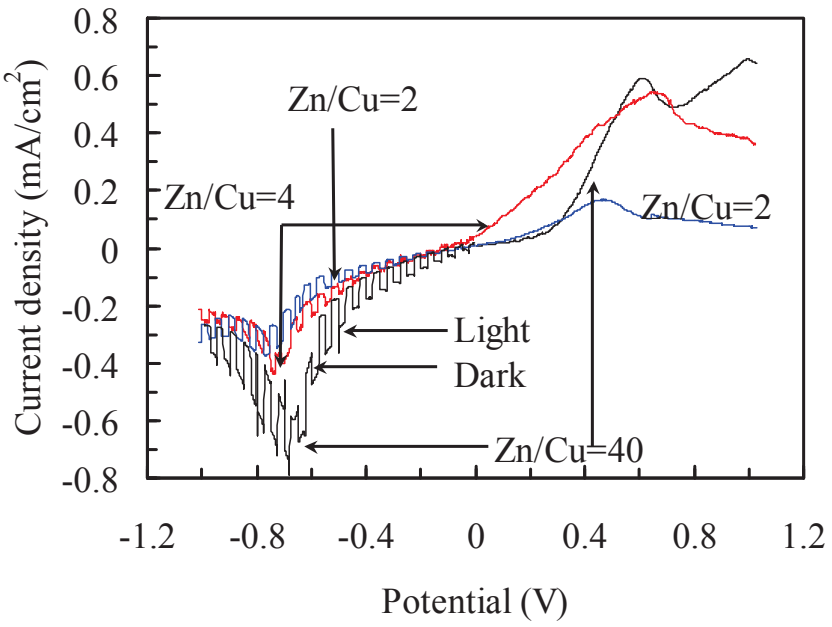

Fig. 2.15. Results of the PEC measurement of the Cu_xZn_yS thin films deposited with various concentration ratios (Zn/Cu=2, 4, 40).

band maximum (VBM) is shifted upward by the filled 3d states of Cu [30]. It seems that though the Cu content in the film is smaller than the Zn content, the Cu content is still sufficient to shift the VBM position.

Figure 2.16 shows the current-voltage characteristics of the heterojunction. In the Figure 2.16, the positive voltage means that the Cu_xZn_yS side of the sample was positively biased with respect to the ZnO side. Thus this result shows that n-ZnO/p-Cu_xZn_yS rectifying junction was formed. This proves that the ECD Cu_xZn_yS films can be applied for various optoelectronic devices such as UV sensors and blue-UV LED. Although the rectifying properties are constantly observed, the amount of leakage current varied considerably from sample to sample. Thus, uniformity and reproducibility of the film quality has to be improved.

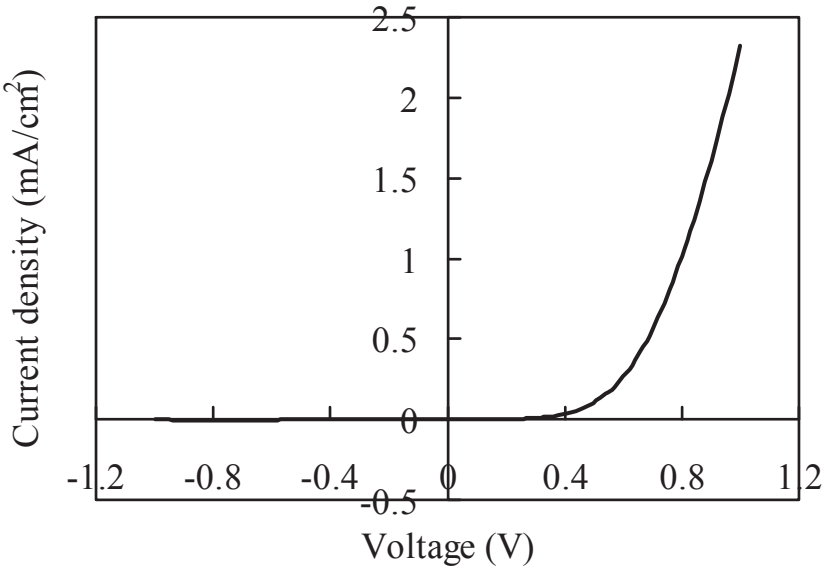

Fig. 2.16. Current–voltage characteristics of the n-ZnO/p-Cu_xZn_yS (Zn/Cu=4) heterojunction.

2.3.2 PCD of Cu_xZn_yS

The AES measurement result was shown in Figure 2.17. As can be seen from the Figure 2.17, Cu_xZn_yS thin films contain a small amount of O. Since the surface of the thin film was sputtered before the AES measurement, it is more likely that oxygen exists in the form of Cu_xZn_yO, rather than as a surface contamination. Since the pH of the solution was 3.0, the amount of OH^-, which is a possible oxygen source, was minimal, and thus it can be considered that O was supplied by the dissolved oxygen in the solution. And the composition obtained from the signal intensity is $Cu_{0.10}Zn_{0.79}S_{0.73}O_{0.27}$.

Figure 2.18 shows the mapping of the Auger signals along with the SEM image of the same area. All the elements seem to be distributed almost uniformly. This shows that the deposit is a uniform alloy, not a composite of binary compounds such as Cu_xS and ZnS.

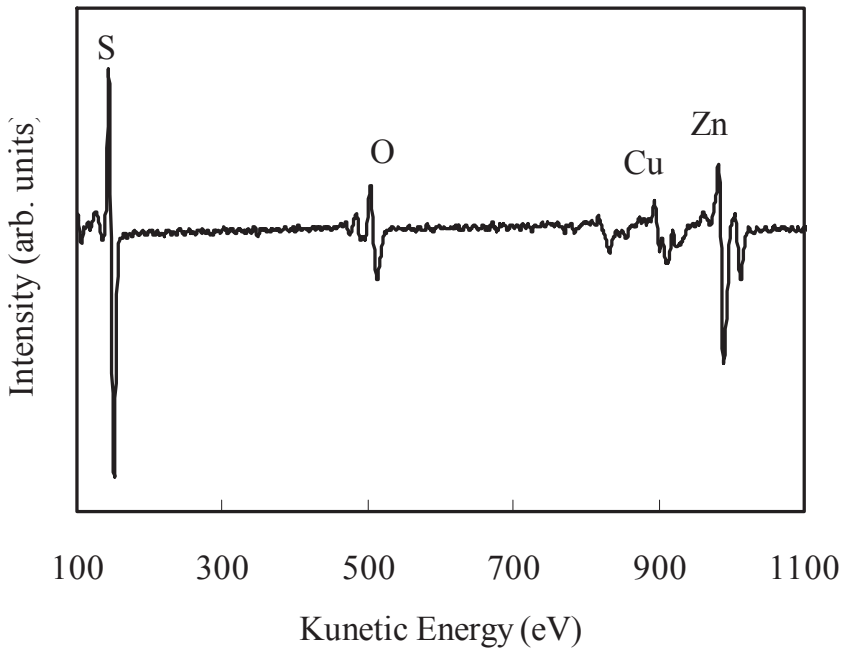

Fig. 2.17. AES spectra for the Cu_xZn_yS thin film.

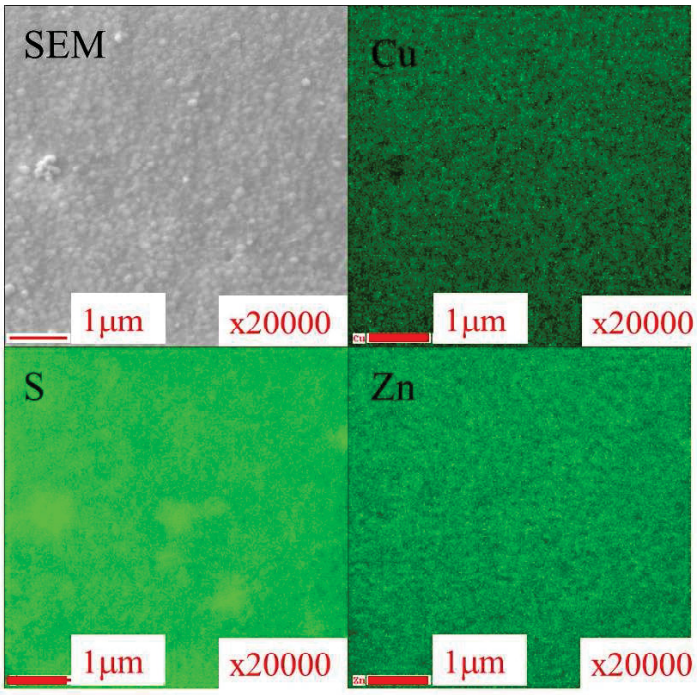

Fig. 2.18. SEM image and AES signal maps for Cu, Zn and S for the Cu_xZn_yS film.

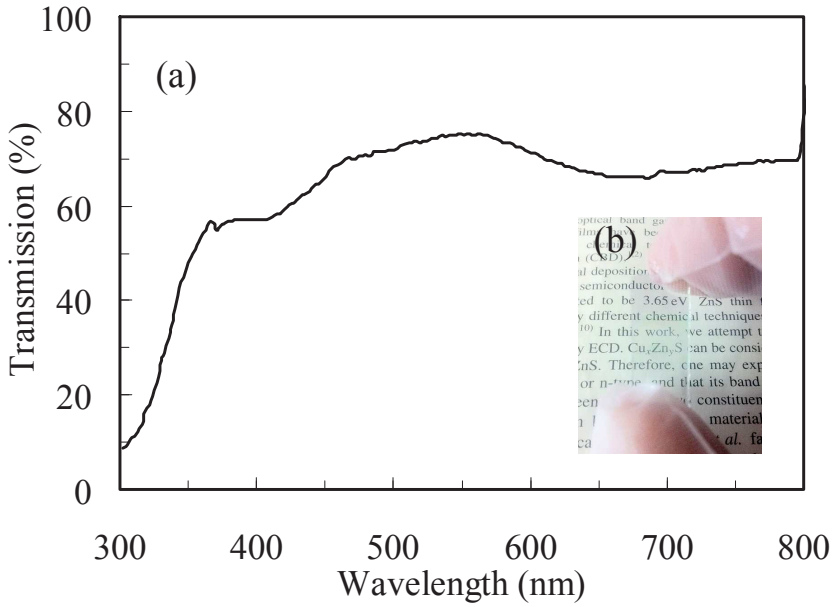

Fig. 2. 19. (a): Optical transmission spectra for the Cu_xZn_yS film,

(b): Photo of the Cu_xZn_yS film.

Figure 2.19 (a) shows the result of optical transmission measurement of the Cu_xZn_yS film. The film thickness was about 0.2 μm. Transmission in the visible region of 480 nm to 750 nm is high, 70% ~ 80%, and the bandgap is 3.6 eV. Figure 2. 19 (b) shows the photo of the Cu_xZn_yS film. We confirmed that the transparent thin film was obtained.

The XRD measurements were carried out, but from comparison with the spectrum for the ITO substrate, all the observed peaks were of the ITO substrate, i.e., there is no peak of Cu_xZn_yS. Thus the deposited films are considered to be amorphous or nano-crystalline.

Figure 2.20 shows the PEC measurement results. The negative current was enhanced by the light under the negative bias, while the change in the current was not significant under the positive bias. Thus the photocurrent is negative, and therefore the minority carriers are electron, i.e., the film is p-type.

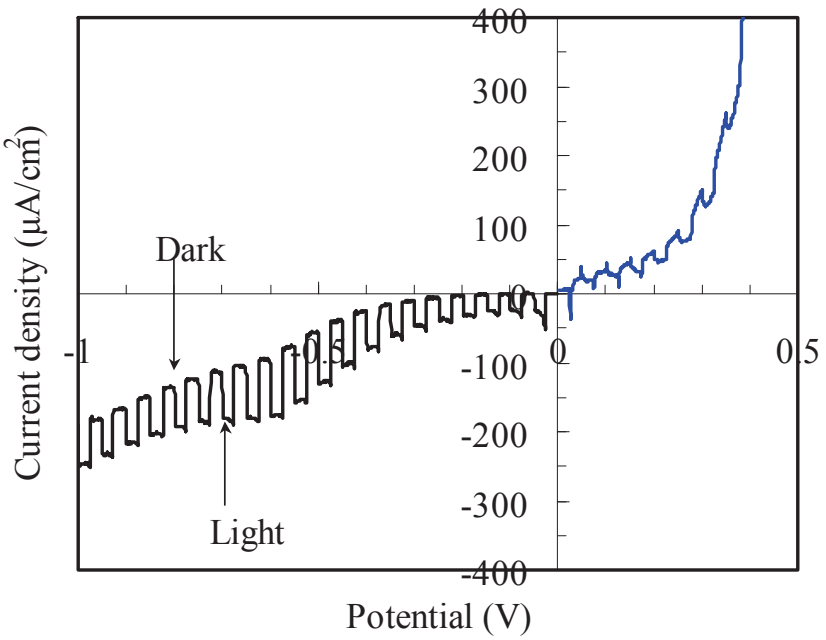

Fig. 2. 20. PEC measurement results for the Cu_xZn_yS film.

2.3.3 Annealing study of ECD-Cu_xZn_yS

Figure 2.21 shows the atomic composition ratios of the as-deposited and annealed films. The film was deposited from the solution with a concentration ratio Zn/Cu=4. The results revealed that the Zn and Cu contents did not vary significantly. However, O and S contents depend on the annealing temperature. The oxygen content increased as the annealing temperature increased up to 200°C. Although the annealing was carried out under the flow of nitrogen gas (99.999% pure nitrogen), a trifle of oxygen would remain in the annealing furnace. Therefore, during the annealing, extra oxygen could be adsorbed at the surface and diffused to the bulk of the film to replace the sulfur.

Figure 2.22 shows the surface morphology of the films annealed at the different temperatures. The substrate surface is completely covered with a uniform film without crakes or voids, and the grains size increased with increasing annealing temperature.

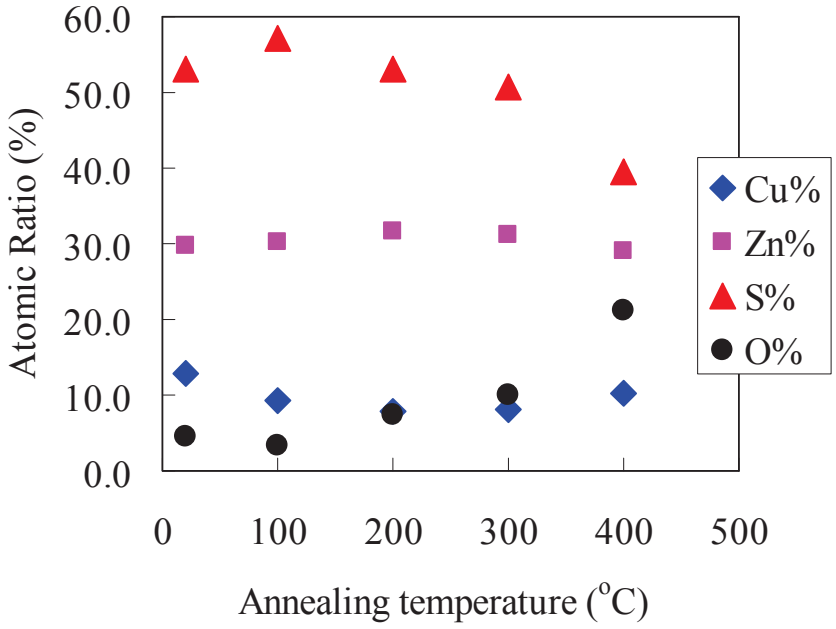

Fig. 2. 21. AES spectra for the as-deposited and annealed films

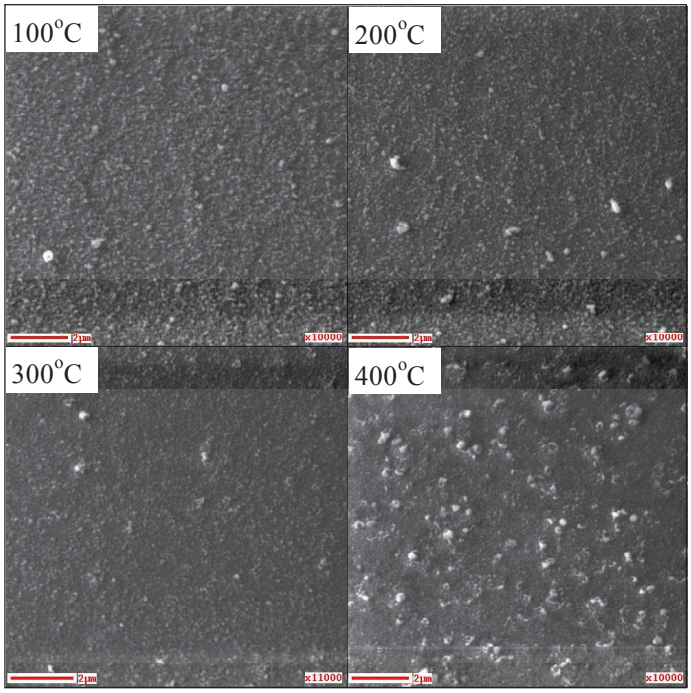

Fig. 2. 22. SEM micrograph of the surface of the annealed films.

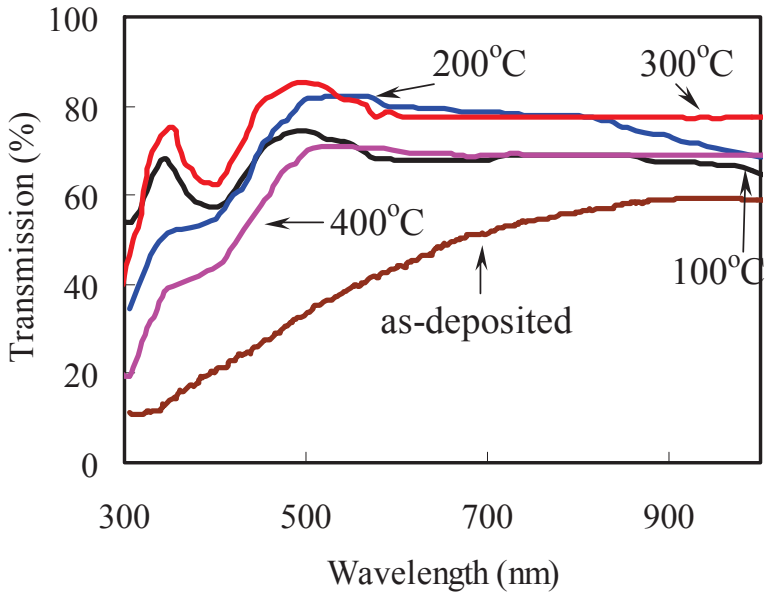

Fig. 2. 23. Optical transmission spectra for the as-deposited and annealed films.

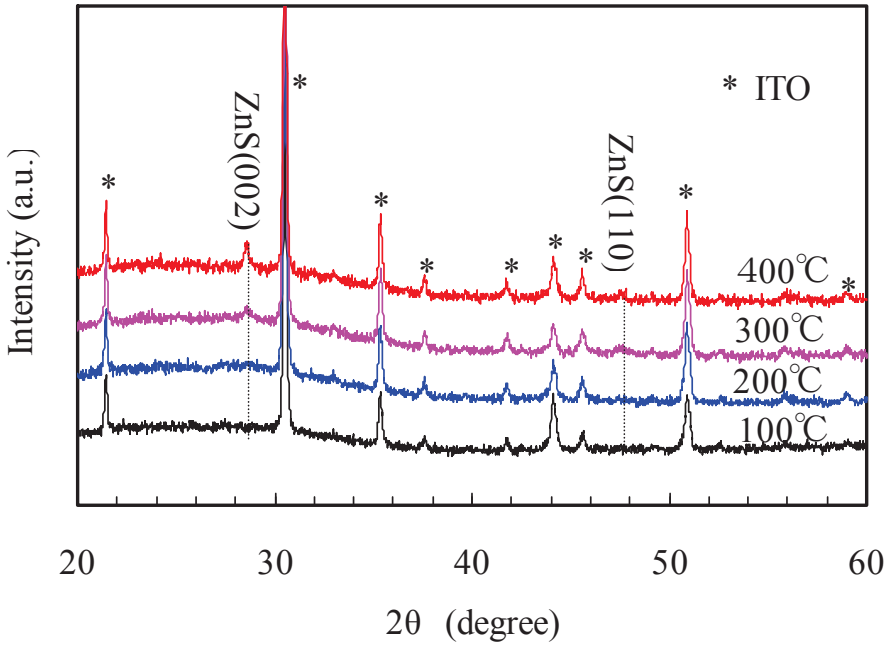

Fig. 2. 24. XRD patterns of the Cu_xZn_yS thin films at the various annealing temperatures.

Figure 2.23 shows the optical transmission spectra of as-deposited and annealed films at the different temperature. The transmission of the annealed films for a 0.05 μm-thick film is higher than that of the as-deposited films. Probably, elemental sulfur at the surface was evaporated. The bandgap energy of the as-deposited and annealed films was estimated from the optical transmission spectrum. The bandgap of the as-deposited film was about 3.3 eV and slightly increased (about 3.5 eV) due to the annealing at 100 ~ 400ºC.

Figure 2.24 shows the XRD patterns measured for the annealed film grown on the ITO substrate. In addition to the ITO peaks were confirmed, shifting ZnS peaks were also observed, and the ZnS peak intensity increased with increasing temperature. On the other hand, there are no peaks due to elemental Cu and Zn or Cu_xS.

Figure 2.25 shows the results of the PEC measurement for the annealed films. The films thickness is about 0.05 μm after the annealing at 100 ~400°C. The negative photocurrent

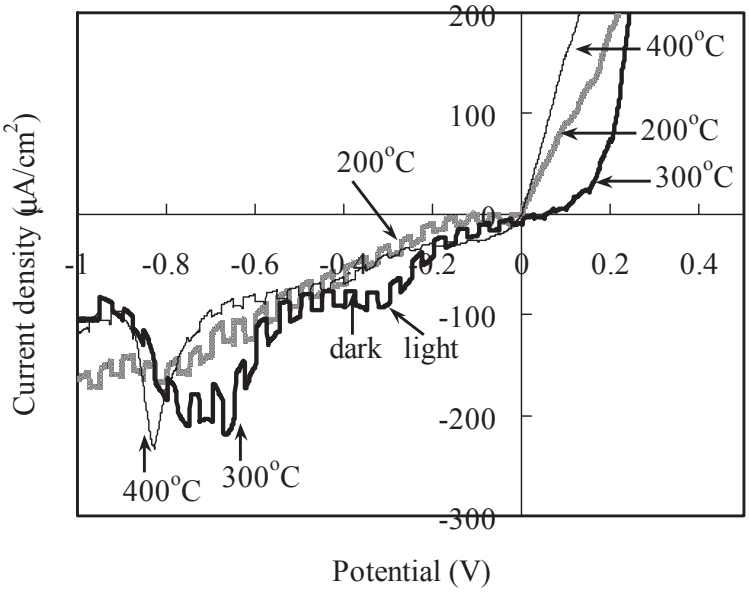

Fig.2.25. PEC measurement results for the films annealed at 200 ~ 400°C

under the negative bias was observed, thus the annealed films are all p-type. After the 200 and 300 °C annealing, the photosensitivity did not vary significantly compared with the as-deposited film. On the other hand, due to the effect of the increased oxygen content, the photosensitivity became weak after the 400°C annealing.

2.4 Conclusions

Cu_xZn_yS thin films have been deposited from solutions containing $Na_2S_2O_3$, $CuSO_4$, $ZnSO_4$, and lactic acid by ECD and PCD. The Cu_xZn_yS thin films have a wide band gap of 3.0-3.6 eV and exhibit p-type conduction and photosensitivity. The thickness is about 0.1 μm. The ZnO/ Cu_xZn_yS heterojunction cells showed rectification properties. Thus, Cu_xZn_yS can be regarded as a new wide-gap p-type material and can be used for various optoelectronic applications. After annealing at 100 ~ 400º, the Zn and Cu contents did not vary significantly. However, O and S contents depend on the annealing temperature. The optical transmission increased with increasing annealing temperature.

References

[1] P. Nair and M. Nair, J. Phys. D: Appl. Phys. 24 (1991) 83.

[2] T. Yamamoto, E. Kubota, A. Taniguchi, S. Dev, K. Tanaka, and K. Osakada, Chem. Mater. 4 (1992) 570.

[3] I. Grozdanov, C. K. Barlingay, S. K. Dey, M. Ristov, M. Najdoski, Thin Solid Films 250 (1994) 67.

[4] A.C. Rastogi and S. Salkalachen, Thin Solid Films 97 (1982) 191.

[5] H. Pathan, J. Desai, and C. D. Lokhande, Appl. Surf. Sci. 202 (2002) 47.

[6] M. Nair and P. Nair, Semicond. Sci. Technol. 4 (1989) 191.

[7] K. Gadave and C. Lokhande, Thin Solid Films 229 (1993) 1.

[8] I. Grozdanov, C. K. Barlingay, S.K. Dey, M. Ristov, and M. Najdoski, Thin Solid Films 250 (1994) 67.

[9] J. Podder, R. Kobayashi, and M. Ichimura, Thin Solid Films 472 (2005) 71.

[10] C. Naşcu, I. Pop, V. Ionescu, E. Indrea, I. Bratu, Mater. Lett. 32 (1997) 73.

[11] J. Vedel, P. Cowache and D. Lincot, Solar Cells 11 (1984) 241.

[12] R. Engelken and H. McCloud, J. Electrochem. Soc. 132 (1985) 567.

[13] T. Yukawa, K. Kuwabara, and K. Koumoto, Thin Solid Films 280 (1996) 160.

[14] K. Anuar, Z. Zainal, M. Hussein, N. Saravanan, and I. Haslina, Sol. Energy Mater. Sol. Cells 73(2002) 351.

[15] T. Nakata, M. Hongo and E. Hayashi, Thin Solid Films 242 (2003) 431.

[16] A. Ennaoui, W. Eisele, M. Lus-Steiner, T.P. Niesen, and F. Karg, Thin Solid Films 431 (2003) 335.

[17] J. Vidal, O. Melo, O. Vigil, N. Lopez, G. Contreras-Puente, and O. Zelaya-Angel, Thin Solid Films 419 (2002) 118.

[18] J. M. Dona and J. Herrero, Thin Solid Films 268 (1995) 5.

[19] T. Taguchi and T. Yokogawa, J. Phys. D 17 (1984) 1067.

[20] B. Sanders and A. Kital, J. Cryst. Growth 100 (1990) 405.

[21] N. Fathy, R. Kobayashi, and M. Ichimura, Mater. Sci. Eng. B 107 (2004) 271.

[22] A. Yildirim, A. Aytunc, and A. Aykut, Physica E 41(2009) 1365.

[23] N. Kitagawa1, S. Ito, D.C. Nguyen and H. Nishino, Natural Resources 4 (2013) 142.

[24] K. Yang and M. Ichimura, Jpn. J. Appl. Phys. 50 (2011) 040202.

[25] F. Kang, J. Ao, G. Sun, Q. He, and Y. Sun, Mater. Chem. Phys. 115 (2009) 516.

[26] F. Kang and M. Ichimura, Thin Solid Films 519 (2010) 725.

[27] E. Fatos, R. Duo, P. Herrasti, F. Arjona, and E. Garcia-Camarero, J. Electrochem. Soc. 131 (1984) 2243.

[28] G. P. Power, D. R. Peggs and A. I. Parker, Electrochem. Acta 26 (1981) 681.

[29] A. Zunger, Appl. Phys. Lett. 83 (2003) 1.

[30] M. Izaki and T. Omi, J. Electrochem. Soc. 143 (1996) L53.

Chapter 3

Fabrication of Cu-Zn-Sn-S-O Thin Films by the Electrochemical Deposition Method and Application to Heterojunction Cells

3.1 Introduction

Cu_2ZnSnS_4 (CZTS) is suitable for thin film solar cells, owing to the band gap energy of 1.4-1.5 eV and large absorption coefficient over 10^4 cm^{-1}. Moreover, efficiency was further improved by adding Se into CZTS thin film. Several papers were reported on solar cells based on $Cu_2ZnSnS_{4-x}Se_x$ (CZTSSe), and Barkhouse et al. have fabricated 10.1% efficient CZTSSe cells by hydrazine-based solution processing [1]. Oxygen is another group VI element and can replace S in CZTS without disturbing valence. Therefore, $Cu_2ZnSnS_{4-x}O_x$ (CZTSO) can also be suitable for thin film solar cells. However, to our knowledge, there is only one paper on fabrication of CZTSO, which reports deposition of CZTSO by an open atmosphere type chemical vapor deposition using oxide precursors [2]. In this work, we deposit CZTSO thin films by the electrochemical deposition (ECD), which is a low-cost technique that enables the production of thin films in a large area in a short time.

ECD has been used to deposit metal precursors, which is subsequently sulfurized to form CZTS [3-5]. Recently, direct synthesis of CZTS by ECD has been reported [6-8]. However, in those previous papers, oxygen amount in the films was not mentioned at all, although introduction of some amount of oxygen is usually not avoidable in ECD from an aqueous solution. Thus, effects of oxygen on film properties have never been studied, and it has not been discussed either how the oxygen amount in a film can be controlled in ECD. Moreover, fabrication of heterostructure cells based on non-annealed ECD-CZTS has not been reported. In this work, we fabricate heterostructures based on as-deposited CZTSO films. So far, as a buffer layer, CdS was usually used for CZTS and CIGS based solar cells [1, 9], but Cd is

Table 3.1. Deposition potential, composition, thickness and bandgap of the CZTSO thin films.

Sample	Potential (V)	Cu (at%)	Zn (at%)	Sn (at%)	S (at%)	O (at%)	Thickness (μm)	Bandgap (eV)
A	V=-0.8	28.2	9.4	12.9	19.8	29.7	~0.5	2.1
B	V=-0.8~-0.5	28.4	11.3	8.8	30.9	20.6	~0.3	1.6
C	V=-0.9~-0.5	27.6	8.4	14.8	40.9	8.4	~0.3	1.6
D	V=-1.0~-0.5	22.6	16.3	13.0	28.8	19.2	~0.3	1.5
E	V=-1.1~-0.5	23.6	17.4	13.2	26.0	19.6	~0.3	1.6

toxic and relatively rare. Recently, a Cd-free CZTS/ZnO heterojunction solar cell has been reported, and the conversion efficiency of 4.29% has been obtained [10]. Therefore, we selected ZnO as the partner of the pn heterojunction based on CZTSO.

In order to investigate the effect of oxygen amount on the CZSTO thin films, we attempted to sulfurize the CZTSO thin films. To do that, the low-cost sulfurization technique was developed.

3.2. Experimental

A three-electrode cell was used for ECD with a saturated calomel electrode (SCE) as the reference electrode. Hokutodenko function generator HB-104 and potentiostat/ galvanostat HA-301 were used as the voltage source. Indium-tin-oxide (ITO)-coated glass was used as the working electrode (substrate) and a platinum sheet was used as the counter electrode. Both the ITO substrate and the platinum sheet were washed ultrasonically in alky benzene and dried in nitrogen before the experiment. The deposition area was about 1x1 cm^2. The CZTSO thin films were prepared from an aqueous solution containing 5 mM $CuSO_4$, 5 mM $ZnSO_4$, 5 mM $SnSO_4$ and 25 mM $Na_2S_2O_3$, and 2 ml sodium lactate (59%) was added to 50 ml of the aqueous solution as a pH buffer [11, 12]. pH of the solution was 4.8. We succeeded in depositing Cu_xZn_yS using a similar solution containing lactate ions [13]. The electrolyte

temperature was kept at room temperature in a water bath throughout the deposition. The deposition potential was determined on the basis of the cyclic voltammetry (CV). The cathodic scan was from 0 to -1.5 V and the anodic scan was from -1.5V to +0.5 V with a scan rate of 20 mV/s. Both DC and two-step pulse biases were employed for the deposition. The DC potential was determined to be -0.80 V on the basis of the cyclic voltammogram. The pulsed potentials employed for the deposition are listed in Table 3.1. The typical pulsed voltage and current profiles during deposition are shown in Figure 3.1. Total deposition time is 20 min. After the experiment, the deposited films were washed in pure water and naturally dried in air.

The as-deposited films with the optimum deposition condition were sulfurized by sulfur at a relatively low temperature. Figures 3.2 a) and b) show the schematic diagram of the sulfurization equipment. The as-deposited films were put into a ceramic crucible with sulfur (99.99%). Sulfur was evaporated on the as-deposited film. The evaporation time and temperature were 1 h and 150°C, respectively. The S/CZTSO thin film was placed in an electric furnace tube filled with N_2 gas. The tube was heated at a rate of 10°C/min to 300°C, maintained at that temperature for 1 hour and then, cooled naturally.

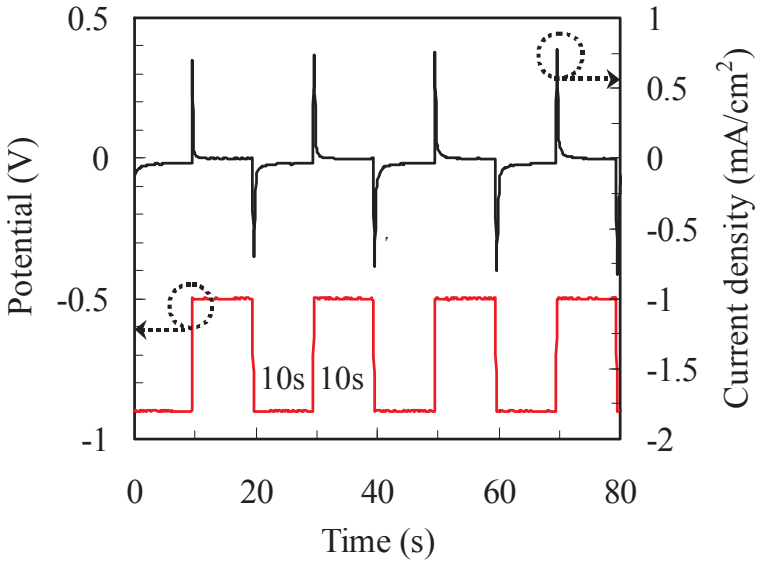

Fig. 3.1. Two-step pulsed voltage and current profile during deposition of sample C.

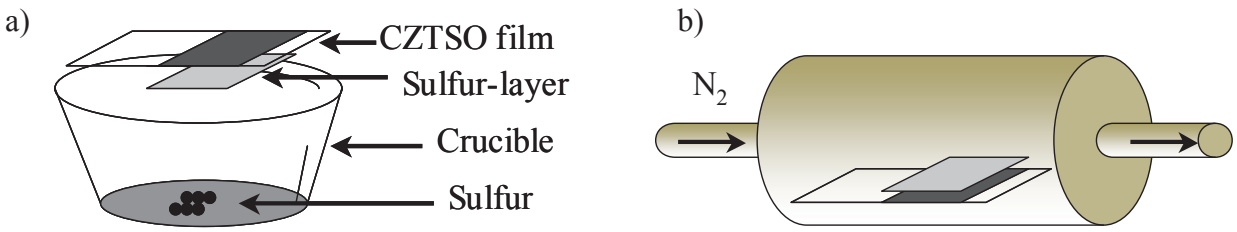

Fig. 3.2. a) Schematic diagram of the sulfurization container, and b) Schematic diagram of the annealing furnace tube.

The compositional analyses were carried out by Auger electron spectroscopy (AES) using a JEOL JAMP 9500 Auger microprobe at a probe voltage of 10 kV and a current of 2 x 10^{-8} A. Argon ion etching with an acceleration voltage of 3 kV and a current of 8 mA was used to sputter the film surface. The surface morphology observation was also performed using scanning electron microscope (SEM) of JEOL JAMP 9500. The films thickness was measured by an Accretech Surfcom-1400D profile meter. The optical transmission measurement was performed using a JASCO U-570 spectrometer with the substrate as the reference. X-ray diffraction (XRD) was measured using a Rigaku Smartlab diffractometer with a Cu Kα radiation source.

To measure conduction type and photosensitivity, photoelectrochemical (PEC) measurements were carried out in an aqueous electrolyte containing 100 mM $Na_2S_2O_3$ using the same three-electrode cell as used for the deposition with the light incident from a xenon lamp toward the back side of the sample. The incident light was turned off and on mechanically every 5 s under the application of a ramp voltage.

ZnO was deposited by ECD using an aqueous solution containing 0.1 M $Zn(NO_3)_2$ [14]. The deposition temperature was 60ºC. The deposition bias was a two-step pulse with V_1 = -1.3V and V_2 = -0.6 V, and the duration of each pulse was 10s. The deposition time was 2 min, and the film thickness was about 0.5 μm. Aluminum was evaporated as electrodes on the Al/ CZTSO/ ZnO/ ITO glass substrate structure.

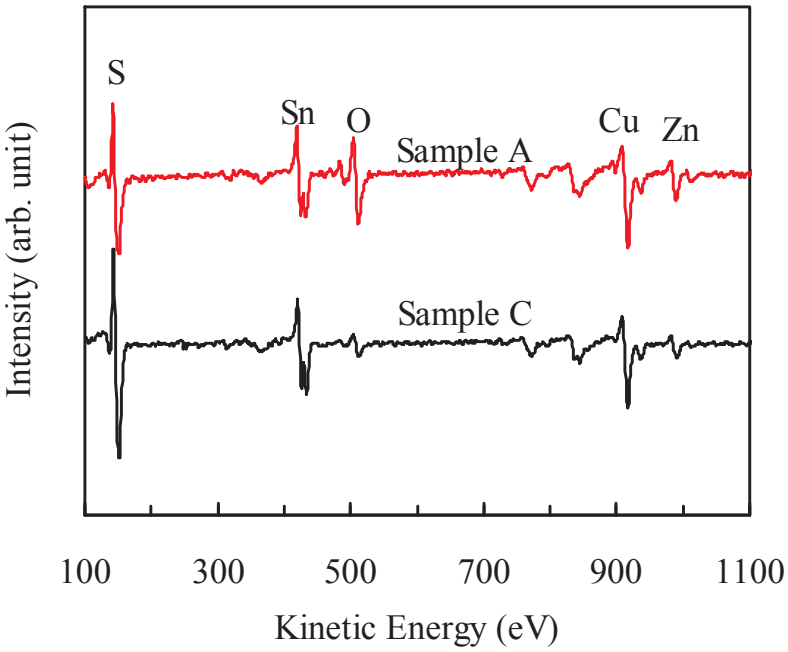

Fig. 3.3. AES spectra for samples A and C.

3.3. Results and Discussion

Figure 3.3 shows the AES spectra of samples A and C. The composition calculated from the AES results are listed in Table 3.1 and also plotted in Figure 3.4. The significant amount oxygen is included in the films. Introduction of oxygen is usually expected in ECD from aqueous solutions, and ECD of various oxides (ZnO [14, 15], SnO_2 [16, 17], Cu_2O [18, 19], and sulfide-oxides (SnS_xO_y [20], ZnS_xO_y [21]) has also been reported. The source of oxygen in those oxide depositions is either OH- ions or dissolved oxygen in the solution. In our case, since the solution is acidic (pH=4.8), the dominant source of oxygen would be dissolved oxygen. The O/S ratio in the film is larger than unity for sample A, but it is smaller for the samples deposited by the pulsed potentials. Thus the oxygen amount can be controlled by the deposition potential form. The previous works suggest that a slightly Zn-rich and Cu-poor composition gives good optoelectronic properties [22-24]. In case of the pulsed potential deposition, Cu amount was reduced with increasing negative potential, and samples D and E have Cu-poor composition (Cu/(Zn+Sn)<1). This can be explained as follows. The ionization

tendency is smaller (the equilibrium potential is more positive) for Cu than for Zn and Sn. Thus deposition of the Cu-based compounds will start at more positive potential than the Zn and Sn-based compounds. Then the composition will be more Cu-rich at relatively positive deposition potentials. With increasing negative deposition potential, deposition rates of the Zn and Sn-compounds will be enhanced while deposition rate of the Cu-compounds is limited by supply of ions in the solution. Therefore, the composition is more Zn and Sn-rich at a larger negative potential.

Figures 3.5 a) and b) show the SEM images of samples A and D. For sample A, which was deposited by DC ECD, deposits with irregular shapes are seen on a continuous but porous film, whereas sample D seems to be composed of densely-packed grains. The other samples deposited by pulsed ECD have surface morphology similar to sample D (Figure (b)). Thus the films deposited by pulsed ECD are more dense than that deposited by DC ECD.

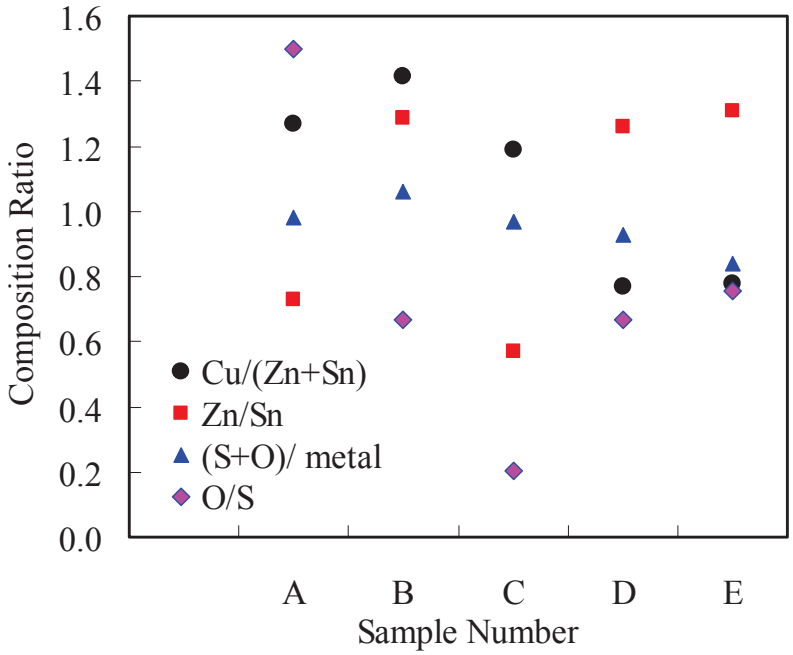

Fig. 3.4. Composition ratios of the samples (A, B, C, D, E).

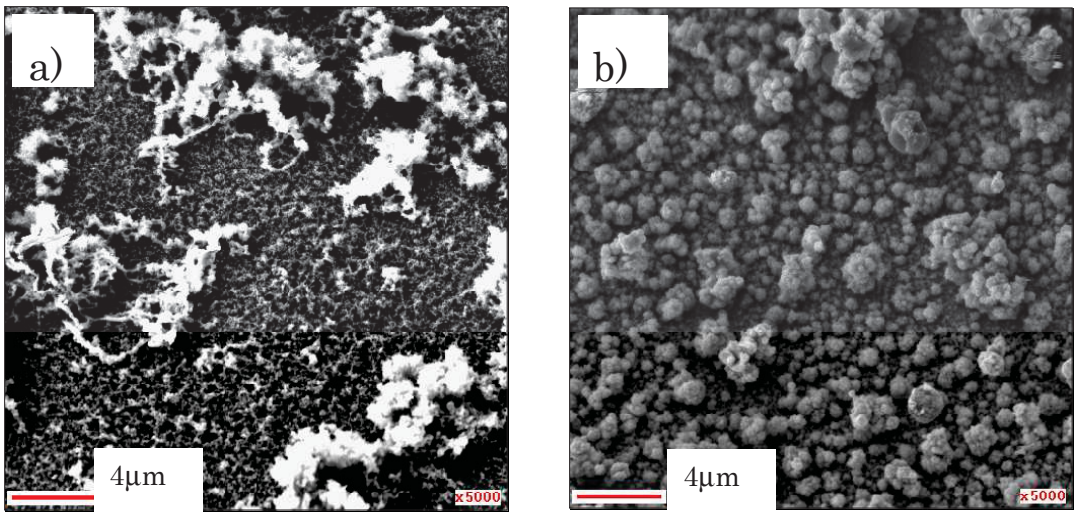

Fig. 3.5. SEM images of the surface of CZTSO (samples A and D)

Figure 3.6 shows the optical transmission spectrum of samples A, B, C, D, and E. The films deposited by the pulsed potentials have an absorption edge at a longer wavelength than that deposited by DC ECD. Figure 3.7 shows plots of $(\alpha h\nu)^2$ vs $h\nu$, where α is the absorption coefficient and $h\nu$ the photon energy. In the calculation of absorption coefficient from the transmission data, a constant reflectance value (10%) was assumed, and the obtained bandgap values are listed in Table 3.1. The band gaps of samples B-E are about 1.5-1.6 eV, close to the literature value of CZTS, while sample A has a band gap larger than 2 eV. We attempted to calculate the indirect bandgap, but the plot of $(\alpha h\nu)^{1/2}$ vs. $h\nu$ does not give a reasonable value of E_g. Since sample A is more oxygen-rich than the other samples, this indicates that the bandgap of CZTSO tends to increase with increasing oxygen content.

Figure 3.8 shows the PEC measurement results for the CZTSO films. The step-form variation in the current is due to the turning on/off of the illumination. By the illumination of the film, carriers are excited and the excited minority carriers diffuse to the surface to participate in the electrochemical reaction at the film-electrolyte interface. Since the photocurrent is negative, the minority carriers generated here are electrons. Thus, we confirmed that the CZTSO films are p-type. The photo current is largest for sample D. This will be partly due to the fact that sample D has the smallest band gap and thus can absorb

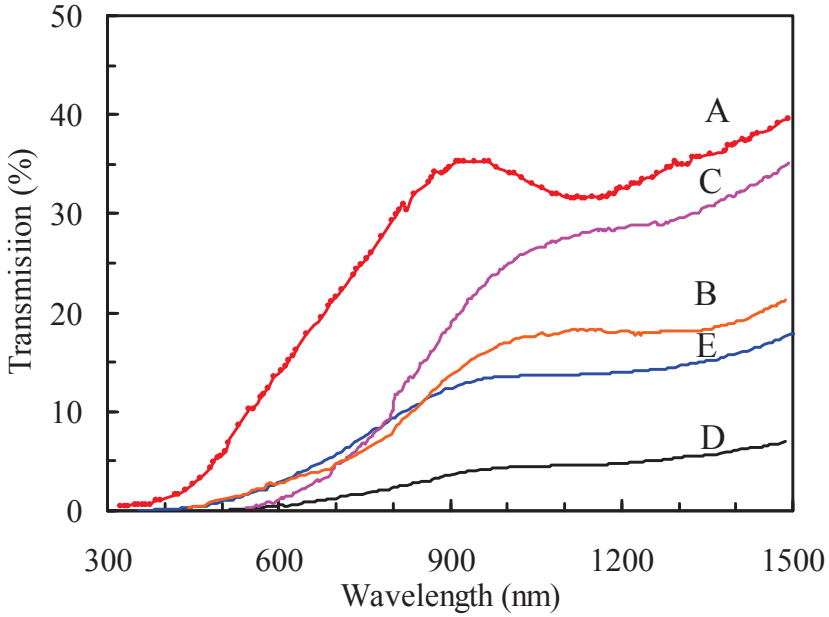

Fig. 3.6. Optical transmission spectra of the CZTSO samples (A, B, C, D, E).

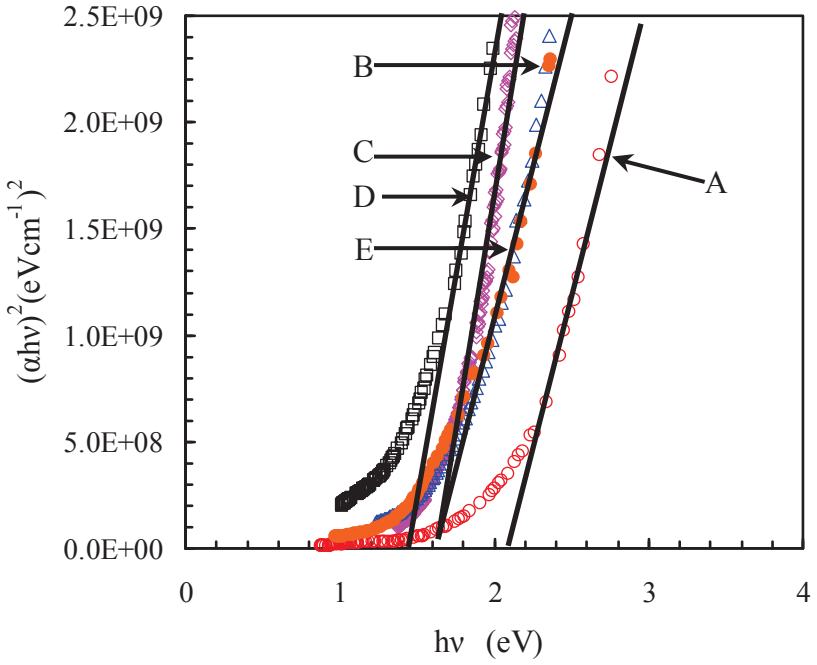

Fig. 3.7. Estimation of the band gap of the CZTSO samples (A, B, C, D, E).

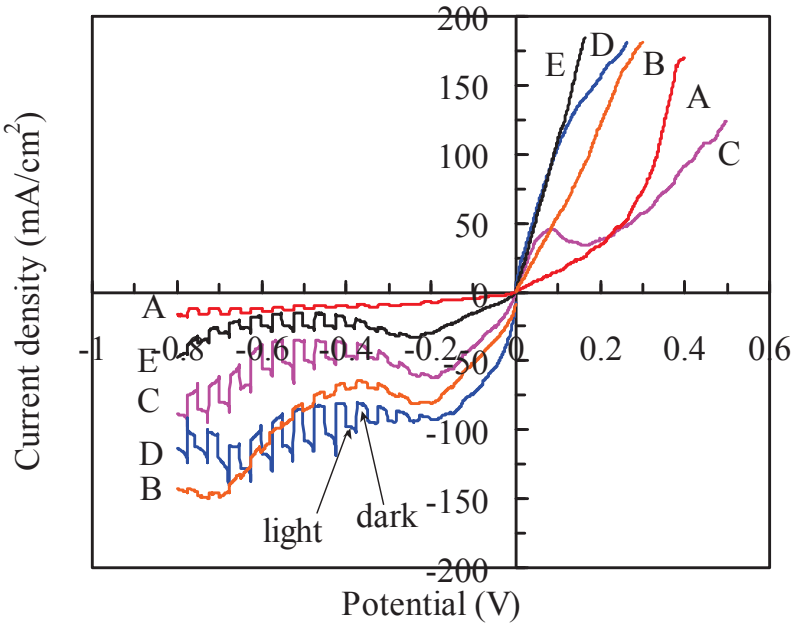

Fig. 3.8. PEC measurement results of the CZTSO samples (A, B, C, D, E).

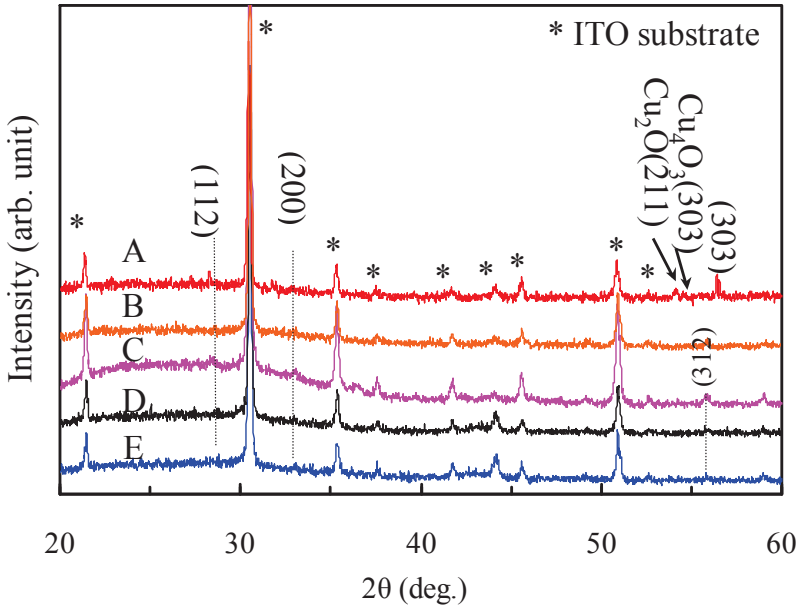

Fig. 3.9. X-ray diffraction patterns of the CZTSO films (A, B, C, D, E).

largest number of photons among the samples. However, even if the number of absorbed photons is large, photoresponse will be small if recombination rate is high. Thus, the relatively large photo current for sample D implies that the defect density of sample D is comparable to or less than those of other samples. On the other hand, the optical transmission in the long-wavelength (sub-band gap) region is lower for sample D than for the other samples, as can be seen from Figure 3.6. One might suppose that this low transmission is due to a large density of gap states, but then the photosensitivity would have been lower for sample D because of recombination at defect levels. Thus the low optical transmission of sample D could be due to some other reason, e.g., scattering due to the grain structure.

Figure 3.9 shows the XRD patterns of the CZTSO films grown on ITO and the bare ITO substrate. For sample A, (112), (200) and (303) peaks of CZTS were confirmed in the XRD pattern, and Cu_2O (211) and Cu_4O_3 (303) peaks were also observed. It is considered that copper oxides were also formed because Cu/(Zn+Sn)>1 and O/S>1 for sample A. In the case sample B, C, D, E, the major peaks of the film can be indexed as (112), (200), and (312) of

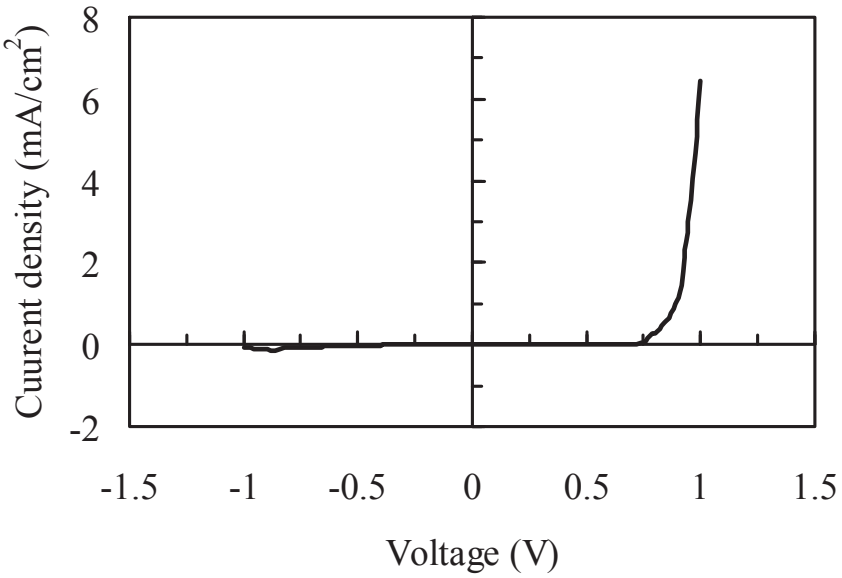

Fig. 3.10 Current-voltage characteristics of the CZTSO/ ZnO/ ITO heterojunction cell (sample D).

CZTS. However, the peaks were very weak, probably because the films were not annealed or sulfurized and thus would be nanocrystalline or amorphous. The peaks of the copper oxides were not confirmed for samples B -E because oxygen amount was reduced to 20% - 10% as can be seen from Table 3.1.

Figure 3.10 shows the results of the current-voltage measurement in the dark for the heterostructure based on sample D. Rectification properties were observed, but the leakage current is large, about 0.15 mA/cm^2 at -1.0 V. The heterostructure based on the other CZTSO samples also show similar rectifying behavior. However, the efficiency of those solar cells is very low probably because of the leakage current. Research is now in progress to improve efficiency by modifying the CZTSO deposition condition.

3.4 The sulfurization of CZTSO thin films

As the as-deposited film, we selected sample D. Figure 3.11 shows the AES spectra of the as-deposited film and the sulfurized films. Before sulfurization, the composition of the as-deposited film is $Cu_{1.9}Zn_{1.4}Sn_{1.1}S_{2.1}O_{1.6}$. After sulfurization, the composition of the sulfurized film is $Cu_{0.9}Zn_{2.1}Sn_{1.4}S_{7.6}O_{0.4}$. The intensity of the oxygen element decreased significantly with sulfurization. However, the Cu and Zn contents also varied slightly. The composition depth profiles were obtained by AES. Figure 3.12 shows the depth profiles of the metal content ratios for the as-deposited film. From the surface to the ITO substrate, composition is Cu-poor and Zn-rich, and approximately uniform. Figure 3.13 shows the depth profiles of the metal element content for the sulfurized film. The composition is still Cu-poor and Zn-rich, but Cu content was reduced near the surface (about 0-150 nm). On the other hand, Zn content was increased significantly near the surface (about 0-150 nm). We can see that the Zn/Sn ratio became lower, and the Cu/(Zn+Sn) ratio slightly higher than that of the as-deposited film in the 150-400 nm range. Zn and Cu elements were redistributed to the bulk of the film during the sulfurization.

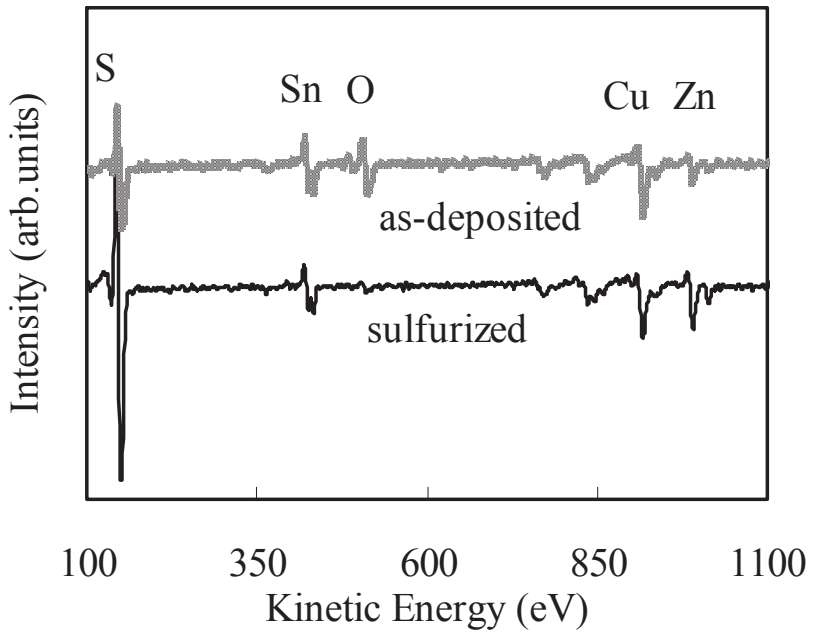

Fig. 3.11. AES spectra for the as-deposited and sulfurized films.

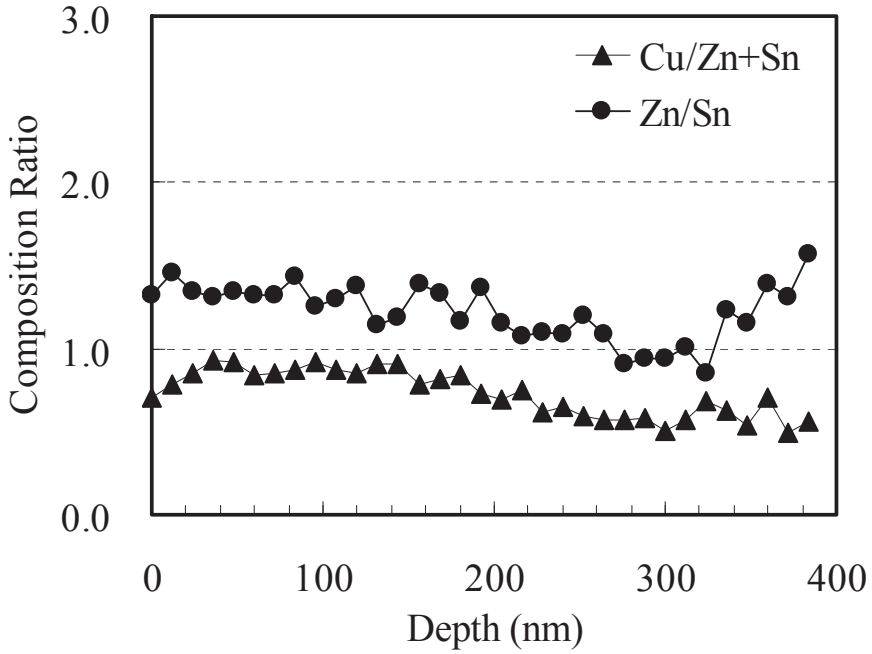

Fig. 3.12. AES spectra depth profiles for the as-deposited film.

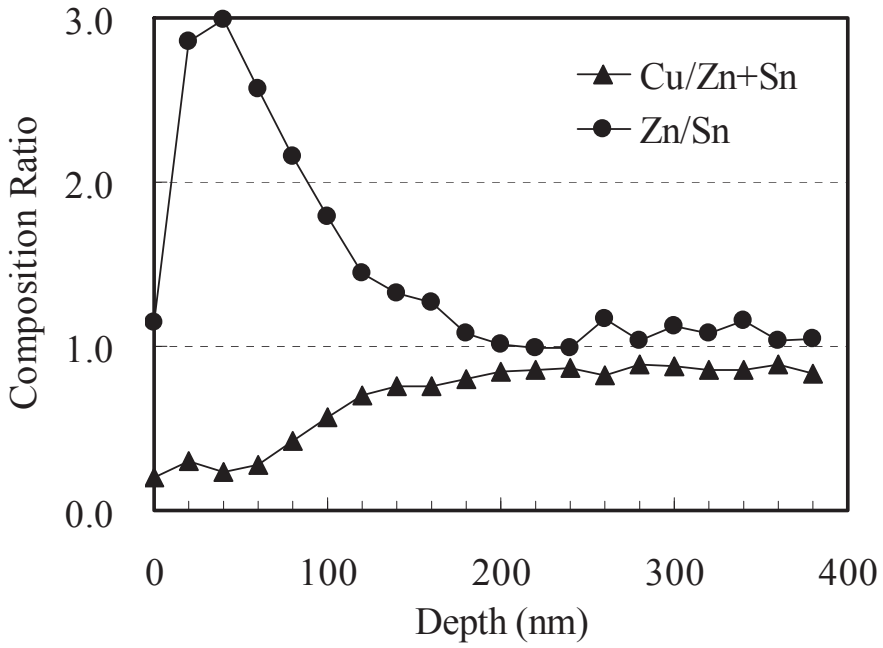

Fig. 3.13. AES spectra depth profiles for the sulfurized film.

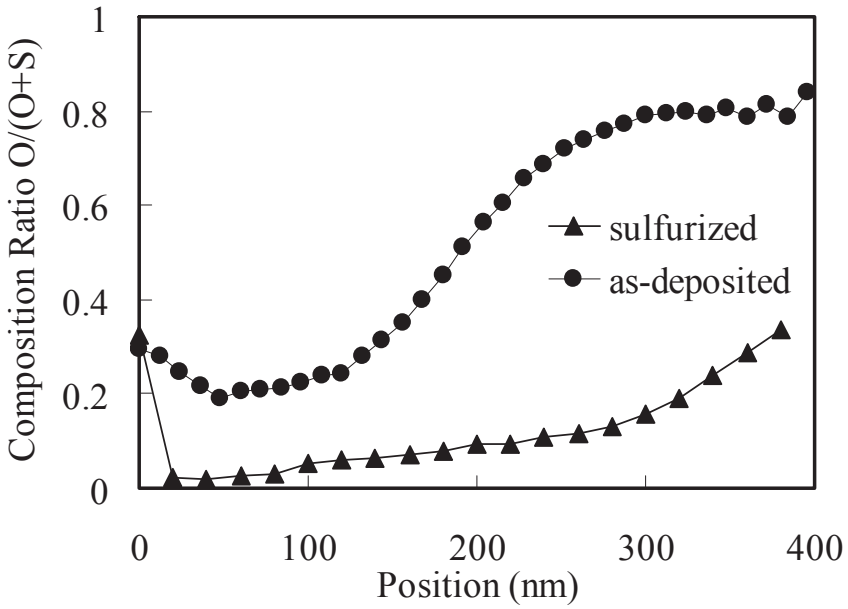

Fig. 3.14. Composition ratios O/(S+O) before and after sulfurization.

The compositions ratio of S and O is shown in Figure 3.14 for the as-deposited and the sulfurized films. After the sulfurization, the composition ratio O/(S+O) decreased significantly in the 0-400 nm range. O amount slowly increased because of ITO near the ITO substrate.

Figure 3.15 shows the SEM image of before and after the sulfurization. The grain size of the sulfurized film became larger and more uniform than that of the as-deposited film.

Figure 3.16 shows the optical transmission spectra of the as-deposited and sulfurizated films. The transmission of the sulfurized film is higher than that of the as-deposited film. This could be because the defect density was reduced by the sulfurization. We can see an absorption edge near 800 nm. The bandgap energy of the as-deposited and sulfurized films was estimated from the optical transmission spectrum. Figure 3.17 shows the bandgap of the as-deposited and sulfurized films. The bandgap of the sulfurized film was about 1.5 eV for a 0.3 μm-thick film, which agrees fairly well with those previously reported for CZTS films [3-5].

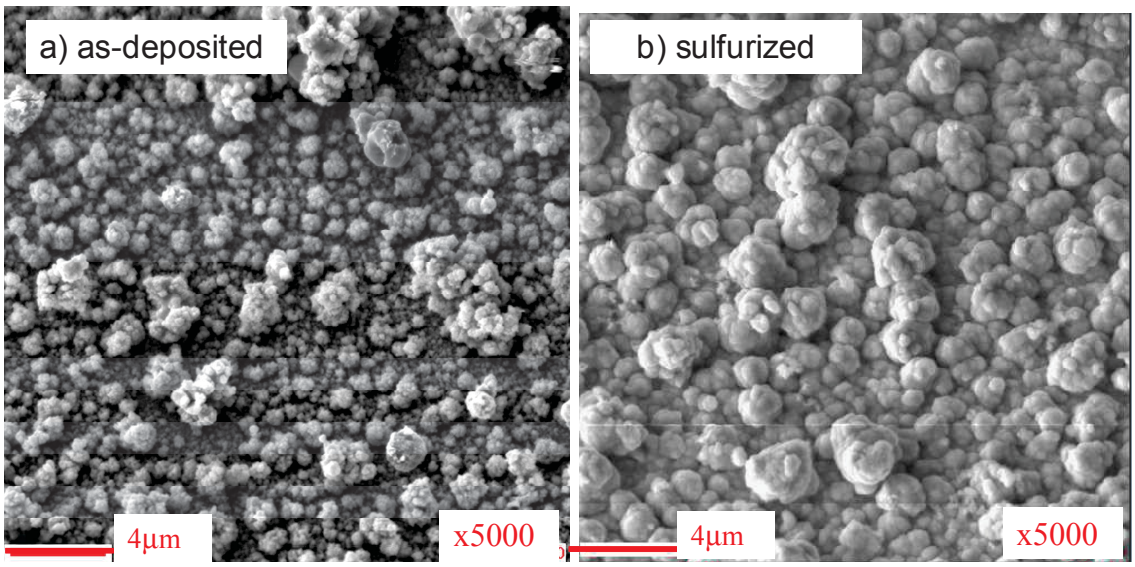

Fig. 3.15. SEM image of the surface of the as-deposited and sulfurized film.

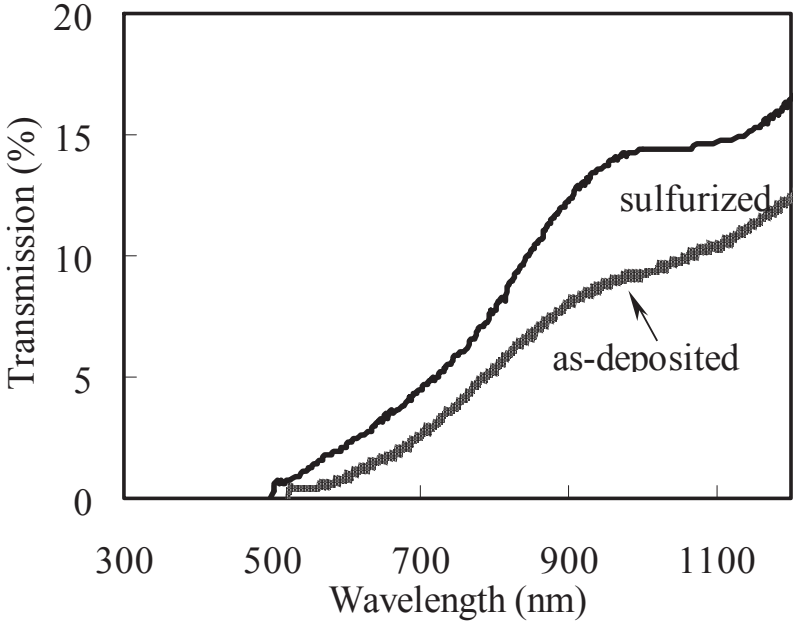

Fig. 3.16. Optical transmission spectra for the as-deposited and sulfurized films.

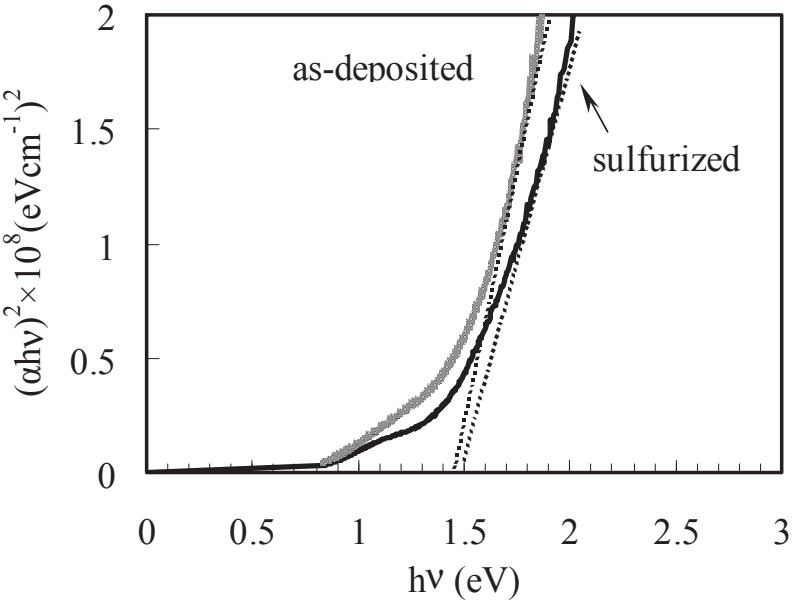

Fig. 3.17. Bandgap estimation of the as-deposited and sulfurized films.

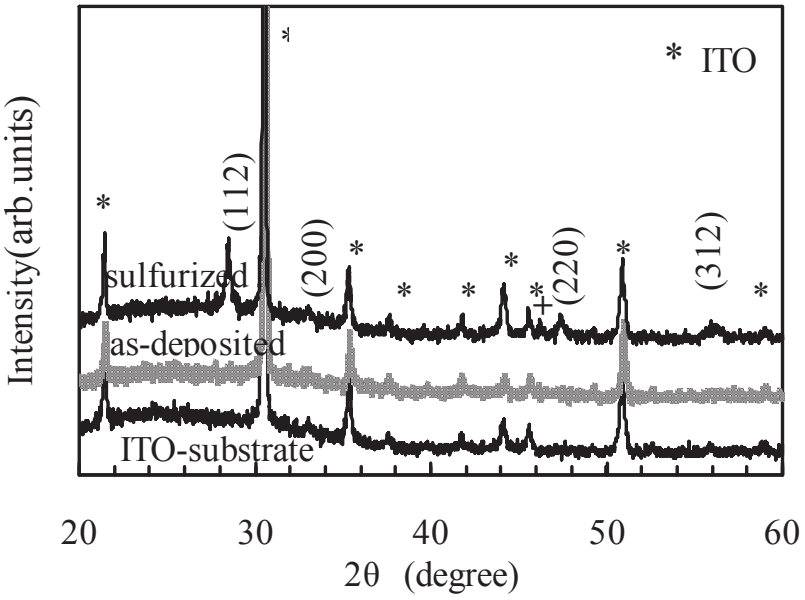

Fig. 3.18. XRD patterns of the as-deposited and sulfurized films on the ITO substrate.

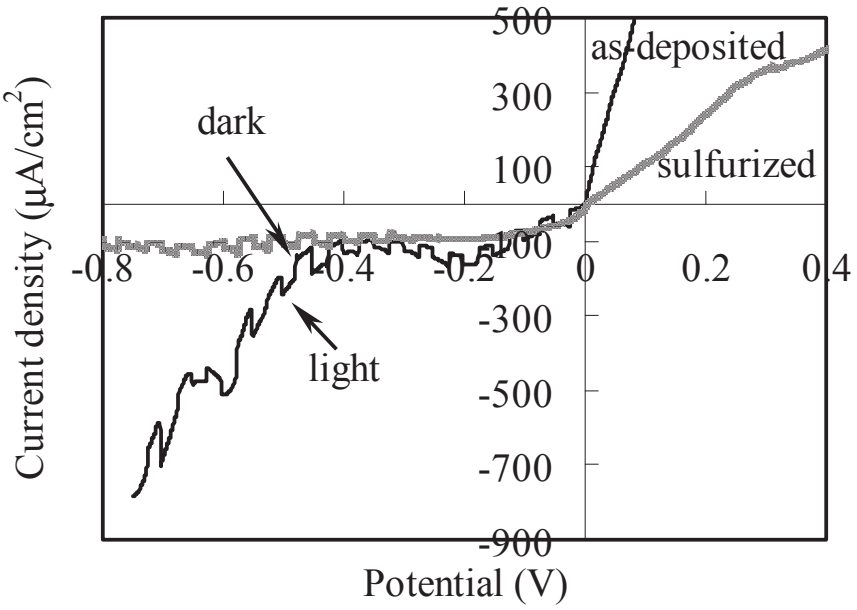

Fig. 3.19. PEC measurement results of the as-deposited and sulfurized films.

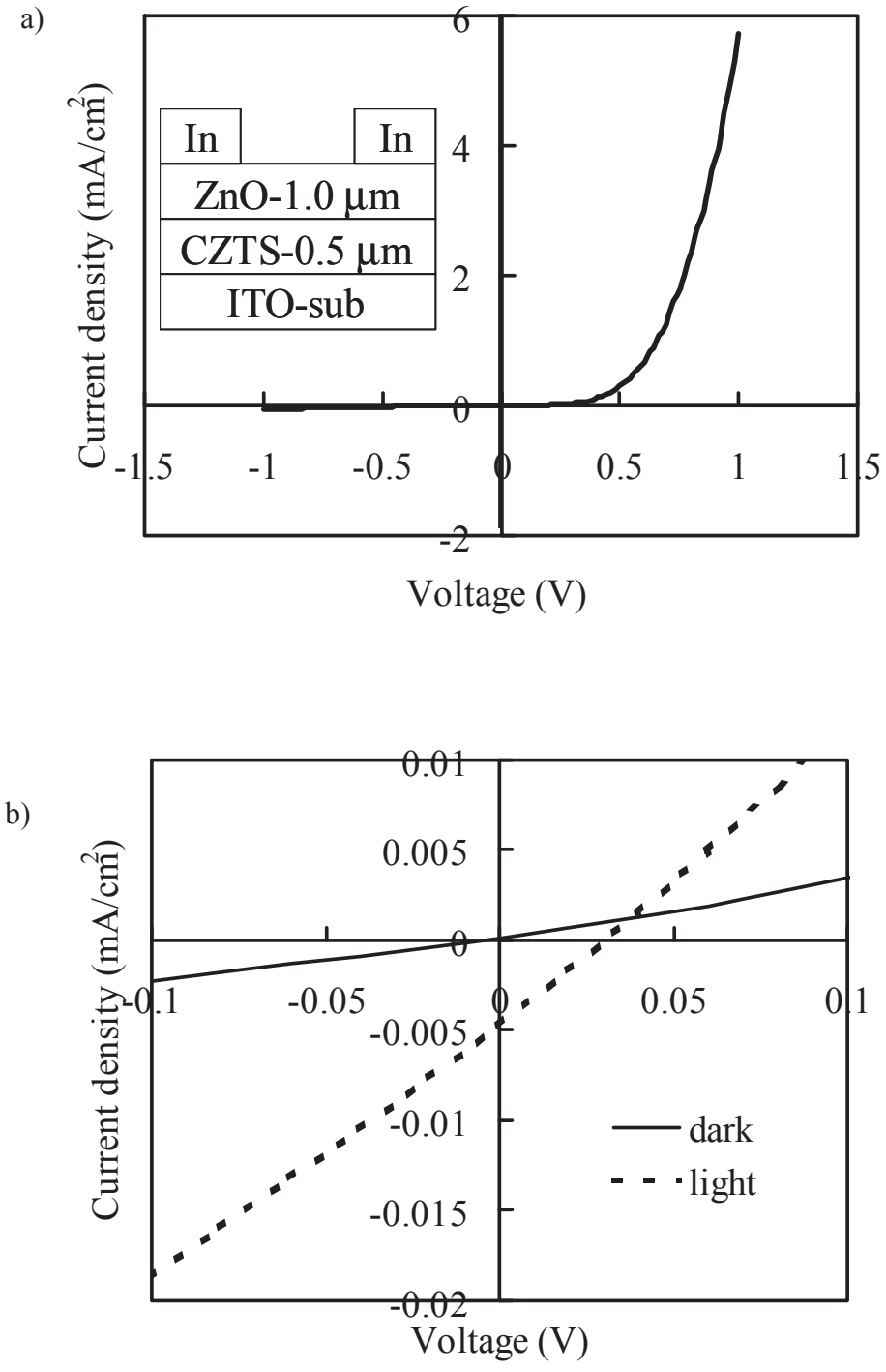

Fig. 3.20. a) I-V characteristics,

and b) photovoltaic effect of the ZnO/sulfurized CZTS/ ITO heterojunction cells.

Figure 3.18 the XRD pattern measured for the as-deposited and sulfurized films on the ITO substrate. After the sulfurization, the peaks of CZTS were confirmed, and those peaks are stronger than those of the as-deposited film. This indicated that the sulfurized film is polycrystalline. The unknown peak (marked by + in Fig. 3.18) was also observed, and that peak may possibly be due to $Cu_2Zn_2S_3$ [25] or Cu_xS (JCPDS Files No. 56-1256).

Figure 3.19 shows the photocurrent response in the PEC measurement of the as-deposited and sulfurized films. From the figure, we confirmed that both the films are p-type semiconductor. We can see that the as-deposited film has a week photosensitivity, and that after the sulfurization, the photosensitivity increased.

Figures 3.20. a) and b) show the rectification properties and photovoltaic effect of the ZnO/sulfurized CZST/ITO heterojunction solar cell, respectively. However, open circuit voltage (V_{oc}) and short circuit current (I_{sc}) are very small, and thus the quality of the sulfurized film must be improved.

3.5 Conclusions

In this work, the DC and two-step pulsed ECD methods have been applied for fabricating CZTSO absorber layers for thin film solar cells. Oxygen amount in the film is smaller for the films deposited by pulsed ECD than that deposited by DC ECD, and composition is more Cu-poor for larger negative deposition potential. P-type conductivity and photosensitivity of the films are confirmed by the PEC measurement, and the pn heterojunction with ZnO shows rectification properties. After the sulfurization, the oxygen amount decreased clearly, relatively strong XRD peaks of CZTS were observed, and weak photovoltaic effects were confirmed.

References

[1] D.A.R. Barkhouse, O. Gunawan, T. Gokmen, T.K. Todorov, and D.B. Mitzi, Prog. Photovolt, Res. Appl. 10 (2011) 1002.

[2] T. Washio, T. Shinji, S. Tajima, T. Fukano, T. Motohiro, K. Jimbob and H. Katagiri, J. Mater. Chem. 22 (2012) 4021.

[3] H. Araki, Y. Kubo, K. Jimbo, W.S. Maw, H. Katagiri, M. Yamazaki, K. Oishi, and A. Takeuchi, Phys. Status Solidi (C), 6 (2009) 1266.

[4] A. Ennaoui, M. Lux-Steiner, A. Weber, D. Abou-Ras, I. Kötschau, H.-W. Schock, R. Schurr, A. Hölzing, S. Jost, R. Hock, T. Voß, J. Schulze, and A. Kirbs, Thin Solid Films 517 (2009) 2511.

[5] J.J. Scragg, P.J. Dale, L.M. Peter, G. Zoppi, and I. Forbes, Phys. Stat. Sol. (b)245 (2008) 9.

[6] M. Jeon, T. Shimizu, and S. Shingubara, Materials Letters 65 (2011) 2364.

[7] S.M. Pawar, B.S. Pawar, A.V. Moholkar, D.S. Choi, J.H. Yun, J.H. Moon, S.S. Kolekar, J.H. Kim, Electrochimica Acta 55 (2010) 4057.

[8] Y. Cui, S. Zuo, J. Jiang, S. Yuan, and J.Chu, Sol. Energy Mater. Sol. Cells 95 (2011) 2136.

[9] M.A. Contreras, K. Ramanathan, J. AbuShama, F. Hasoon, D.L. Young, B.Egaas, and R. Noufi, Prog. Photovolt. Res. Appl. 13 (2005) 209.

[10] M.T. Htay, Y. Hashimoto, N. Momose, K. Sasaki, H. Ishiguchi, S. Igarashi, K. Sakurai, and K. Ito, Jpn. J. Appl. Phys. 50 (2011) 032301.

[11] F. Kang, J. Ao, G. Sun, Q. He, and Y. Sun, Mater. Chem. Phys. 115 (2009) 516.

[12] F. Kang and M. Ichimura, Thin Solid Films 519 (2010) 725.

[13] K. Yang and M. Ichimura, Jpn. J. Appl. Phys. 50 (2011) 040202.

[14] M. Izaki and T. Omi, J. Electrochem. Soc. 143 (1996) L53.

[15] S. Peulon and D. Lincot, Adv. Mater. 8, 166 (1996).

[16] J. J. M. Vequizo, J. Wang, and M. Ichimura, Jpn. J. Appl. Phys. 49 (2010) 125502.

[17] S. T. Chang, I. C. Leu, and M. H. Hon, Electrochem. Solid-State Lett. 5 (2002) C71.

[18] A. E. Rakhshani, A. A. Al-Jassar, and J. Varghese, Thin Solid Films 148 (1987) 191.

[19] T. D. Golden, M. G. Shumsky, Y. Zhou, R. A. VanderWerf, R. A. Van Leeuwen, and J. A. Switzer, Chem. Mater. 8 (1996) 2499.

[20] K. Omoto, N. Fathy, M. Ichimura, Jpn. J. Appl. Phys. 45 (2006) 1500.

[21] N. Fathy and M. Ichimura, Jpn. J. Appl. Phys. 44 (2005) L1295.

[22] T. Washio, H. Nozaki, T. Fukano, T. Motohiro, K. Jimbo, and H. Katagiri, Journal of Applied Physics 110 (2011) 074511.

[23] H. Katagiri, K. Jimbo, S.W. Maw, K. Oishi, M. Yamazaki, H. Araki, and A. Takeuchi, Thin Solid Films 517 (2009) 2455.

[24] Q. Guo, G.M. Ford, W.C. Yang, B.C. Walker, E.A. Stach, H.W. Hillhouse, and R. Agrawal, J. Am. Chem. Soc. 132 (2010).

[25] N. Kitagawa, S. Ito, D.C. Nguyen and H. Nishino, Natural Resources 4 (2013) 142.

Chapter 4
Electrochemical Deposition of Fe-S-O Thin Films

4.1 Introduction

Iron pyrite (FeS_2) is an attractive semiconducting material consisting of non-toxic and earth abundant elements, since FeS_2 is suitable for an absorber in a thin film solar cell owing to its large optical absorption coefficient over 10^5 cm^{-1} in the near-infrared and visible light region [1,2]. Many methods have been used for the preparation of thin pyrite films, such as low pressure chemical vapor deposition [3], spray pyrolysis [4], sulfurization of electrodeposited films [5,6], sulfurization of sputtered [7] or vacuum evaporated [8,9] iron films, sol-gel [10,11], and chemical bath deposition [12]. More recently, use of ink technology is also reported, where precursor films of molecular inks composed of iron complexes and elemental sulfur were spin-coated and annealed [13].

However, the band gap of FeS_2 (0.95 eV) is in fact smaller than the optimum one for solar cells (about 1.5 eV [14]). FeS_xO_y will have a larger band gap than FeS_2 and thus could be more suitable for photovoltaics. Several metal sulfide-oxides materials such as SnS_xO_y [15], $Cu_xSn_yS_zO$ [16] and Cu-Zn-Sn-S-O [17] have been fabricated by the electrochemical deposition (ECD) in our group. ECD is a cost-effective technique, and its advantage over other solution methods is the possibility of controlling film properties and thickness through the electrochemical variables. So far, there have been reports on the fabrication of FeS_xO_y by ECD [18] and photochemical deposition (PCD) [19]. While the conduction type was found to be n-type for the PCD FeS_xO_y film, the conduction type of the ECD film was not reported. Moreover, fabrication of any heterostructure devices based on FeS_xO_y has never been attempted. In this work, we deposited FeS_xO_y thin films by ECD. A ZnO/ FeS_xO_y heterostructure was fabricated, and rectification properties were confirmed for the first time. Moreover, the effects of annealing on FeS_xO_y thin films were investigated.

4.2. Experimental details

A three-electrode cell was used for ECD with a saturated calomel electrode (SCE) as the reference electrode. Indium-tin-oxide (ITO)-coated glass was used as the working electrode (substrate) and a platinum sheet was used as the counter electrode. In the following, all the potential values are vs SCE. Hokuto denko function generator HB-305 and potentiostat/ galvanostat HA-151B were used as the voltage source. Both the ITO substrate and the platinum sheet were washed ultrasonically in alkyl benzene and dried in nitrogen before the experiment. The deposition area was about 1x1 cm^2. The deposition solution contained $FeSO_4$ and 100 mM $Na_2S_2O_3$. It should be noted that all the above deposition potential was determined on the basis of the cyclic voltammetry (CV). The cathodic scan was from 0 to −1.5V and the anodic scan was from −1.5V to +0.5V with a scan rate of 20 mV/s. The deposition potential range was determined on the basis of the cyclic voltammetry (CV). In order to investigate dependence of composition on various parameters, the deposition temperature was varied from 15 to 60ºC, the deposition potential from –0.8 to –1.0 V, and the $FeSO_4$ concentration from 20 to 40mM. The solution pH was unadjusted, and the deposition time is 5 min. After the deposition, the deposited films were washed in pure water and naturally dried in air.

Iron sulfide is expected to be formed by the following mechanism, as reported for other sulfides. Elemental sulfur is released from $S_2O_3^{2-}$ by the reaction.

$$S_2O_3^{2-} + 2H^+ = S + H_2SO_3. \qquad (1)$$

Then iron sulfide is formed at the cathode by the reaction

$$Fe^{2+} + xS + 2e^- = FeS_x. \qquad (2)$$

For the oxide formation, one can consider dissolved oxygen and OH^- ions as the oxygen

source. Since the solution is weakly acidic, the dominant oxygen source would be dissolved oxygen. Then iron oxide can be formed by the following reaction.

$$2Fe^{2+} + yO_2 + 4e^- = 2FeO_y . \quad (3)$$

With reactions (2) and (3) proceeding simultaneously, FeS_xO_y is expected to be formed.

The annealing was carried out at 100, 200, 300 and 400ºC in nitrogen atmosphere for an hour.

Compositional analysis was carried out by Auger electron spectroscopy (AES) using a JEOL JAMP 9500 Auger microprobe at a probe voltage of 10 kV and a current of 10 nA. Argon ion etching with an acceleration voltage of 2.5 kV and a current of 8 mA was used to sputter the film surface. The scanning electron microscope (SEM) observation was also performed using JEOL JAMP 9500 at a constant acceleration voltage of 10 kV and a magnification of 5000. The films thickness was measured by an Accretech Surfcom-1400D profile meter. The optical transmission measurement was performed using a JASCO U-570 spectrometer with the substrate as the reference. X-ray diffraction (XRD) was measured using a Rigaku Smartlab diffractometer with a Cu Kα radiation source. The Raman spectra excited by a 632.8 nm He-Ne laser were collected using JASCO NRS 3300 spectrometer. The laser power was set low (0.9 mW), because high laser power could lead to decomposition of the deposited films. Furthermore, to determine the type of conduction and to estimate the photosensitivity, photoelectrochemical (PEC) measurements were carried out using the same potentiostat as used for the deposition. The three-electrode cell with a solution containing 100 mM $Na_2S_2O_3$ was used. The light was incident from a xenon lamp toward the backside of the sample. The incident light (about 100 mW/cm^2) was turned off and on mechanically every 5 s by inserting and removing a barrier between the lamp and the sample. This light chopping was performed under the application of a ramp voltage, first in the cathodic bias range (0 to -1 V) and then in the anodic bias range (0 to +1 V).

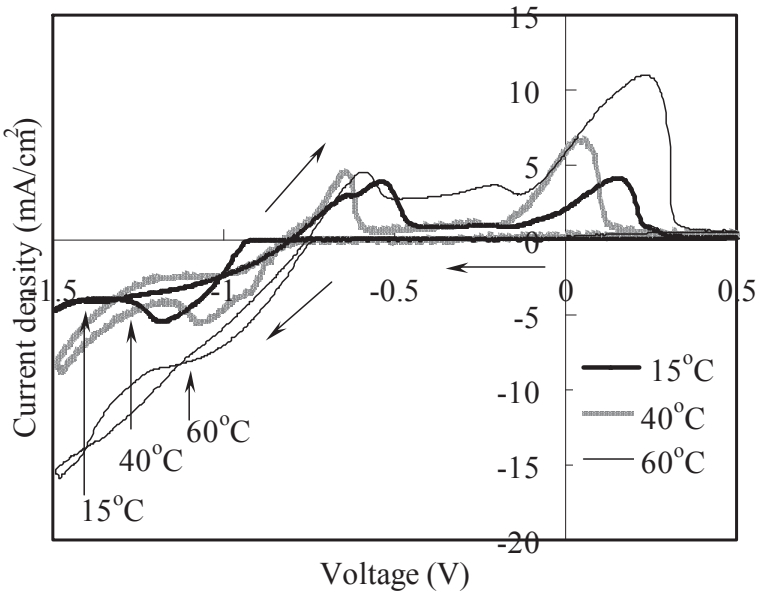

Fig. 4.1. CV measurement for different solution temperatures 15ºC, 40ºC and 60ºC ($FeSO_4$ concentration 40mM).

ZnO was also deposited by ECD using an aqueous solution containing 0.1 M $Zn(NO_3)_2$ [20]. The deposition temperature was 60ºC. The deposition bias was a two-step pulse with V_1 = -1.3V and V_2 = -0.6 V, and the duration of each pulse was 10s. The deposition time was 2 min, and the film thickness was about 0.5 μm. Indium was evaporated as electrodes on the ZnO/ FeS_xO_y / ITO structure.

4.3. Results and discussion

We investigate dependences of FeS_xO_y deposition on a) solution temperature, b) potential, and c) $FeSO_4$ concentration.

Figure 4.1 shows the CV measurement results obtained on the ITO substrate for the solution containing $Na_2S_2O_3$ 100 mM and 40 mM $FeSO_4$ at the different solution temperatures. pH was 5.6 (unadjusted). The negative current was not observed at potentials more positive than –0.7 V. A stable film was not obtained at potentials more negative than –1.0 V: after

deposition, the thin film was peeled off from the substrate. Thus, we performed the deposition at potentials from –0.8 to –1.0 V.

The composition obtained by AES are shown in Figure 4.2 for the films deposited at different temperatures. The deposition potential was fixed at –0.8 V and the $FeSO_4$ concentration at 40 mM. The Fe content did not vary significantly and in a range of 33~37 %. However, O and S contents depend strongly on the solution temperature. At 60ºC, sulfur precipitations were formed in the solution, and thus S content in the film was lower than that of films deposited at lower temperatures.

Figure 4.3 shows SEM images of the samples deposited at the different temperatures. The grain size of the sample deposited at 15ºC is larger than that of the 40ºC-deposited sample, but surface roughness is larger for the 15ºC-deposited sample. Holes were be observed on the surface of the 60ºC-deposited sample. The film seems relatively uniform and compact when deposited at 40ºC.

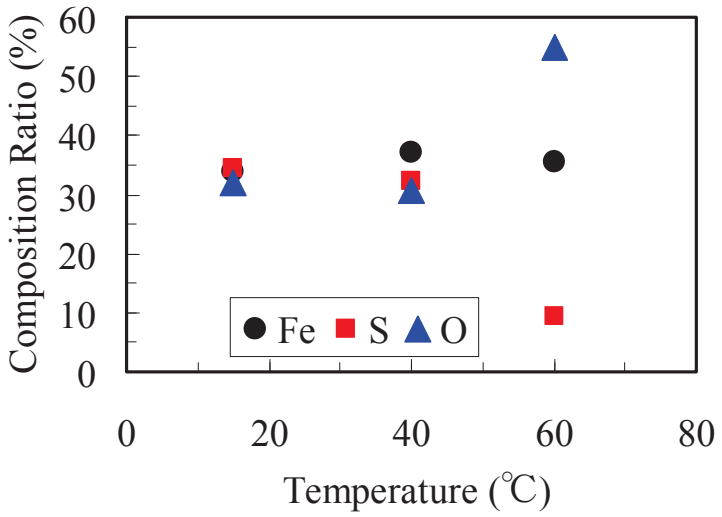

Fig. 4.2. Composition of FeS_xO_y films deposited at different temperatures. (The potential was –0.8 V, and the $FeSO_4$ concentration 40mM).

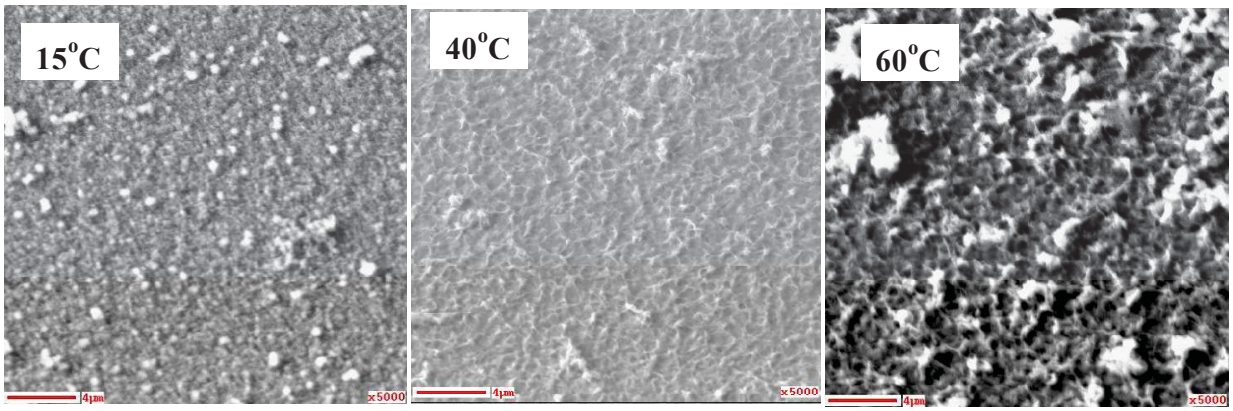

Fig. 4.3. SEM photograph of the surface of the FeS_xO_y film.

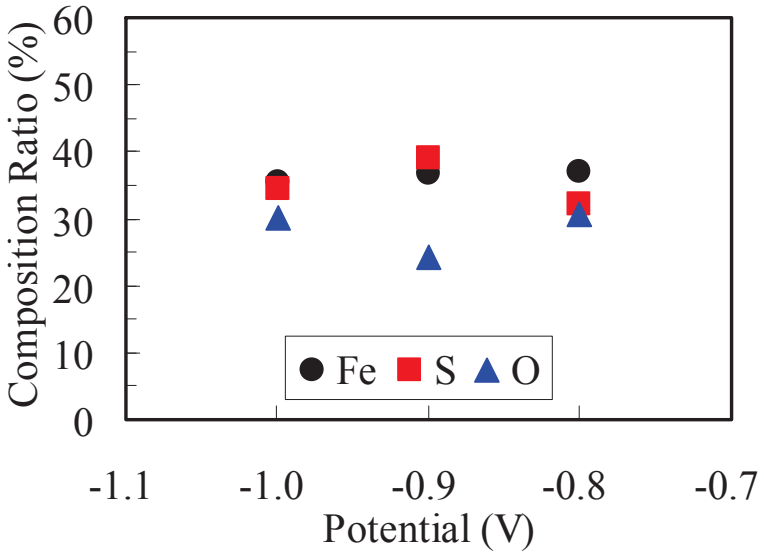

Fig. 4.4. Composition of FeS_xO_y films deposited at different potentials.

(The temperature was 40°C, and the $FeSO_4$ concentration 40 mM)

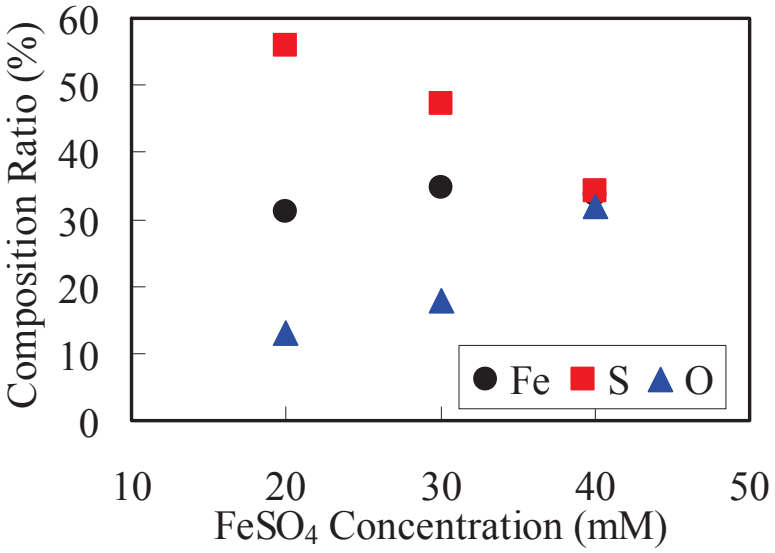

Fig. 4.5. Composition of FeS_xO_y films deposited with different $FeSO_4$ concentrations. (The temperature was 15°C, and the potential -1.0V)

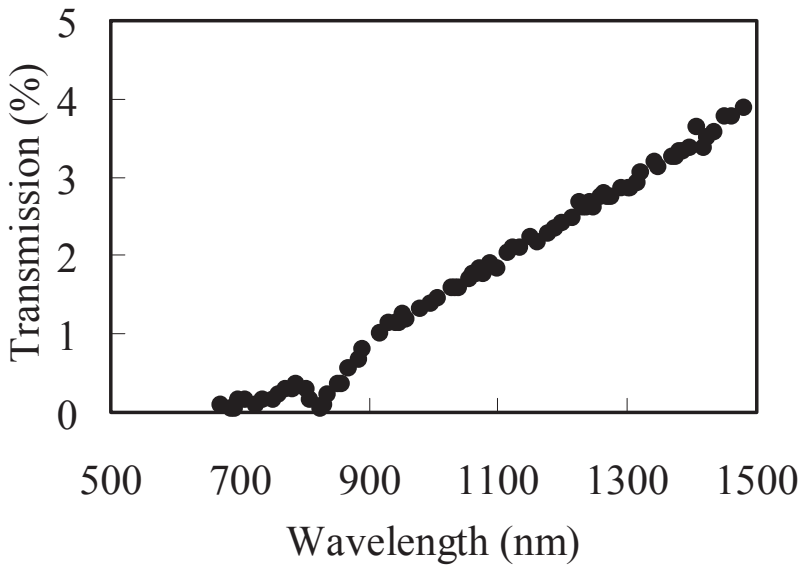

Fig. 4.6. Optical transmission spectrum for the FeS_xO_y film.

Figure 4.4 shows the dependence of composition on the deposition potential. The deposition temperature was fixed at 40ºC and the $FeSO_4$ concentration at 40 mM. The composition did not depend significantly on the deposition potential. Figure 4.5 shows the results for different $FeSO_4$ concentrations with the temperature fixed at 15ºC and the potential at –1.0 V. The oxygen content increased with increasing $FeSO_4$ concentration.

In the following, the deposition temperature is set 40ºC, the deposition potential –0.8 V, and the $FeSO_4$ concentration 40 mM. pH was 5.6 (unadjusted). The composition obtained by AES is Fe:S:O ≈ 1:1:1 under that condition. An about 0.5 μm-thick black film was obtained with the 5 min deposition.

Figure 4.6 shows the optical transmission spectrum of the FeS_xO_y film. The optical transmission is lower than 10% for a 0.5 μm-thick film, and we found a change in the slope around 900 nm, which would corresponds to an absorption edge. The optical band gap energy was calculated from the classical relation for direct-band optical absorption, $\alpha = k(h\nu - E_g)^{1/2}/h\nu$, where k is a constant, E_g is the band gap, and hν is the photon energy. Figure 4.7 shows

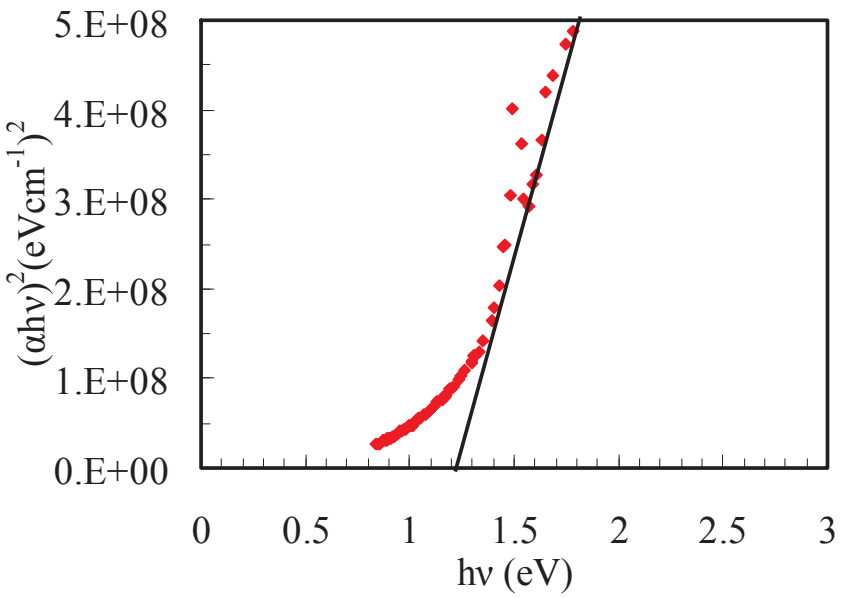

Fig. 4.7. The bandgap estimation of the FeS_xO_y film.

the bandgap of the FeS_xO_y film. The direct energy band gap estimated from the optical transmission approximately equals 1.2 eV. This band gap is larger than that of FeS_2. We attempted to calculate the indirect bandgap, but the plot of $(\alpha h\nu)^{1/2}$ vs. hν does not give a reasonable value of E_g.

Figure 4.8 shows the PEC measurement results for the FeS_xO_y films. The photo-response was observed in both the polarity, but the negative photocurrent under the negative bias is higher than the positive photocurrent under the positive bias. Accordingly, the film would be a p-type semiconductor.

Figure 4.9 shows the XRD pattern measured for the FeS_xO_y film grown on the ITO substrate. Only the diffraction peaks due to ITO were observed, and thus the film is considered to be amorphous. On the other hand, since there are not peaks due to elemental Fe, we can conclude that Fe is chemically bonded to S or O.

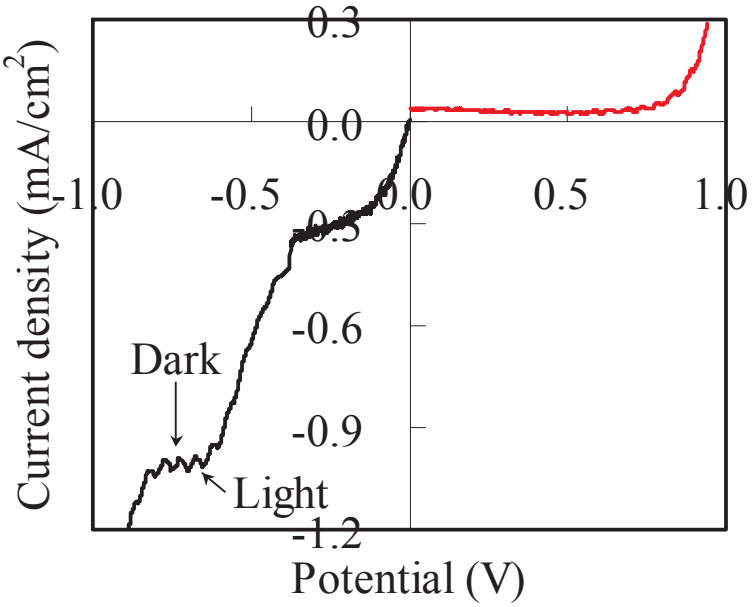

Fig. 4.8. PEC measurement results of the FeS_xO_y film.

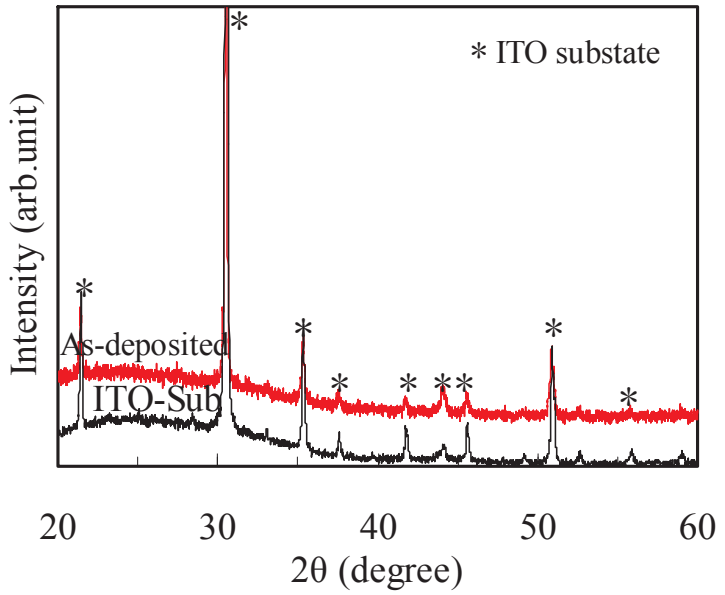

Fig. 4.9. X-ray diffraction pattern of the FeS_xO_y film on the ITO substrate.

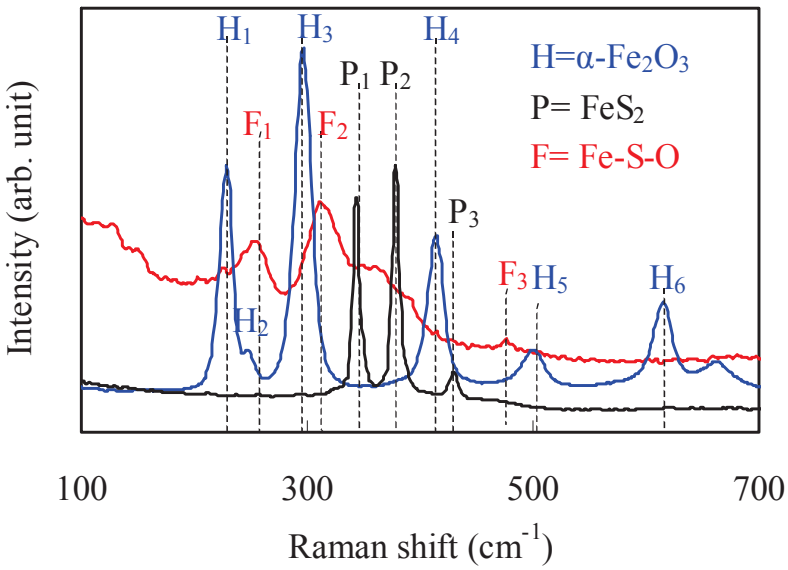

Fig. 4.10. Raman spectra of FeS_xO_y, hematite (α-Fe_2O_3), and pyrite (FeS_2).

Figure 4.10 shows the Raman spectra of the FeS_xO_y thin film with the spectra for hematite (α-Fe_2O_3) and pyrite (FeS_2) shown for comparison. If deposited FeS_xO_y is a composite of iron oxides and sulfides (i.e., Fe is bonded to either O only or S only), then the peaks for iron oxides and sulfides will be observed. However, the peak frequencies for FeS_xO_y are distinctly different from those for α-Fe_2O_3 or FeS_2, as shown in Figure 4.10. The peak frequencies for FeS_xO_y do not agree with those for other oxide and sulfide phases, either. Therefore, we may consider that Fe atoms in FeS_xO_y are bonded to both O and S atoms so that new vibrational bands are formed.

Figure 4.11 shows the results of the current-voltage measurement in the dark for the ZnO/FeS_xO_y heterostructure. In the figure, the positive voltage means that the FeS_xO_y side of the sample was positively biased with respect to the ZnO side. Thus, this result shows that an n-ZnO/p-FeS_xO_y rectifying junction was formed. The leakage current is about $1x10^{-2}$ mA/cm^2 at -1.0 V. The I-V characteristic under the illumination condition showed a photo response, but a photovoltaic effect was not observed.

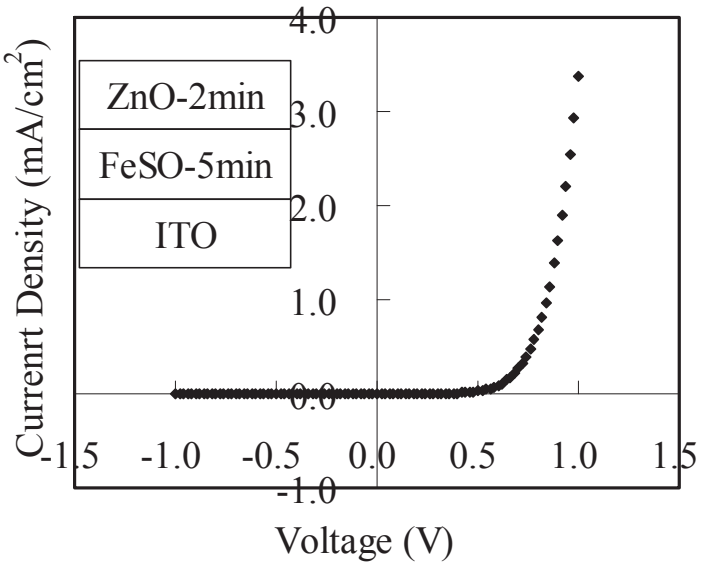

Fig. 4.11. Current-voltage characteristics of the ZnO/ FeS_xO_y / ITO heterojunction cell.

4.4 Annealing study of FeS_xO_y

Figure 4.12 shows the atomic composition ratio of the as-deposited and annealed films. The results revealed that the Fe content did not vary significantly. However, O and S contents strongly depend on the annealing temperature. The oxygen content increased as the annealing temperature was increased above 200º C. Although the annealing was carried out under the flow of nitrogen gas, a trifle of oxygen would remain in the annealing furnace. Therefore, during the annealing, extra oxygen could be adsorbed at the surface and diffused to the bulk of the film to replace sulfur. S content was evaporated. This indicates that iron element was easily combined with O element, and oxidized.

Figure 4.13 shows the SEM image of the as-deposited and annealed films at the different temperatures. Holes and cracks reaching the substrate are not observed. The grain size was slightly increased with increase in annealing temperature from 100ºC to 300ºC. The morphology after annealing at 400ºC is drastically different from those of others films.

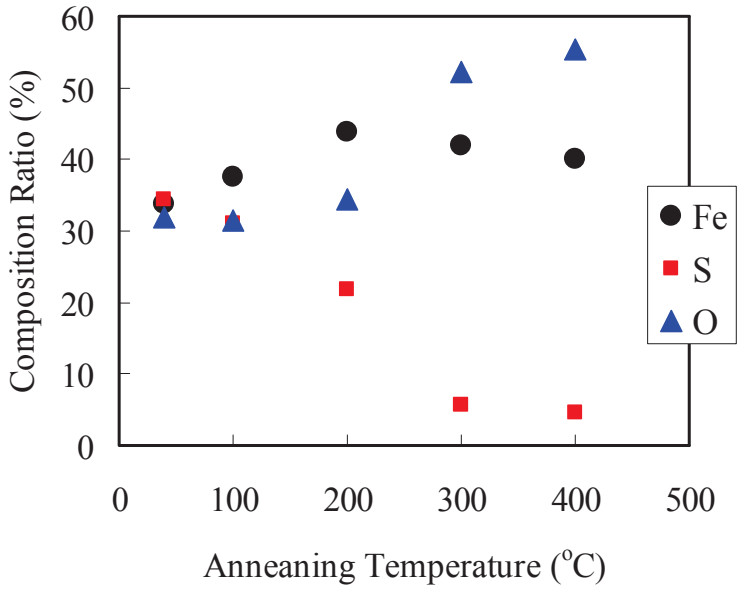

Fig. 4.12. AES spectra for the as-deposited and annealed films.

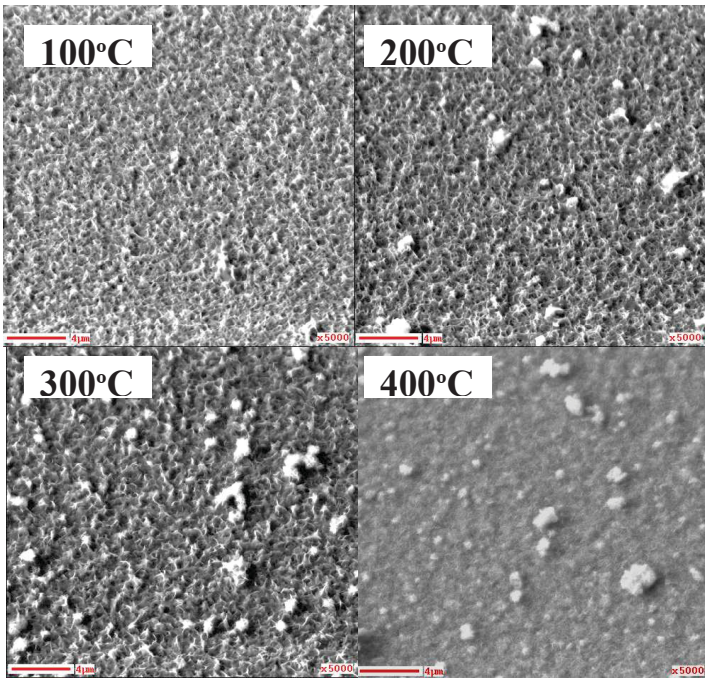

Fig. 4.13. The SEM image of the as-deposited film and the films annealed at different temperatures.

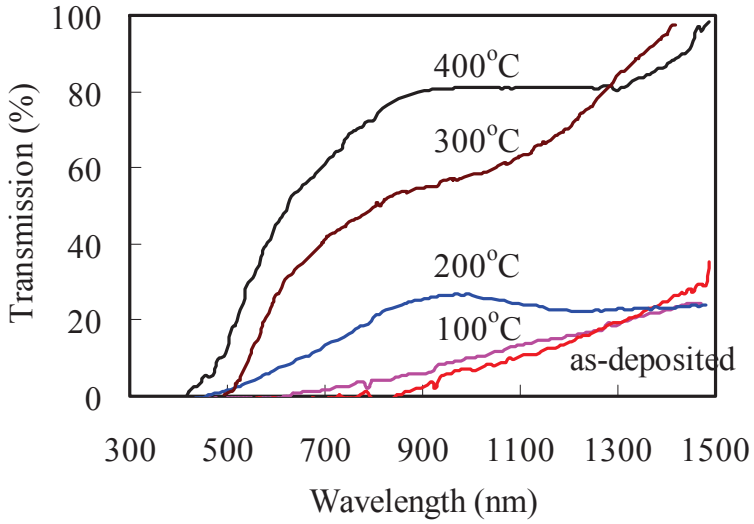

Fig. 4.14. Optical transmission spectra for the as-deposited films and the films annealed at different temperatures.

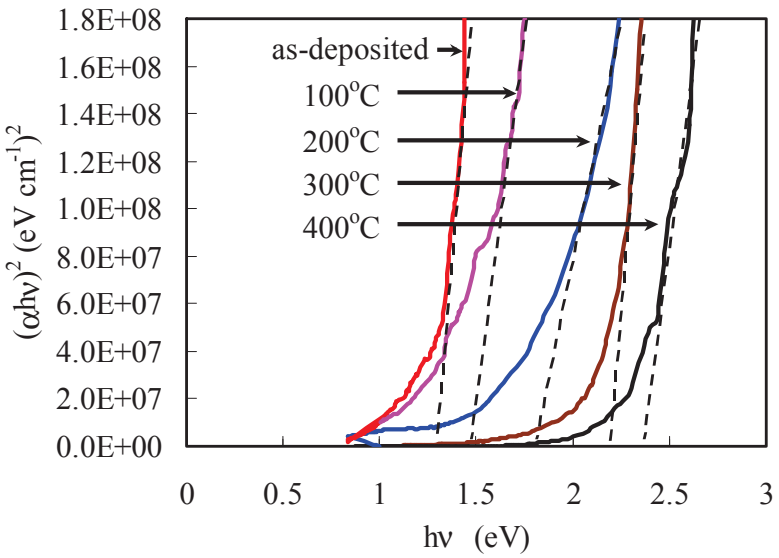

Fig. 4.15. Bandgap estimation of the as-deposited film and the films annealed at the different temperatures.

Figure 4.14 shows the dependence of optical transmission of the FeS_xO_y thin films on the annealing temperatures. The as-deposited film shows a low transmission. However, the transmission of the annealed films is higher than that of the as-deposited film. In addition, the optical transmission curves shift to a shorter wavelength with increasing annealing temperature. The annealed films show large transmission in the visible wavelength range and absorption edges at around 500-700 nm. This is because of the increase in oxygen content.

Figure 4.15 shows the energy bandgap of the as-deposited and the annealed films. The bandgap varied significantly due to the annealing. For the 400ºC annealed film the bandgap was found to be 2.4 eV, and this value is near to that of α-Fe_2O_3 (about 2.2eV). This indicates that the bandgap of the annealed films became large due to increasing oxygen content.

Figure 4.16 shows the XRD patterns of the as-deposited and annealed films. We mark the peak positions of In_2O_3 taken from the database (JCPDS Files No. 6-0416). For annealing temperatures up to 300 ºC, any peaks were not observed for the deposited film. This indicated

that FeS_xO_y films are amorphous or nanocrystalline. However, the pattern of the film annealed at 400ºC shows peaks of Fe_3O_4 (311) and (511) without any peaks for iron sulfide.

Figure 4.17 shows the results of the PEC measurement for the annealed films. The inset figure shows that the photocurrent was negative under the light illumination during the cathode biasing for the 100ºC-annealed film. After the 200ºC and 300ºC annealing, the photosensitivity became even weak. On the other hand, due to the effect of the increased oxygen content, n-type semiconductor responses were confirmed during the anodic biasing. Figure 4.18 shows the PEC measurement results for the film annealed at 400ºC. The negative photocurrent was not observed but the positive photocurrent, and therefore, we confirmed that the 400ºC-annealed film is n-type.

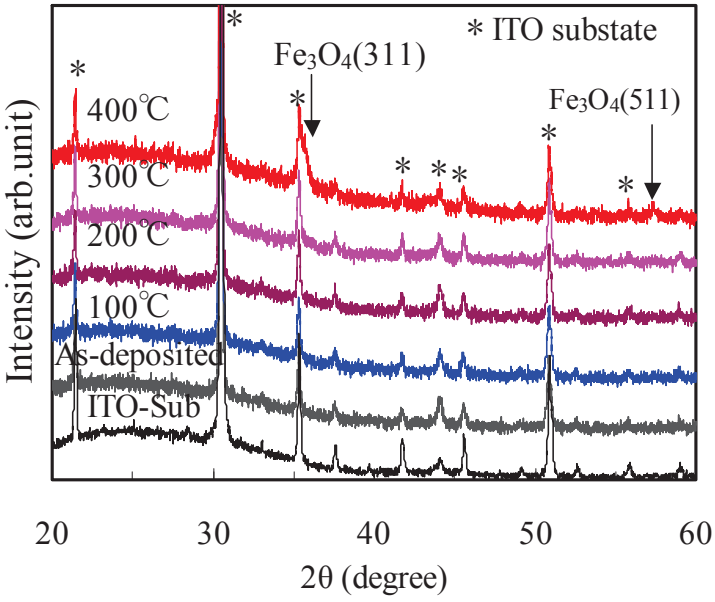

Fig. 4.16. XRD spectra of the as-deposited films and the films annealed at different temperatures.

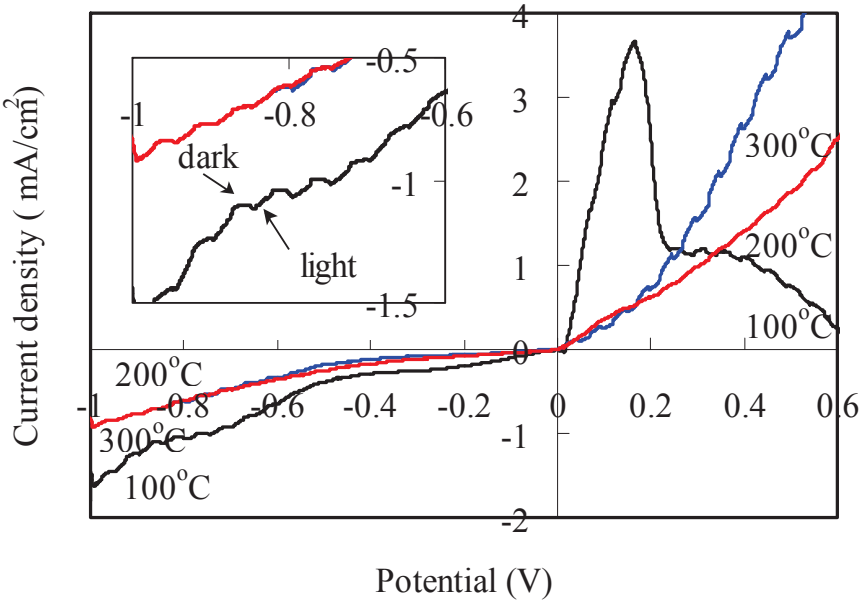

Fig. 4.17. PEC measurement results for the films annealed at 100, 200 and 300°C

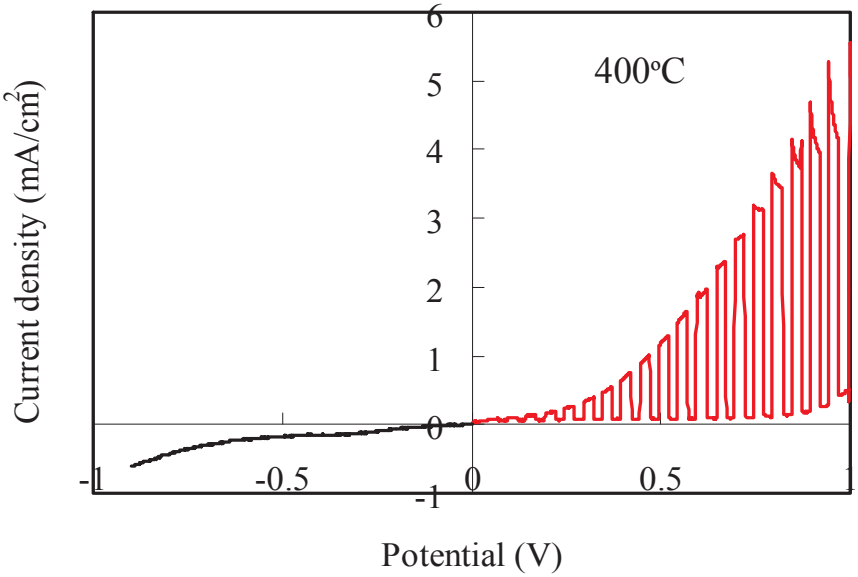

Fig. 4.18. PEC measurement result for the film annealed at 400°C.

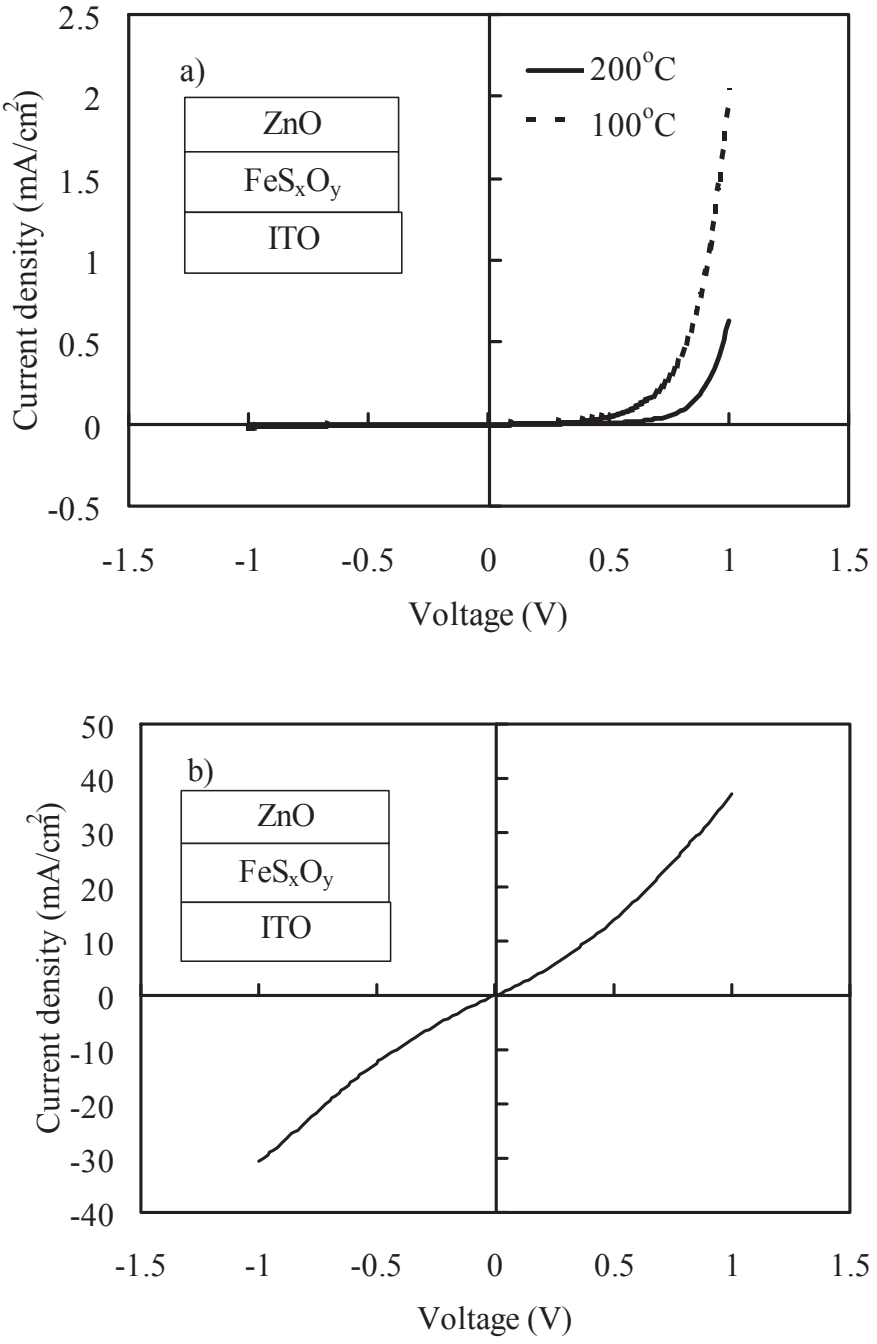

Fig. 4.19. I-V measurement of the ZnO/ annealed FeS_xO_y / ITO heterojunction cells with the FeS_xO_y films annealed a) at 100ºC and 200ºC, and b) at 300ºC.

Finally, the I-V properties of the heterojunction based on the annealed films were measured. The 400ºC-annealed films were not p-type, and thus the films annealed at 100, 200 and 300ºC were used for the heterojunction with ZnO. Figure 4.19 a) shows I-V measurement results of the heterojunctions with the 100 and 200ºC annealed films. The figure revealed that the heterojunction showed rectification properties, but photovoltaic effects were not confirmed. Compared with the as-deposited film heterojunction, the results did not change significantly. Figure 4.19 b) show I-V measurement results of the heterojunction with the 300ºC-annealed film. The results shows that when the oxygen content of the FeS_xO_y film increased, a rectifying junction was not formed with ZnO.

4.5 Conclusion

FeS_xO_y thin films were deposited by the ECD method from the deposition solution containing $FeSO_4$ and $Na_2S_2O_3$. The composition obtained by AES is Fe:S:O ≈ 1:1:1, when the $FeSO_4$ concentration is 40 mM, $Na_2S_2O_3$ concentration 100 mM, and the deposition temperature 15 ~ 40ºC. By the PEC measurement, a negative photocurrent was observed under illumination, and thus the film was considered to be p-type. The band gap was estimated to be about 1.2 eV for a 0.5 μm-thick film from the optical transmission results. A ZnO/ FeS_xO_y heterostructure was fabricated, and in the current-voltage measurement, clear rectification properties were observed. After annealing at 100 ~ 400ºC in a nitrogen atmosphere for an hour, the Fe content did not vary significantly. However, O and S contents depend on the annealing temperature. The optical transmission and the bandgap increased with increasing annealing temperature. After the 400ºC annealing, the XRD peaks of Fe_3O_4 were observed and the conduction type was changed to n-type.

References

[1] A. Ennaoui, S. Fiechter, W. Jaegermann, H. Tributsch, J. Electrochem. Soc. 133 (1986) 97.

[2] A. Ennaoui, S. Fiechter , C. Pettenkofer , N. Alonsovante , K. Buker , M. Bronold , C. Hopfner , and H. Tributsch, Sol. Energy Mater. Sol. Cells 29 (1993) 289.

[3] D.M. Schleich, H.S.W. Chang, J. Cryst. Growth 112 (1991) 737.

[4] A. Yamamoto, M. Nakamura, A. Seki, E.L. Li, A. Hashimoto, S. Nakamura, Sol. Energy Mater. Sol. Cells 75 (2003) 451.

[5] G. Pimenta,W. Kautek, Thin Solid Films 238 (1994) 213.

[6] S. Nakamura, A. Yamamoto, Electrodeposition of pyrite (FeS_2) thin films for photovoltaic cells, Sol. Energy Mater. Sol. Cells 65 (2001) 79.

[7] L. Meng, J.P. Tu, M.S. Liu, Mater. Lett. 38 (1999) 103.

[8] B. Rezig, H. Dahman, M. Kenzari, Renewable Energy 2 (1992) 125.

[9] I.J. Ferrer, C. Sanchez, J. Appl. Phys. 70 (1991) 2641

[10] H. Siyu, L. Xinyu, L. QingYu, and C. Jun, J. of Alloys and Comp. 472 (2009) L9.

[11] L. Huang, F. Wang, Z. Luan, and L. Meng, Materials Letters 64 (2010) 2612.

[12] D. A. Maz´on-Montijo, M. T. S. Nair and P. K. Nair, Journal of Solid State Science and Technology 2 (11) (2013) P465.

[13] S. Seefeld, M. Limpinsel, Y. Liu, N. Farhi, A. S. Weber, Y. Zhang, N. Berry, Y. J. Kwon, C. L. Perkins, J. C. Hemminger, R. Wu, and M. Law, J. Am. Chem. Soc. 135 (2013) 4412.

[14] J.J. Loferski: J. Appl. Phys. 27 (1956) 777.

[15] K. Omoto, N. Fathy, M. Ichimura, Jpn. J. Appl. Phys. 45 (2006) 1500.

[16] Y. Nakashima and M. Ichimura, Inter. J. Photoenergy 2012 (2012) 171432.

[17] K. Yang and M. Ichimura, Inter. J. Photoenergy 2012 (2012) 154704.

[18] H. R. Dizaji, M. Ichimura, Mater. Sci. Eng. B 158 (2009) 26.

[19] X. Han, B. Zhou and M. Tao, Photovoltaic Specialists Conference (PVSC), 38th IEEE (2012) 002528.

[20] M. Izaki and T. Omi, J. Electrochem. Soc. 143 (1996) L53.

Chapter 5
Conclusion and future work

5.1 Main conclusion of this work

Cu_xZn_yS thin films were deposited from solutions containing $Na_2S_2O_3$, $CuSO_4$ and $ZnSO_4$ by the electrochemical deposition (ECD) and photochemical deposition (PCD) methods. Firstly, Cu_xZn_yS thin films were deposited by ECD using DC biasing. We fixed the sum of the concentrations of $ZnSO_4$ and $CuSO_4$ at 30 mM, and varied the Zn/Cu ratio. The Zn content depends only weakly on the Zn/Cu concentration ratio in the solution. The copper content decreases and the sulfur content increases with increasing Zn/Cu. All the elements were found to be distributed almost uniformly. The Cu_xZn_yS thin films have a wide band gap of 3.0-3.6 eV and exhibit p-type conduction and photosensitivity. The ZnO/ Cu_xZn_yS heterojunction cells showed rectification properties. Secondly, Cu_xZn_yS thin films were deposited by PCD. Transmission in the visible region is high, about 70% ~ 80% for an about 0.2 μm-thick film, and the bandgap is 3.6 eV. The p-type conduction was confirmed by the photoelectrochemical (PEC) measurement. Cu_xZn_yS thin films deposited by ECD were annealed in N_2 atmosphere for one hour at 100 ~ 400ºC. The Zn and Cu contents did not vary significantly. However, O and S contents depend on the annealing temperature. The optical transmission increased with increasing annealing temperature.

The DC and two-step pulsed ECD methods were applied for fabricating Cu-Zn-Sn-S-O (CZTSO) thin films. Oxygen content in the film is smaller for the films deposited by pulsed ECD than that deposited by DC ECD, and a slightly Cu-poor and Zn-rich composition ratios were obtained. The bandgap is about 1.5 eV for the films deposited by pulsed ECD. P-type conductivity and photosensitivity of the films were confirmed by the PEC measurement, and the pn heterojunction consisting of CZTSO deposited by pulsed ECD and ZnO showed rectification properties. CZTSO thin films deposited by pulsed ECD were sulfurized at 300ºC.

After the sulfurization, the oxygen amount decreased clearly. However, Cu content was reduced near the surface. Relatively strong XRD peaks of CZTS were observed, and very weak photovoltaic effects were confirmed.

FeS_xO_y thin films were deposited by the ECD method from the deposition solution containing $FeSO_4$ and $Na_2S_2O_3$. The composition is Fe:S:O ≈ 1:1:1, when the $FeSO_4$ concentration is 40 mM, $Na_2S_2O_3$ concentration 100 mM, and the deposition temperature 15 ~ 40ºC. By the PEC measurement, the film was found to be p-type. The band gap was estimated to be about 1.2 eV. A ZnO/ FeS_xO_y heterostructure was fabricated, and clear rectification properties were observed. After annealing at 100 ~ 400ºC in a nitrogen atmosphere for an hour, the Fe content did not vary significantly. However, O and S contents depend on the annealing temperature. The optical transmission and the bandgap increased with increasing annealing temperature. After the 400ºC annealing, the XRD peaks of Fe_3O_4 were observed and the conduction type was changed to n-type.

Cu_xZn_yS is a new wide gap p-type semiconductor and should be applied to ultraviolet and visible LED and photo detectors. Both CZTSO and FeS_xO_y are novel materials for the solar cell absorption layer. Possibility of application of CZTSO films for solar cell was demonstrated, but clear advantage was not found in comparison with CZTS films deposited by others methods. On the other hand, FeS_xO_y film has a great advantage that Fe is much more abundant than Cu, Zn and Sn. Photovoltaic effects of the heterojunction solar cell were not observed. However, the rectification properties confirmed in this work can be regarded as an important achievement, and extensive further research should be done for realization of FeS_xO_y-based solar cells.

5.2. Suggestions for future work

In the present work, Cu_xZn_yS thin films were deposited by ECD. We fixed the sum of the concentrations of $ZnSO_4$ and $CuSO_4$ at 30 mM, and varied the Zn/Cu ratio. All the deposited

films are p-type conduction. The largest Zn/Cu concentration ratio is 40, and the deposited film still showed p-type conduction. We suggest to increase the Zn/Cu concentration ratio further to find at which ratio the Cu_xZn_yS film changes to i- or n-type.

The surface of the Cu_xZn_yS film deposited by ECD is not uniform compared with those deposited by PCD. One possible reason would be that the deposition solutions are not stable: colloidal sulfur precipitates. Therefore, we suggest to decrease $Na_2S_2O_3$ concentration or change pH value to prevent colloidal sulfur formation.

CZTSO thin films were deposited by the two-step pulsed ECD method. After the sulfurization, the oxygen content was decreased, and weak photovoltaic effects were confirmed. However, Zn and Cu elements were redistributed within the film during the sulfurization. We suggest use of other additives to control the oxygen content without sulfurization.

FeS_xO_y thin films were deposited by the ECD method, and for the heterojunction with ZnO, rectification properties and photosensitivity were confirmed, but not photovoltaic effects. The absence of photovoltaic effects will be due to large density of defect states, because the optical transmission is very low. Thus, the origin of the defects needs to be investigated, and the deposition condition needs to be reexamined to reduce the defect concentration.

Journals

1. **Kai Yang**, and Masaya Ichimura:
   "Fabrication of transparent p-type Cu_xZn_yS thin films by the electrochemical deposition method",
   Jpn. J. App. Phys. **50**, (2011), 040202-1~3.

2. **Kai Yang**, Yuki Nakashima, and Masaya Ichimura,
   "Electrochemical Deposition of Cu_xS and Cu_xZn_yS Thin Films with p-Type Conduction and Photosensitivity",
   J. Electrochem. Soc., **159**(3), (2012), H250-H254.

3. **Kai Yang**, and Masaya Ichimura:
   "Fabrication of Cu-Zn-Sn-S-O Thin Films by the Electrochemical Deposition Method and Application to Heterojunction Cells",
   Inter. J. Photoenergy, **2012**, (2012), 154704-1~6.

4. Mandula, **Kai Yang** and Masaya Ichimura:
   "Photochemical deposition of p-type transparent alloy semiconductor Cu_xZn_yS", Semicond. Sci. Technol., **27**, (2012), 125007-1~5.

5. **Yang Kai**, Shoichi Kawai and Masaya Ichimura
   "Electrochemical deposition of Fe-S-O thin films"
   Submitted to Sol. Energy Mater. Sol. Cells

Presentations

1. **Kai Yang**, Masaya Ichimura:
   "Fabrication of Cu-Zn-Sn-S-O thin films by the electrochemical deposition method and application to hetero-junction cells",
   21st International Photovoltaic Science and Engineering Conference (PVSEC-21), Nov.28-Dec.2, 2011, Fukuoka, Japan.

2. **Kai Yang**, Shoichi Kawai, Masaya Ichimura:
   "Electrochemical deposition of Fe-S-O thin films",
   23st International Photovoltaic Science and Engineering Conference (PVSEC-23), Oct.28-Nov.1, 2013, Taipei, Taiwan.

Scholarship:

Oct. 2009 ~ Mar. 2010 Japan Student Services Organization (JASSO)

Apr. 2010 ~ Mar. 2011 Meitetsu International Scholarship Foundation

Apr. 2011 ~ Mar. 2012 Meitetsu International Scholarship Foundation

Apr. 2012 ~ Mar. 2013 Nagaya Institute of Technology I- scholarship

Apr. 2013 ~ Mar. 2014 Rotary Yoneyama Memorial Foundation

Research Grant:

Mar. 2013 The Hori Sciences and Arts Foundation Research Grant

Nov. 2013 The Nitto Foundation Presentation Research Grant

Awards:

Mar. 2013 Aword of vice-president of Nagaya Institute of Technology